

**UNIVERSITY OF OSLO
Department of Geoscience;
Meteorology and
Oceanography Section**

**Evaluation of two
model versions of
the Oslofjord with
different grid
resolutions**

Master thesis in
Geosciences

Peter Isachsen

01. juni 2014



Abstract

We consider results from from a one year simulation in the Oslofjord area, produced by an 800- and 300- meter versions of the ROMS model. The two versions differ only in resolution and grid orientation. Our objective is to evaluate similarities and differences between the two version. To this end we study current patterns, kinetic energy levels and last, but not least, particle trajectories. By doing this we quantify the effect of an increased grid resolution, enabling us to assess what size resolution is required for simulations of the fjord dynamics. We find that a higher skill regarding the representation of bathymetry and coastal geometry in the model grid enables resolution of smaller, stronger and more confined eddies, causing the higher resolution model to be more energetic. Moreover, simulations in areas where the two model grids display diverging coastal geometry and bathymetry produce diverging particle trajectories. In contrast simulations in more open regions where the relative difference in bathymetry is smaller yield more similar trajectories. This conclusion is reached by decomposing the kinetic energy into a mean and eddy part, and inspecting the eddy patterns of the two. We find a correlation between the spatial location of the eddies and the trajectories taken. We conclude, that it is not the effect of resolution itself that is of major importance in the fjord, but rather the implications it brings in the form of enhanced bathymetry and coastal geometry. Some other more obvious findings are that a more natural coastal geometry preclude/permit certain trajectories. Moreover, the inclusion of islands in the model domain obstructs eddy generation, and possibly cause island wakes.

Acknowledgement

First and foremost I wish to thank my supervisor Lars Petter Røed, who have thought me everything I know about numerical ocean modeling.

I would also like to thank Nils Melsom Kristensen (MET) and André Staalstrøm (NIVA), for helping me with problems regarding the more technical aspects of ROMS.

A special regard also goes out to Karina Hjelmervik at HBU, who was very helpful at the early stages in the thesis.

I also like to thank my soon to-be wife Shruti for putting up with me all this time, and for offering moral support in the times i needed it the most.

My appreciation also goes out to all my fellow students, friends and family.

Peter Isachsen
Oslo, June 2014

Contents

| | |
|---|-----------|
| Abstract | i |
| Acknowledgement | iii |
| 1 Introduction | 1 |
| 1.1 The Oslofjord | 2 |
| 2 Theory | 5 |
| 2.1 Terrain following coordinate systems | 5 |
| 2.1.1 The pressure gradient error | 6 |
| 2.2 The First Baroclinic Rossby radius of deformation | 7 |
| 2.3 Energy | 7 |
| 3 Method | 11 |
| 3.1 The model fjord | 11 |
| 3.2 Forcing | 12 |
| 3.2.1 Atmospheric input | 13 |
| 3.2.2 Lateral boundary forcing | 13 |
| 3.2.3 River and tidal input | 13 |
| 4 Model Setup | 15 |
| 4.1 The model grids | 17 |
| 4.2 Locations of special interest | 20 |
| 4.2.1 The Drøbak strait | 20 |
| 4.2.2 Svelvik-Verket | 20 |
| 4.2.3 Hvaler | 21 |
| 4.3 Forcing; some minor differences | 23 |
| 4.4 Verification | 23 |
| 4.4.1 Tides | 28 |
| 5 Results | 29 |
| 5.1 Kinetic energy | 29 |
| 5.2 Results in terms kinetic energy | 30 |
| 5.3 Particle trajectories | 44 |
| 5.4 Results in terms of particle trajectories | 45 |

| | | |
|----------|----------------------------------|-----------|
| 6 | Discussion | 59 |
| 6.1 | Preliminary discussion | 59 |
| 6.2 | Development in energy | 60 |
| 6.2.1 | Spin-up | 60 |
| 6.2.2 | Discussion | 61 |
| 6.3 | Particle trajectories | 62 |
| 7 | Summary and final remarks | 65 |
| A | Appendix I | 68 |
| A.1 | ROMS parameters | 68 |
| A.2 | ROMS module list | 69 |
| B | Appendix II | 71 |
| B.1 | Harmonic analysis | 71 |

List of Figures

| | | |
|-----|---|----|
| 1.1 | An illustration of the Oslofjord resolved in 3 different model grids. The resolution of the grids are (from the left) 4 kilometers, 800 meters and 100 meters. <i>Courtesy of Prof. Karina Hjelmervik, HBU</i> | 3 |
| 1.2 | A map of the Oslofjord. The marked locations will be referred to at later stages in the thesis. <i>Original grid obtained from NIVA.</i> | 4 |
| 2.1 | Figure showing the variations in the first baroclinic Rossby radius of deformation. Figure taken from <i>Chelton et al. (1997)</i> | 8 |
| 3.1 | The area covered by the full NorKyst-800- (right), and the Nonocur bathymetry (left). The coloring is depth depending. | 14 |
| 4.2 | Difference in bathymetry between grids | 15 |
| 4.1 | The bathymetry of the a) 800m, b) 300m and c) 150m reference grid. | 16 |
| 4.3 | Depth values for the different domains along chosen line (b). Fourier transform of the values from the top plot (a). | 19 |
| 4.4 | The two model grids in the area around the Drøbak strait. | 21 |
| 4.5 | The two model grids in the area around Svelvik-Verket. | 22 |
| 4.6 | The two model grids in the area around the Hvaler archipelago. | 22 |
| 4.7 | The yearly mean surface temperature for a) 300m version, b) 800m version and c) Nonocur. Covering the simulation period 31.Okt 2010 - 30.Sept 2011. | 24 |
| 4.8 | As Figure 4.7, but displaying the mean surface salinity. | 25 |
| 4.9 | As Figure 4.7, but displaying the mean surface current. | 26 |
| 5.1 | The location of the 6 different scenarios in which Lagrangian drifters are released, in addition to the placement of 4 chosen locations where we will take a closer look at the kinetic energy levels later on. | 31 |

| | | |
|------|--|----|
| 5.2 | Panel a) shows the averaged TKE for both model versions as a function of time. Panel b) shows the amount of water contained in the simulations. helping us interpret the results for the volume averaged kinetic energy. Day 1 corresponds 31.okt.2010. We have used a 21 day average to calculate the values resulting in the missing values for the 10 first and last entries. Panel c) gives a more detailed view on the early development in the KE in the versions, giving insight into the length of the spin-up period. This plot is based on unaveraged model results with a 5 minute spacing, and hence also include tidal effects. | 32 |
| 5.3 | As Figure 5.2, but showing the eddy kinetic energy (a) and mean kinetic energy (b) | 33 |
| 5.4 | Yearly averaged TKE as defined in (2.7) and (2.10) for a) 300m- and b) 800m versions. Areas not common for both grids are removed to ease the comparison. . | 35 |
| 5.5 | As Figure 5.4, but showing the EKE as defined in (2.9). | 36 |
| 5.6 | As Figure 5.4, but showing the MKE as defined in (2.8). | 37 |
| 5.7 | 5 day mean (Day 135-140 in simulation) averaged EKE as defined in (2.8) for a) 300m- and b) 800m versions. Areas not common for both grids are removed to ease the comparison. | 38 |
| 5.8 | Surface kinetic energies for location 1 as a function of time for the whole simulation. Day 1 corresponds to 31.okt.2010. We have used a 21 day average to calculate the values, resulting in the missing values for the 10 first and last entries. The plot also includes the atmospheric wind speeds at the same position to check for possible correlations. The plots is showing the following: a) TKE, b) MKE and c) EKE. | 40 |
| 5.9 | Surface kinetic energies for location 2 as a function of time for the whole simulation. Day 1 corresponds to 31.okt.2010. We have used a 21 day average to calculate the values, resulting in the missing values for the 10 first and last entries. The plot also includes the atmospheric wind speeds at the same position to check for possible correlations. The plots is showing the following: a) TKE, b) MKE and c) EKE. | 41 |
| 5.10 | Surface kinetic energies for location 3 as a function of time for the whole simulation. Day 1 corresponds to 31.okt.2010. We have used a 21 day average to calculate the values, resulting in the missing values for the 10 first and last entries. The plot also includes the atmospheric wind speeds at the same position to check for possible correlations. The plots is showing the following: a) TKE, b) MKE and c) EKE. | 42 |
| 5.11 | Surface kinetic energies for location 4 as a function of time for the whole simulation. Day 1 corresponds to 31.okt.2010. We have used a 21 day average to calculate the values, resulting in the missing values for the 10 first and last entries. The plot also includes the atmospheric wind speeds at the same position to check for possible correlations. The plots is showing the following: a) TKE, b) MKE and c) EKE. | 43 |

| | | |
|------|--|----|
| 5.12 | Lagrangian drifters trajectories for scenario 1 during the 2nd run for a.) 300m- and b.) 800m version. Each line represent the trajectory of a single Lagrangian drifter, and their color coding changes with respect to the number of days spent by the drifter in the domain relative to the release-time. | 47 |
| 5.13 | Lagrangian drifters trajectories for scenario 1 during the 3rd run for a.) 300m- and b.) 800m version. Each line represent the trajectory of a single Lagrangian drifter, and their color coding changes with respect to the number of days spent by the drifter in the domain relative to the release-time. | 48 |
| 5.14 | Lagrangian drifters trajectories for scenario 2 during the 1st run for a.) 300m- and b.) 800m version. Each line represent the trajectory of a single Lagrangian drifter, and their color coding changes with respect to the number of days spent by the drifter in the domain relative to the release-time. | 50 |
| 5.15 | Lagrangian drifters trajectories for scenario 2 during the 3rd run for a.) 300m- and b.) 800m version. Each line represent the trajectory of a single Lagrangian drifter, and their color coding changes with respect to the number of days spent by the drifter in the domain relative to the release-time. | 51 |
| 5.16 | Lagrangian drifters trajectories for scenario 3 during the 1st run for a.) 300m- and b.) 800m version. Each line represent the trajectory of a single Lagrangian drifter, and their color coding changes with respect to the number of days spent by the drifter in the domain relative to the release-time. | 52 |
| 5.17 | Lagrangian drifters trajectories for scenario 3 during the 3rd run for a.) 300m- and b.) 800m version. Each line represent the trajectory of a single Lagrangian drifter, and their color coding changes with respect to the number of days spent by the drifter in the domain relative to the release-time. | 53 |
| 5.18 | Lagrangian drifters trajectories for scenario 4 during the 2nd run for a.) 300m- and b.) 800m version. Each line represent the trajectory of a single Lagrangian drifter, and their color coding changes with respect to the number of days spent by the drifter in the domain relative to the release-time. | 55 |
| 5.19 | Lagrangian drifters trajectories for scenario 5 during the 1st run for a.) 300m- and b.) 800m version. Each line represent the trajectory of a single Lagrangian drifter, and their color coding changes with respect to the number of days spent by the drifter in the domain relative to the release-time. | 56 |
| 5.20 | Lagrangian drifters trajectories for scenario 6 during the 3rd run for a.) 300m- and b.) 800m version. Each line represent the trajectory of a single Lagrangian drifter, and their color coding changes with respect to the number of days spent by the drifter in the domain relative to the release-time. | 57 |
| B.1 | Harmonic analysis at Viker for the 300 meter setup during the time span covering run 1 (11.Feb - 11.Mar 2011). Plot a) shows the sea elevation, and plot b) shows the size of the different tidal constituents. | 72 |
| B.2 | Harmonic analysis at Viker for the 800 meter setup during the time span covering run 1 (11.Feb - 11.Mar 2011). Plot a) shows the sea elevation, and plot b) shows the size of the different tidal constituents. | 73 |

| | | |
|-----|---|----|
| B.3 | Harmonic analysis at Viker for the 800 meter setup during the time span covering run 3 (11.Aug - 9.Sept 2011). Plot a) shows the sea elevation, and plot b) shows the size of the different tidal constituents. | 74 |
| B.4 | Harmonic analysis at Viker for the 800 meter setup during the time span covering run 3 (11.Aug - 9.Sept 2011). Plot a) shows the sea elevation, and plot b) shows the size of the different tidal constituents. | 75 |
| B.5 | The sea level pressure at Viker during all 3 runs. | 76 |

List of Tables

| | | |
|-----|---|----|
| 4.1 | Overview of the r -value for the different grids. | 18 |
| 4.2 | The Table yielding information on the wavelength in the model grids. The factor $2\Delta s$ is the smallest wavelength resolvable in the model grids; $10\Delta s$ is the recommended value to ensure clear signals; Fourier the lower limit wavelength resolved in the transformation 4.3. | 18 |
| 5.1 | Overview of the time span covered by the different runs | 45 |
| A.1 | ROMS spesific parameters. | 68 |

Chapter 1

Introduction

The Norwegian Meteorological Institute (MET) publishes ocean forecast on a daily basis, providing invaluable information to people all over Norway. This is done via the use of numerical ocean weather prediction (NOWP) models running on supercomputers, solving the governing equations of the ocean using numerical methods. Using standard finite difference approximation (FDA), methods as such the accuracy is determined by the finite length or increment of the spatial grid and time step used, most often referred to as the model's grid resolution. Here we investigate the effect of increasing the grid resolution when simulating particle motion inside the Oslofjord.

Until 2011 the operational ocean model at MET employed a computational grid with a horizontal resolution of 4 kilometers. An ocean model with this resolution is able to capture large scale patterns, but much of the ocean weather occurs on much smaller scales than this. This is particularly true in the Oslofjord. The foremost discrepancy between the ocean and the atmosphere is the difference in the range of scales. In the atmosphere you have pressure systems on the scale of 500km with a lifetime of days. While the typical scale of such features in the ocean would be 10km with a lifetime, possibly approaching months. This is caused by the big difference in the inertial Rossby radius of deformation, particular in sub-polar and higher regions. Because of this a global mesoscale daily ocean forecast model is still not within the realms of possibility, due to limitations in computer capability. As a result, nesting techniques are used in which values from coarser grid ocean models are employed as boundary forcing, enabling high resolution simulations locally. Here we compare two models. One of them is a local area cut out of the NorKyst-800 modeling domain.

The NorKyst-800 modeling system was introduced by MET in 2011. NorKyst-800 is a national ocean weather forecasting system, with a spatial resolution of 800 meters, based on ROMS (Regional Ocean Modeling System). The system provides daily forecasts viewable at the web-page www.yr.no.

From Vilhelm Bjerknes famous article published in 1904 (*Bjerknes, 1904*), we know that the quality of a weather forecast is linked up to two key components. Those are the skill of the model in emulating nature, and the quality of the initial conditions given into the model to start with. By increasing the grid resolution of a ocean model, we enable a more exact representation of

sometimes complex bathymetry and the irregular coastline, hopefully increasing the model skill. This is costly from a computational point of view, hence an ocean-modeler only uses the grid resolution necessary to properly simulate the features he/she wants to examine.

In addition to delivering the daily ocean weather MET is also responsible for emergency tasks, and has to produce forecast in short notice in the event of extraordinary circumstances, like search and rescue after people adrift at sea or oil spills. Access to a well-functioning modeling system under such circumstances, might save lives and/or decrease the damage done to nature. The Oslofjord has been the victim of 2 major oil spills within the recent years, the “Full City” (Jul 2009) and “Godafoss” (Feb 2011) incidents. The availability of a local high resolution model for the area could have made the job containing the spills easier.

This study focuses on comparing the results from two ocean models. The mentioned local version of NorKyst-800, and a second 300 meter version, also based on ROMS. These two versions differ only in resolution and model grids orientation. Our main objective is to consider how differences in grid resolution expresses itself in terms of;

- current patterns.
- development in kinetic energy.
- trajectories of particles (e.g. oil)

By doing this we will try to quantify the effect of resolution, and the effects that follow with it, enabling us to assess what size resolution is required for simulations of the fjord.

Figure 1.1 illustrates the achieved effect increasing the grid resolution provide. The figure shows the representation of the Oslofjord by three separate model grids. The grid to the left has a spatial resolution of 4 kilometers, the middle 800 meters and the right 100 meters. For coastal area forecasts the representation of the coastline plays a huge role, and looking at Figure 1.1 it would be naive to think that these three grids would yield the same results for the region, in particular regarding particle trajectories.

1.1 The Oslofjord

The Oslofjord is approximately 100 kilometers long, stretching from the city of Oslo down to the Færder lighthouse (Fig. 1.2). It offers a complex bathymetry, including a deep channel running from the regions just north of Horten southwards towards Skagerrak. This is the deepest feature in the fjord, with a depth ranging between 200-450 meters. The fjord has small tidal variations, and hence major forcings are the atmosphere, rivers, and the lateral boundary conditions. The weather is found to be a decisive factor in deciding the behavior of the ocean in the region. The natural narrowing at Drøbak splits the fjord into two main parts, known as the inner- and outer fjord.

The area around the Oslofjord is the densest populated region in Norway, and the biggest portion dwells in the regions surrounding the inner parts in the fjord. The fjord also holds several big

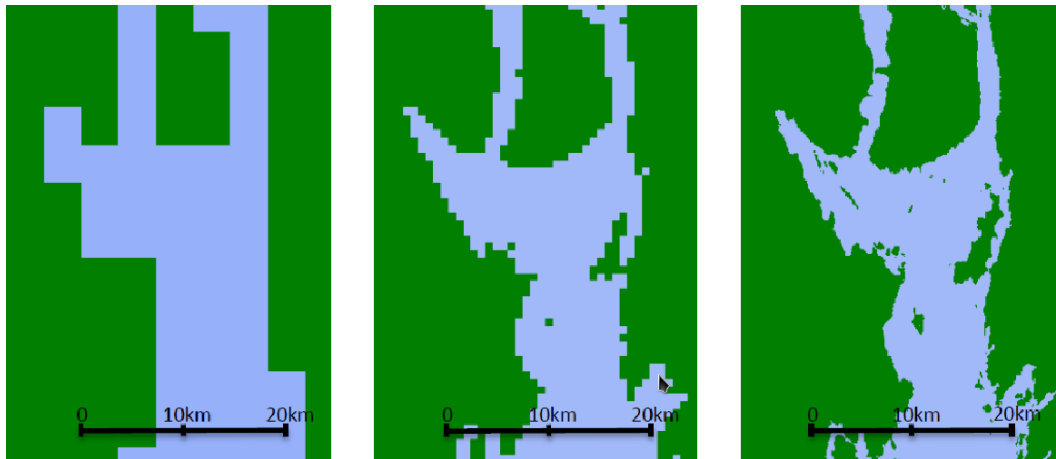


Figure 1.1: An illustration of the Oslofjord resolved in 3 different model grids. The resolution of the grids are (from the left) 4 kilometers, 800 meters and 100 meters.

Courtesy of Prof. Karina Hjelmervik, HBU

harbors, and as a result has the highest commercial traffic in the country. In addition, an increasing amount of leisure boats is leading to an even bigger strain on the recreational areas in and around the fjord.

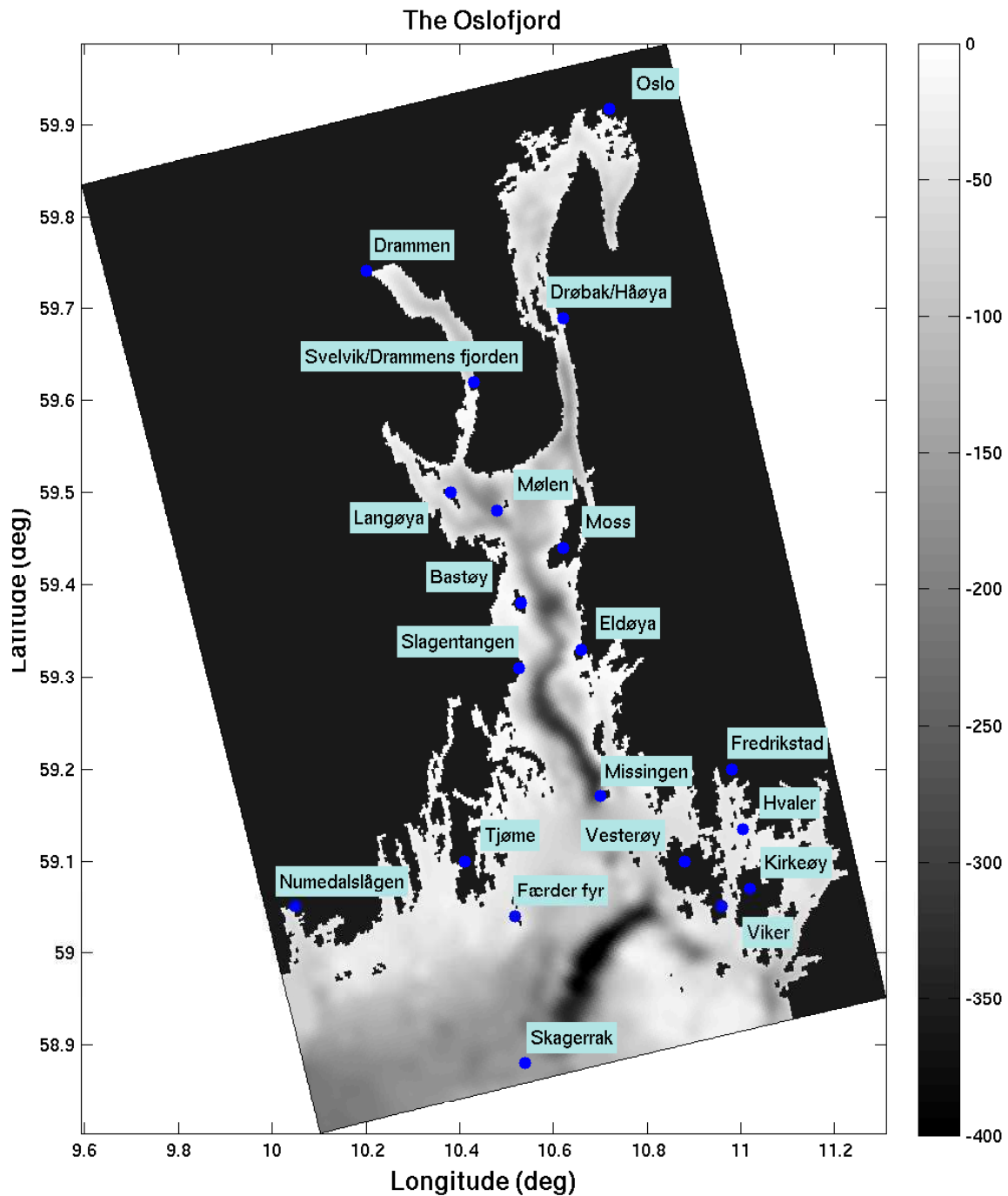


Figure 1.2: A map of the Oslofjord. The marked locations will be referred to at later stages in the thesis.

Original grid obtained from NIVA.

Chapter 2

Theory

We consider the performances of two fjord models, and hence much of the following theory is on this subject.

2.1 Terrain following coordinate systems

We start by quoting *Griffies (2004), page 121*. “The choice of vertical coordinate is the most important aspect of an ocean model’s design. This choice strongly prejudices the model’s representation of various resolved dynamical processes and determines the details of how to parameterize unresolved processes”. We will now look into just why this is the case, building much of our discussion on (*Griffies, 2004*).

The vast majority of ocean models uses either terrain-following (σ)-, pressure- or ordinary z -coordinates to describe the vertical position. Our fjord model belongs to the class of terrain following coordinate models, and hence we focus on this clan of models.

The σ -coordinate system was first presented by *Phillips (1957)*. It was designed for meteorological purposes, with an emphasis on the Planetary boundary layer. It involves a coordinate transformation $(x, y, z, t) \rightarrow (x', y', \sigma, t')$ where $x' = x, y' = y, t' = t$, meaning that it is only the vertical z -coordinate that changes during the transformation. The coordinate transformation for z look as the following:

$$\sigma = \frac{z + \eta}{H + \eta} \quad (2.1)$$

Here $\eta(x, y, t)$ is the displacement of the ocean surface with respect to $z = 0$, and $H(x, y)$ is the ocean depth. At $z = 0$ equation (2.1) yields $\sigma = 0$, and for $z = -H$ we get $\sigma = -1$. Using the depth values of the different z -levels, the coordinate transformation, depending on the total ocean depth and surface displacement, creates an monotonic mapping between the $\sigma(x, y, t)$ and z values. However, in some special cases we might end up with σ -values lacking this monotonicity. This happens in regions where the ocean surface displays overhangs (i.e lapping backwards extending over the lower ocean floor). When this is the case the monotonicity is broken, and hence there is no unique relationship between the two coordinates anymore. This implies that

certain σ values could be referring to multiple positions in space at the same time, rendering the ocean model unable to utilize it for calculations. Note that this problem is more theoretical, as the smoothing procedure performed on model grids prior to simulations will remove such features.

The transformations ensures a free surface. For ocean models based on an ordinary z -coordinate system, the elevations of the ocean surface is limited to the height of the topmost grid cell. This is not the case for σ -coordinates, as the elevation in this case is “spread” between all the different σ -layers.

The transformation ensures that the line $\sigma = -1$ always equals to the position of the ocean floor, a trait other coordinate systems like z or ρ do not display. The much smoother representation of the Ocean boundary layer (OBL) in a σ -coordinate system, makes it the ideal choice for investigating near bottom dynamics.

However, looking at the oceanic boundary layer (OBL), standard σ -coordinate models are presented with a problem. When moving away from the coast towards the more central region of the basin, the vertical distance between the σ layers will typically increase, leading to a possibly faulty representation of the OBL in σ -coordinate models. In *Haidvogel and Beckmann (1999)* the authors present a solution to this problem, introducing a more complex version of (2.1). This equation makes use of two additional user predefined factors which renders the modeler able to increase resolution in certain regions (i.e Ocean boundary layer), making the problem a non-issue

2.1.1 The pressure gradient error

Gravity is defined as a vertical force, exerting a drag towards Earth’s center. In an ordinary z -coordinate system the vertical direction is aligned with the gravity, resulting in a pure horizontal pressure gradient. This is not generally the case for a σ -coordinate system. The σ -lines are created from the ocean depth and surface elevations, changing with both time and space, hence the horizontal pressure gradient term in a σ -coordinate model is made up from two separate terms

$$\nabla_z p = \nabla_\sigma p + \rho g \nabla_\sigma z \quad (2.2)$$

Where p is the pressure, g the gravitational acceleration and ρ the density.

The term $\nabla_\sigma p$ is the pressure gradient along the σ surfaces, while $\rho g \nabla_\sigma z$, also called the “sigma correction term”, stems from the relative difference between the z - and σ -surfaces. The term is typically small, but when approaching steep bathymetry (i.e. large relative difference between the z - and σ -surfaces), it can be on the same order as pressure gradient term. This means that a σ -coordinate model, to ensure credible solutions, has to be able to represent both these terms in a sufficient manner.

In regions with large bathymetry gradients and strong stratification (i.e high Burger number), the representation of the latter term has proven to be a problem. Much research has been put into the subject, and in the article *Beckmann and Haidvogel (1993)* the authors presented a solution partially vindicating some of the problems. This article presented the r -value (also known as the Beckman and Haidvogel number); defined as

$$r = \frac{|h - h^*|}{h + h^*} \quad (2.3)$$

Where h and h^* is the depth of two neighboring wet[†] grid cells, and $0 \leq r < 1$ is a dimensionless number. The r -value yields information on the bathymetry gradient between the two grid cells, and to high values would indicate that a smoothing procedure of the grid is required prior to simulation. There is a lack of consensus regarding how high the r -value of a model grid can be. *Beckmann and Haidvogel* (1993) operated with a r -value of 0.21, and found that this greatly reduced the error related to the pressure gradient.

There is also another problem associated with the pressure gradient when using σ -coordinates, and that is cancellation. We mentioned that $\rho g \nabla_{\sigma} z$ could be on the same size as $\nabla_{\sigma} p$ in the vicinity of steep topography, but what we did not mention is that the terms has opposite signs. The subtraction of two large nearly equal numbers is a known problem in numerics, as it is associated with loss of accuracy and hence errors.

2.2 The First Baroclinic Rossby radius of deformation

The first baroclinic Rossby radius of deformation is an essential parameter in numerical ocean modeling. The radius gives is a measure on the distance a current can travel before affected by the Coriolis force. The value has a inverse dependence in the Coriolis force, causing it to rapidly decrease towards higher latitudes. Figure 2.1 gives an illustration of this. Note the values for regions around the Oslofjord is less than 10 kilometers. In terms of mathematics the first Rossby radius of deformation can be written as,

$$L_{R,1} = \frac{c_1}{f} \quad (2.4)$$

where c_1 is the phase speed of the 1st mode gravity wave and f is the Coriolis parameter. The phase speed is dependent on the stratification and the ocean depth, explaining the smaller variances in figure 2.1. The phase speed is a product of the Brunt-Väisälä frequency and the scale height $c = NH$, showing the dependence on stratification. The theory is based around the stratification to be constant in time, also causing $L_{R,1}$ to time independent.

2.3 Energy

To evaluate the two model versions we investigate the kinetic energy (KE). Specifically we split the KE into its mean and eddy part. We consider the development of the system, that is:

$$KE = \frac{1}{2} \rho_0 \mathbf{u}^2 \quad (2.5)$$

where ρ_0 is a reference density and \mathbf{u} is the horizontal current components. Note that we neglect the vertical velocity component since this is much smaller than the horizontal velocities. \mathbf{u} is in this case a daily mean, since we want to filter out the tidal variations from the currents.

[†]Wet grid cells are all cells within the model domain, subtracted the ones laying on land or placed at the boundary. The values obtained in these cells are all calculated form the model itself.

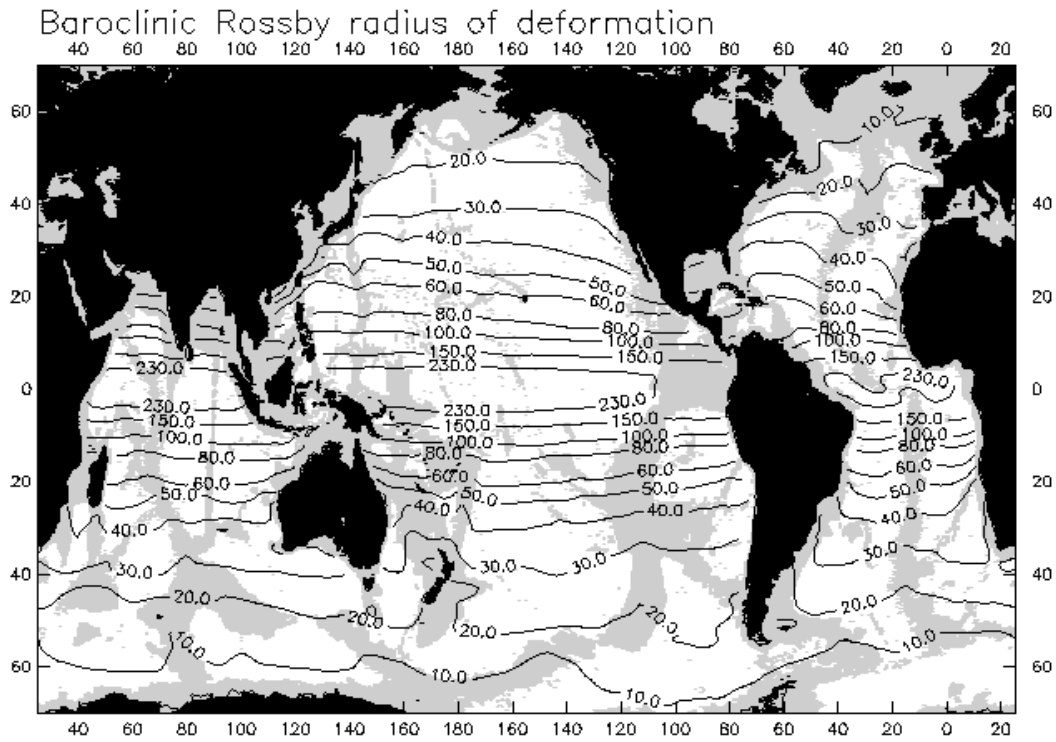


Figure 2.1: Figure showing the variations in the first baroclinic Rossby radius of deformation. Figure taken from *Chelton et al. (1997)*.

Let $\mathbf{u} = \bar{\mathbf{u}} + \mathbf{u}'$ where $\bar{\mathbf{u}}$ is the average current defined as a temporal average, and \mathbf{u}' is the deviation from the mean velocity. Then

$$KE = \frac{1}{2}\rho_0(\bar{\mathbf{u}}^2 + 2\bar{\mathbf{u}}\mathbf{u}' + \mathbf{u}'^2) \quad (2.6)$$

If we average (2.6), knowing that $\bar{\bar{\mathbf{u}}} = \bar{\mathbf{u}}$ and assuming $\bar{\mathbf{u}'} = 0$ we get with:

$$\overline{KE} = \underbrace{\frac{1}{2}\rho_0\bar{\mathbf{u}}^2}_{\text{mean kinetic energy}} + \underbrace{\frac{1}{2}\rho_0\overline{\mathbf{u}'^2}}_{\text{eddy kinetic energy}} \quad (2.7)$$

$$MKE = \frac{1}{2}\rho_0\bar{\mathbf{u}}^2 \quad (2.8)$$

$$EKE = \frac{1}{2}\rho_0\overline{\mathbf{u}'^2} \quad (2.9)$$

$$TKE = \overline{KE} = MKE + EKE \quad (2.10)$$

Note that MKE is the KE associated with the mean motion, while EKE is a measure of the variance in the currents. The definition of eddy and mean in the case is somewhat loose, as this is decided by the time span the last averaging is taken over.

Chapter 3

Method

3.1 The model fjord

Both versions of the Oslofjord model used here are based on the Region Ocean Modeling System (e.g., *Shchepetkin and McWilliams (2005); Haidvogel et al. (2008)*) or ROMS for short. ROMS, is a state of the art ocean modeling system that solves the Reynolds-averaged Navier-Stokes equations. The model is hydrostatic and has a free surface. It employs a combination of an Arakawa C-grid (*Arakawa, 1966; Arakawa and Lamb, 1977*) in the horizontal and a σ -coordinate (Chap.2.1) in the vertical. Note that the model offers more advanced versions of the σ coordinate transformation, in line with the one mentioned at the end of Chapter 2.1. These more complex transformations make it possible for the user to increase the vertical resolution in certain parts of the water column. This will cause the model to make due with fewer vertical layers, and thus reducing the cost of computation. The system itself is available for public use, and thus used by many oceanographic communities. The system is implemented with a C-preprocessor, which enables the user to easily tailor his/her model setup for its intended use, before compiling the system. The possible choices include among other things various turbulence closure- and boundary layers schemes, in addition to both a sea ice- and ecosystem module. For optimal computer efficiency, the computational kernel separates the barotropic and the baroclinic terms in the governing equations, for so to advance them with different size time steps. This is possible because the stability constraint on the barotropic mode, is notably higher than the one for the baroclinic (Chap.2.2). This separation saves the model for a lot of computations, as we do not need to calculate the baroclinic parts with the same frequency as the barotropic.

The end result is a very flexible and robust system that can be tweaked to fit multiple purposes, and thus widely used.

For more extensive documentation on ROMS, the reader is referred to the community homepage (<http://www.myroms.org>).

Prior to the introduction of the NorKyst-800 system (*Albretsen et al., 2011*) MET used a 4 km ocean model version of ROMS to obtain daily forecasts in the Norwegian waters. An increasing demand for higher accuracy and a more streamlined modeling system, birthed the NorKyst-800.

The modeling system is a joint venture between MET, Institute of Marine Research (IMR), and the Norwegian Institute for Water Research (NIVA). It is based on the ROMS model, and model especially for the Norwegian coastal waters. The systems has a grid resolution of 800x800 meters, and its full bathymetry can be seen in Figure 3.1.

The modeling suite also provides full river and tidal forcing for the same area, in addition to several choices for atmospheric forcing. The system is fitted with a user-friendly interface, which makes the creation of the forcing files and running simulations a trivial task. The NorKyst-800 system is as of this date (21.May 2014), the basis for multiple ocean forecasts, including those used at MET's own <http://www.yr.no>.

The newer release of the NorKyst-800 suite (v2) also includes a modeling suite called Norfjords. Norfjords is a tool designed for modeling smaller areas with high resolution, making it ideal for near-coast simulations. To run the application the user has to obtain a high resolution grid, and give in the location of the grid via latitude and longitude coordinates to Norfjords. The application will then interpolate user specified forcing (atmospheric, tides, etc), created via the NorKyst-800 main application down to this new grid. This procedure was also followed in the creation of the majority of the forcing files for one of our Oslofjord versions. Norfjords offers a relative fast and easy way for creating local high resolution model versions, more or less ready for simulation out-of-the-box. The use of Norfjords requires some technical insight into the ROMS modeling system, and knowledge in the manipulation of NetCDF files, but can be a very powerful tool if mastered.

3.2 Forcing

ROMS is a regional ocean model (ROM), and as most ocean models, it lacks routines for calculating dynamics not involving the sea. In a real case these external factors would affect the behavior of the ocean, and thus need to be included if one wants to perform realistic simulations. One good example would be wind blowing over the ocean surface. We all know that this will exert a drag on the upper ocean layer, producing a change in velocity.

Since ROMS is regional, it employs a lateral boundary at the edge of the domain where the simulations are performed. At these boundaries the model itself cannot calculate the development of the different scalar fields, as it lacks input from the surrounding areas. We still need values in these cells to be able to conduct our simulations, and we solve this by giving these to ROMS as external forcing files.

ROMS can be told to run without factors like atmosphere, rivers and tides, but will always need a set of initial- and boundary conditions. All forcing files are typically on the netCDF (Network Common Data Form) format, a format widely used in both meteorology and oceanography. NetCDF is compact, simplifies exchange of model results by supporting multiple platforms, and still enables the user to keep track of the content in an easy way.

3.2.1 Atmospheric input

The unified model (*Cullen and Davies* (1991)) or UM for short, is a numerical weather prediction (NWP) system developed by the United Kingdom Met office in the early 90's. In the following years many of the other national weather-forecasting agencies adapted and refined the model for their own use, among those the Norwegian Met office. The system has its forte in being very robust (i.e. usable over a wide scale of ranges), making it a widely used, and also earning the model its name. The UM4km is a 4x4km model version based on the UM model suite run by MET, providing atmospheric model results for the area inside and in close vicinity to Norway. NorKyst (Chap.3.1) offers model results from UM4km as a possible choice for the atmospheric input in a ocean model, and this is what we chose to employ in our own model version.

3.2.2 Lateral boundary forcing

The Nonocur project (*Røed and Kristensen* (2012)) was carried out by the Norwegian Meteorological Institute (MET) in collaboration with the Institute of Marine Research (IMR). They were commissioned by Norwegian oil company Statoil to provide high resolution ocean variables for the North-Sea region for the year 2011 (fig.3.1), probably in connection with development of oil-infrastructure in the region. The ocean model utilized for this task was MET's own modified version of ROMS, NorKyst-800. For initial and boundary conditions the team used results from a cruder configuration called SVIM. The system was set to run for the period between 2.Okt 2010 - 1.Jan 2012, where the 3 months prior to 2011 were used to spin up the model. When performing a cold start (i.e. when the initial conditions used in the model do not strain from the model itself), one might experience strong gradients in the model fields. The strength of these gradients are depending of the differences between the initial conditions and models own equilibrium (they are probably not equal..). To counteract biases created by this, it is standard procedure to run a model for some time prior to simulations, making sure that the model has "settled", and thus produce the best possible results for the wanted period.

Although originally meant to investigate the North-Sea, the Nonocur model domain also covers the Oslofjord (Fig.3.1), and thus the model results are used as both initial- and lateral boundary conditions in our two model version.

3.2.3 River and tidal input

The river forcing in NorKyst (Chap.3.1) is based on the river discharge model created by (*Beldring et al.*, 2003). The model calculates the flux associated with a river with respect to its catchments and climatic input, making the fluxes exhibit seasonal variations. The full forcing set contains river fluxes from a total of 249 rivers where 247 are Norwegian and 2 are Swedish. The flux is modeled as a point-source placed at the land-sea interface in the model grid.

Our Oslofjord domain contains a total of 15 rivers. The most notable is Glomma, which has its estuary in Hvaler at city of Fredrikstad. Other important contributors are also Drammenselva and Numedalslågen (Fig.1.2).

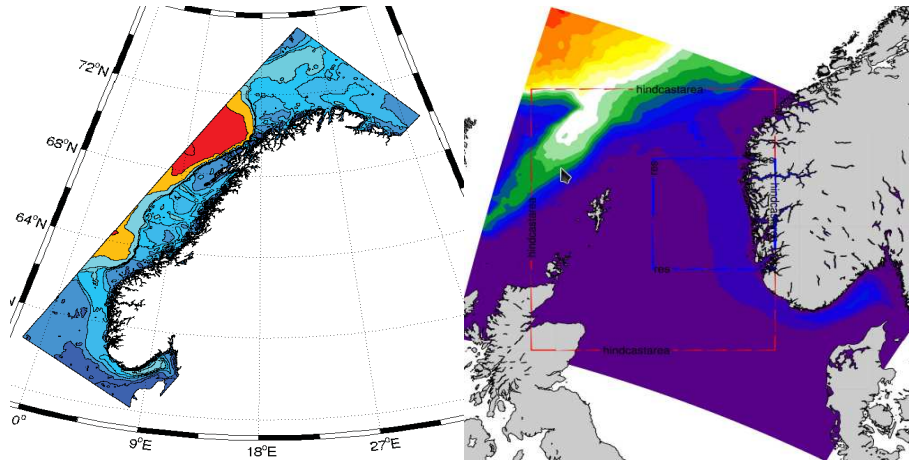


Figure 3.1: The area covered by the full NorKyst-800- (right), and the Nonocur bathymetry (left). The coloring is depth depending.

The tidal forcing in NorKyst is based on TPXO7.26 (Egbert *et al.*, 1994; Egbert and Erofeeva, 2002), a global inverse barotropic tidal model that covers the 8 largest tidal constituent (M_2 , S_2 , N_2 , K_1 , K_2 , O_1 , P_1 , Q_1). The original forcing file in NorKyst has values for the amplitude and phase for these constituent covering the entire original NorKyst domain. Depending on region and time, the tides will often constitute a large portion of the total dynamics in an ocean model. Thus, it is good practice to verify that an ocean model is able to simulate the tides in a reasonable way. This can be done via a harmonic analysis. Through this procedure one calculates the amplitude and phase angle of the different tidal constituents using the model results, and validate these against more credible data. The analysis is grounded in the assumption that total tide can then be expressed as the sum of a finite set of sinusoids at given frequencies, that is,

$$h_{tide} = a_m \sin(\omega_m t - \phi_m) \quad (3.1)$$

where h_{tide} is total tidal elevation, $a_m t$ the amplitude, and ϕ_m the phase angle of the tidal component m . At last, we quickly mention the matlab tool T_tide (Pawlowicz *et al.* (2002)). This is a user-friendly and powerful tool, especially made for investigating the tides in an ocean model. The system takes in a time series of ocean height values at a fixed point, and from this calculates the amplitude and phase angle of the most important tidal constituents. This can be used to verify/validate the model and/or to quantify the amount of energy in the model connected to the tides in a fast and easy way.

Chapter 4

Model Setup

We make use of two separate model versions, both based on ROMS (Chap.3.1). One has a spatial grid resolution of 800 meters, and the other 300 meters. Both model versions employ the same modules, and have the same forcing except for some minor differences explained in this chapter. The initial and boundary conditions values are taken from the Nonocur (Chap.3.2) simulation, and for the atmospheric forcing model results from the UM4KM (Chap.3.2) NWP model was used. The versions differ in choice of time step, as the higher resolution in the 300 meter version requires a shorter temporal increment to remain stable. Thus the time step for the 300m version was set to 20 seconds, while the time step in the 800m version is 40 seconds.

ROMS requires a set of parameters to be predefined prior to the simulations. These were set so they would match the Nonocur model run for both versions. The parameters decide the spatial distribution of the vertical σ -layers (Chap.2.1), and for optimal performance they should match the values on the boundaries. Both versions utilize a third order upstream scheme for horizontal-, and a fourth order centered in time and space scheme for the vertical advection of momentum and tracers. For the turbulence closure the Generic Length Scale (GLS) mixing parameterization was chosen (Warner *et al.*, 2005). On the lateral boundaries ROMS operates with a set of boundary conditions for the different scalar fields. The most important possibly being the radiation condition (Orlanski, 1976), which is used in tandem with a nudging

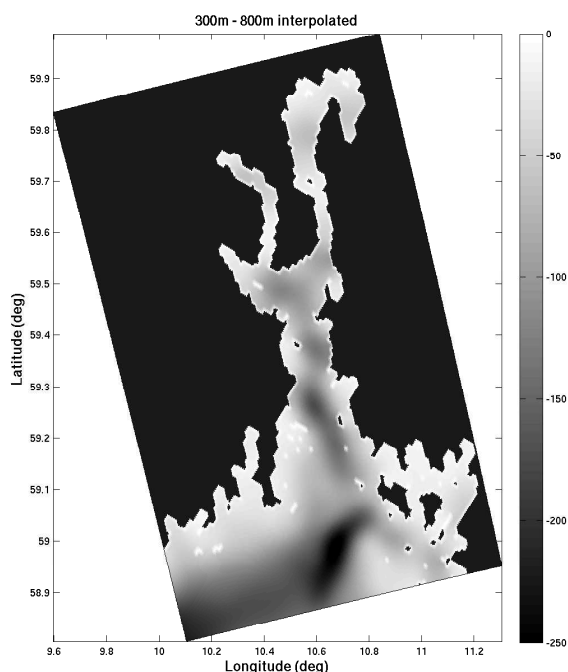


Figure 4.2: The difference between the 800- and 300 meter grids. Here the bathymetry from the 800 meter grid have been interpolated over to the mesh of the 300 meter grid and then subtracted.

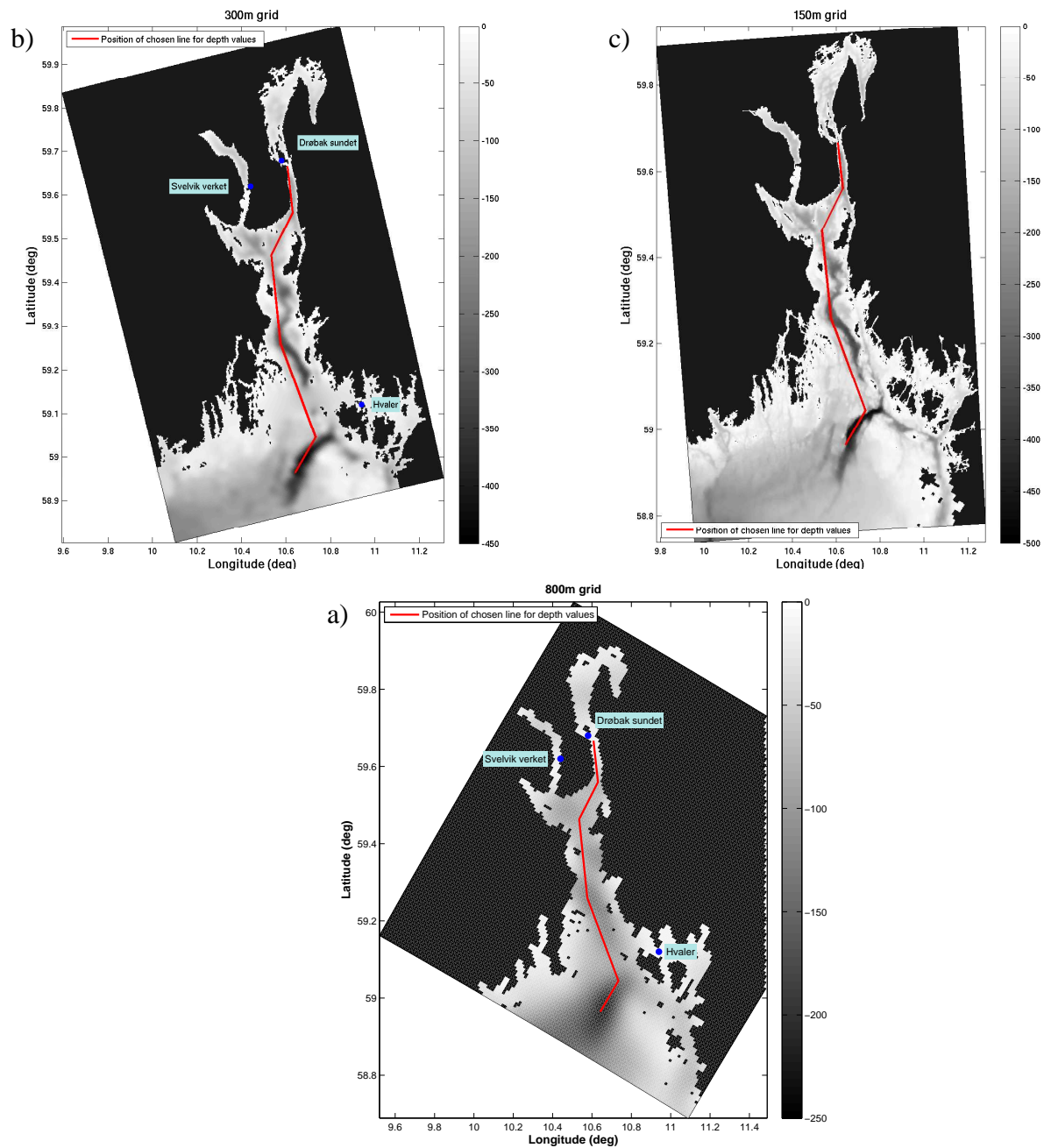


Figure 4.1: The bathymetry of the a) 800m, b) 300m and c) 150m reference grid. The red line marks the location of depth values used in the Fourier analysis. The three names are locations of special interest, where the two model grids deviates greatly in form of bathymetry and coastal geometry.

zone for all the three dimensional scalar fields. For more specific details on the parameters and modules used, the reader is referred to the Appendix (Appendix A).

4.1 The model grids

Our two model versions, naturally also employ two different grids. The grid used in the 800m version was made directly with the NorKyst-800 application (Chap.3.1), as a cut-out of the original grid, while the refined 300m grid was obtained from NIVA. The difference between the two are profound, in terms of bathymetry and coastal geometry. Hence, a closer examination is required before starting the actual experiment. In the comparison we have also included a 150 meter grid (also obtained from NIVA), as a reference.

Figure 4.1 gives an overview of the bathymetry resolved in the different model grids. First of all we note the large differences in depth (most notably the maximum depth), between the coarse 800m- and the other two grids. The is most pronounced regions are the deep channel following the middle of the fjord, and the sill located southwest of Hvaler approaching the southern boundary of our domain. Steep gradients may place unwanted constraints on the time step and in worst case cause the model solution to blow up. Because of this it is standard procedure to smooth out the bathymetry in a model grid prior to simulation, which will cause differences between the real bathymetry and the final grid bathymetry. Higher resolution grids are able to keep a larger portion of the original details, as an increased number of grid cells allows for sharper gradients. This means that the grid resolution is a key factor for simulations in “rugged“ regions (i.e. coastal areas), as well as capturing the key features of the local terrain is prerequisite for producing credible results. Small islands and tiny river- and fjord outlets are simply smoothed out of the 800m grid, a difference that probably will yield local differences between the simulations. In addition to the mentioned smoothing, our grids have also been trough a procedure where all horizontal gaps (fjords etc.) have been made at least two ρ -points wide, as ROMS has problems handling one-point bays. This opens for the possibility of having motion in both directions at the same height level, while also enabling the use of a larger time step, as the increase in volume will weaken the gradients.

Figure 4.2 shows the difference in bathymetry between the grids used in the two different versions. Here a simple interpolation has taken place to move the 800m bathymetry over on the 300m mesh, and then these values are subtracted from each other. We see quite big disparities all over the domain, with the a maximum of around 200 meters located in the southern part of the basin.

Looking at the r -value (Chap.2.1) for our grids, it is actually the 800m grid that has the higher numbers (tab. 4.1), despite the extensive smoothing applied to this grid. We see that mean r -values for all the grids are within acceptable ranges, but the tables displays a clear trend. A higher resolution grid allow for a smaller r -value, and hence a more accurate simulation. We mentioned in our theory section (chap. 2.1) how σ -coordinate models have a built in bias in areas of high r -values, meaning that the two coarser grids, particularly the 800m, may be prone for biases. In regions with a r -value of 0.85, the mentioned effect of cancellation (Chap.2.1) would be highly relevant, resulting in a loss off accuracy, and local biases in the model scalar fields. There is no

| Grid | 150 meter | 300 meter | 800 meter |
|--------------------|-----------|-----------|-----------|
| Wet grid-cells | 168786 | 38485 | 4473 |
| Average r -value | 0.056 | 0.083 | 0.18 |
| Maximum r -value | 0.2 | 0.43 | 0.85 |

Table 4.1: Overview of the r -value for the different grids.

| Grid | $2\Delta_s$ | $10\Delta_s$ | Fourier |
|------|-------------|--------------|---------|
| 150m | 300m | 1.5km | 3km |
| 300m | 600m | 3km | 6km |
| 800m | 1.6km | 8km | 20km |

Table 4.2: The Table yielding information on the wavelength in the model grids. The factor $2\Delta_s$ is the smallest wavelength resolvable in the model grids; $10\Delta_s$ is the recommended value to ensure clear signals; Fourier the lower limit wavelength resolved in the transformation 4.3.

real consensus on the maximum r -value a grid can display, but values of 0.85, and even 0.43, would by most oceanographers be deemed as high.

The red line in Figure 4.1 is plotted from a set of chosen latitude and longitude coordinates (the same set for each grid), that were picked so that the line would coincide with the deeper part of the basin in all of the grids. The depth values were taken out along the line and plotted in the upper part of Figure 4.3. Here the effects of the smoothing can be seen clearly, examining the two extremes of the plot. The smooth curve from the 800m grid, and the more rugged curve spawned from the 150m grid. The mentioned difference in maximum depth is also shown well here. Turning our attention to the bottom part of Figure 4.3, which contains a Fourier transformation of the values from the top panel. The depth the line representing the 300m grid seems to coincide well with the 150m grid, thus one can believe that they both contain approximately the same amount of the longer wavelengths. Inspecting the bottom plot we see that this is clearly is not the case. Already at approximately $\lambda \sim 15000\text{m}$ the 300m- has fallen way off the 150m-transformation. The 800m grid seems to have an even harder time, resolving waves only smaller than $\lambda \sim 20000\text{m}$. Table 4.1 shows an interesting observation. When examining current events (i.e. eddies, jets, meanders) it is recommended to at least employ a grid resolution 10 times larger than the object in question, to ensure a clear signal. From Table 4.1 we see that the Fourier transformation, only yield clear signals when approaching the 20Δ limit. This is worth noting, as it implies that the ordinary 10Δ recommendation is insufficient in the Oslofjord area.

Here we also note that the factor $2\Delta_s$, also known as the Nyquist frequency (*Shannon, 1949*) places an upward constraint on the wave numbers included. This is of course also the case for our other grids, but this was cropped to increase view-ability. Our model versions cannot resolve wavelength smaller than the Nyquist frequency, so when the waves reaches these scales, they need to be handled by other means (i.e. diffusion).

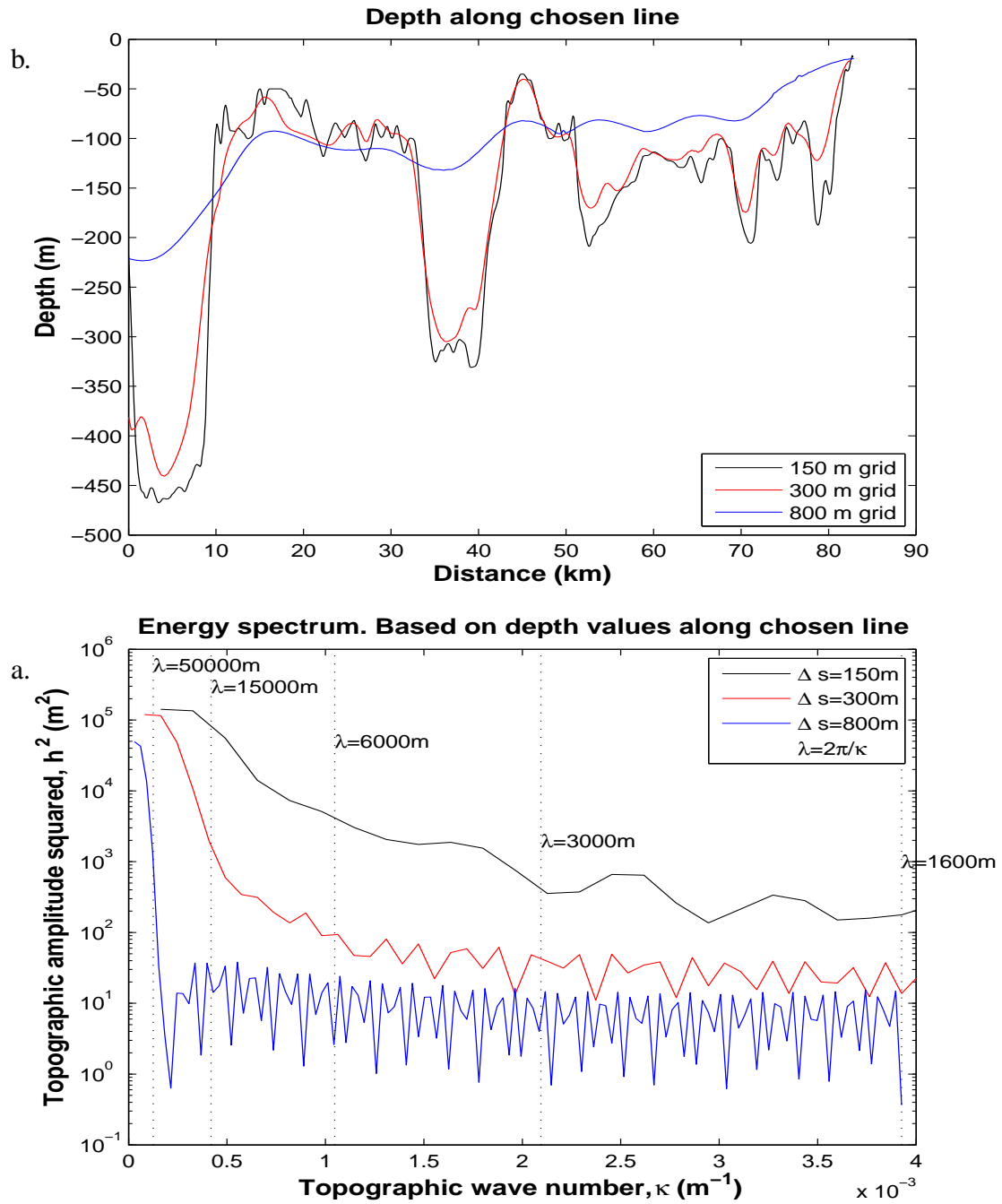


Figure 4.3: Depth values for the different domains along chosen line (b). Fourier transform of the values from the top plot (a).

4.2 Locations of special interest

Until now we have looked at the broader picture of the bathymetry in our two model grids. Closer investigation also reveals large local differences in coastal geometry at certain locations. This may affect the model dynamics substantially, and more comprehensive examination of the grids might help us explain model results later on. It also provides an good illustrations of the effects an increase in grid resolution might prove to have.

4.2.1 The Drøbak strait

The Drøbak strait is centrally placed a bit north of the center in both of our grids. All objects need to pass trough here to reach the city of Oslo and the surrounding areas, making it a key location. Looking at Figure 4.4 we see that only one big island (Håøya) is resolved by the 800 meter grid, while the 300 grid in addition to this also contain 3 smaller islands and several promontories. It is likely that the small cluster of islands seen in the 300m grid could work as a natural barrier, affecting both fluxes and particle trajectories. Taking all this into account it would be naive to exclude the possibility for substantial differences between the two model versions here. The difference in width could cause difference in current speeds in the region, in addition to creating a diverging potential for having particles passing to the strait.

The islands removed from the 800m grid are in them themselves big enough to be resolved, but their placements near the coast combined with the two ρ -point spacing requirement originating from ROMS, results in them being removed. We briefly mentioned this requirement in Section 4.1. There we based our arguments for performing this procedure on an increase in stability and allowing for a longer time step. In addition, to the possibility of having fluxes in both directions, at the same σ -level and time frame. But what do we lose? Our goal is to mimic the real physical processes in an area, and hence this kind of trade-off is common dilemma for modelers. We want our models to simulate nature in a realistic manner, and hence wish for the bathymetry and coastal geometry to be as near true values as possible. At the same time we have to consider the limitations presented by computer power, and based on this choose our resolution, both spatial and temporal. The differences between our two model grids illuminates this trade-off in a good way. With respect to computation time, an arbitrary model employing the 800m grid would be distinctly faster than one based on the 300m grid, but the latter would both have a higher potential for producing credible values and capturing small scales dynamics. Ocean models are tools, and a skilled oceanographer must know what tool to choose for the task at hand.

4.2.2 Svelvik-Verket

Investigating the waters in and around the Drammensfjord (Fig. 4.5), reveals differences between the two model grids. The natural breakwater in the middle of the Drammensfjord where the small town of Verket is situated, is completely removed from the 800m grid. In the 300m grid this feature is present, and this discrepancy might prove to yield big differences in the dynamics in the area. The narrowing created by the breakwater is in reality just over 200 meters wide,

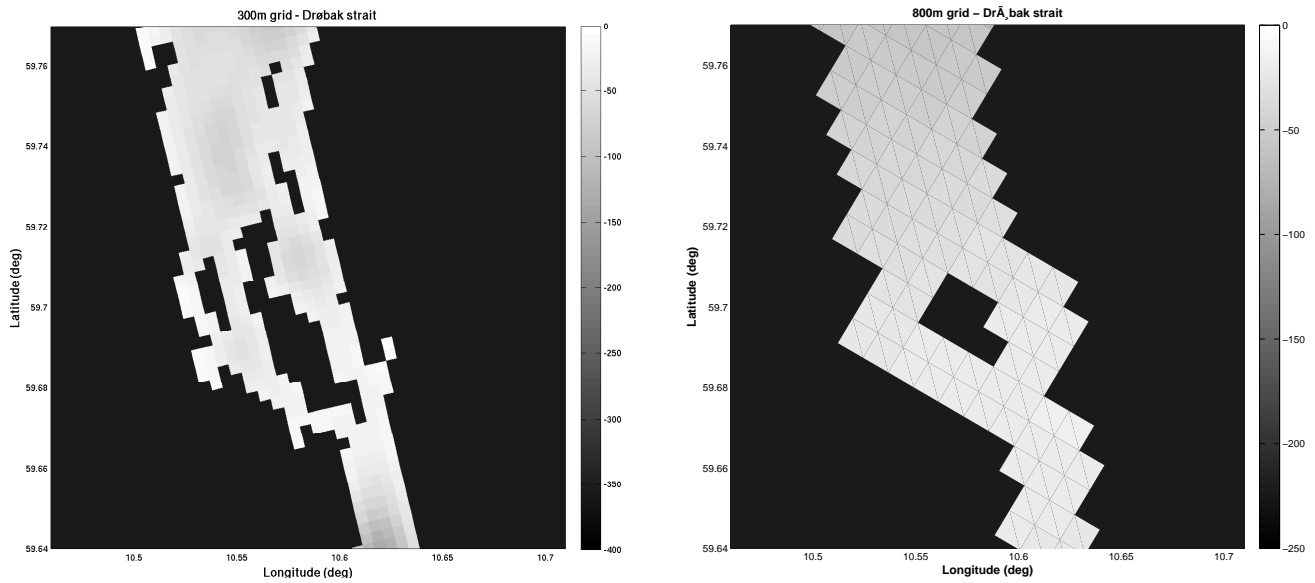


Figure 4.4: The two model grids in the area around the Drøbak strait.

again meaning one would need a 100m grid to properly resolve it, and at the same time fulfill the two ρ -point spacing requirement. The local current in the area, known as the Svelvik current, is the strongest currents in the Oslofjord. The combination of strong currents and discrepancies between the model grids makes this a location of special interest, and hence should be followed closely. The Svelvik current is heavily based upon tides, hence the model versions skill in this department is crucial to be able to reproduce this feature in a proper way.

4.2.3 Hvaler

Finally we take a closer look at the Hvaler archipelago (Fig.4.6), an area that consist of several (hundreds) of islands in all shapes and sizes. This area offers by far the most complex coastal geometry in the Oslofjord. As revealed by Figure 4.6 the archipelago is reduced down to a total of 7 islands (2 big and 5 small), in the 800m grid. The 300m grid is naturally more realistic, but even this does not capture the full extent of the complex coastal geometry in this region. Looking at Figure 4.6, focusing on the area around the leftmost island (Vesterøy Fig. 1.2), the reader should take a special note of the western passage on the north side of this island. In the 800m grid this has been "opened" up via the two ρ -point spacing requirement, creating a new easy-to-access waterway out of the region. Combining this with the notable ocean currents induced by the outflow of the river Glomma in the Fredrikstad region, one could expect pronounced differences in the area, an assumption substantiated by the sheer amount of islands and possible waterways in the region. For the 300m grid the two passages to the south seem like the most natural way for the vast bulk of water to exit the archipelago, while we in case of the 800m grid might expect a more dominate westward flux.

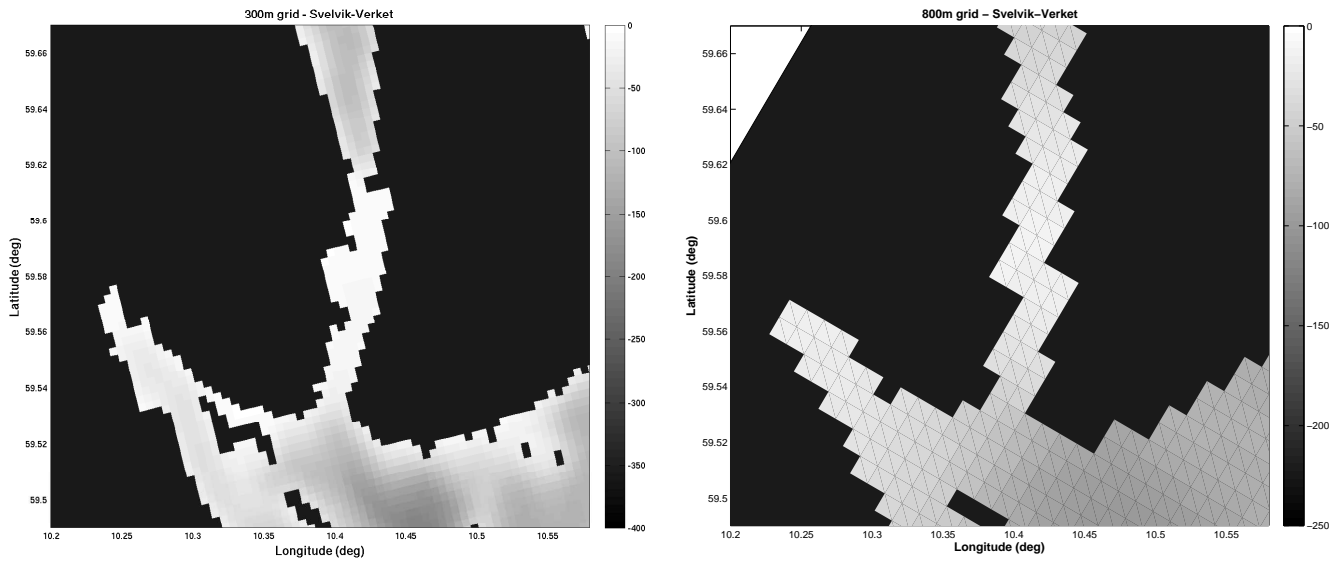


Figure 4.5: The two model grids in the area around Svelvik-Verket.

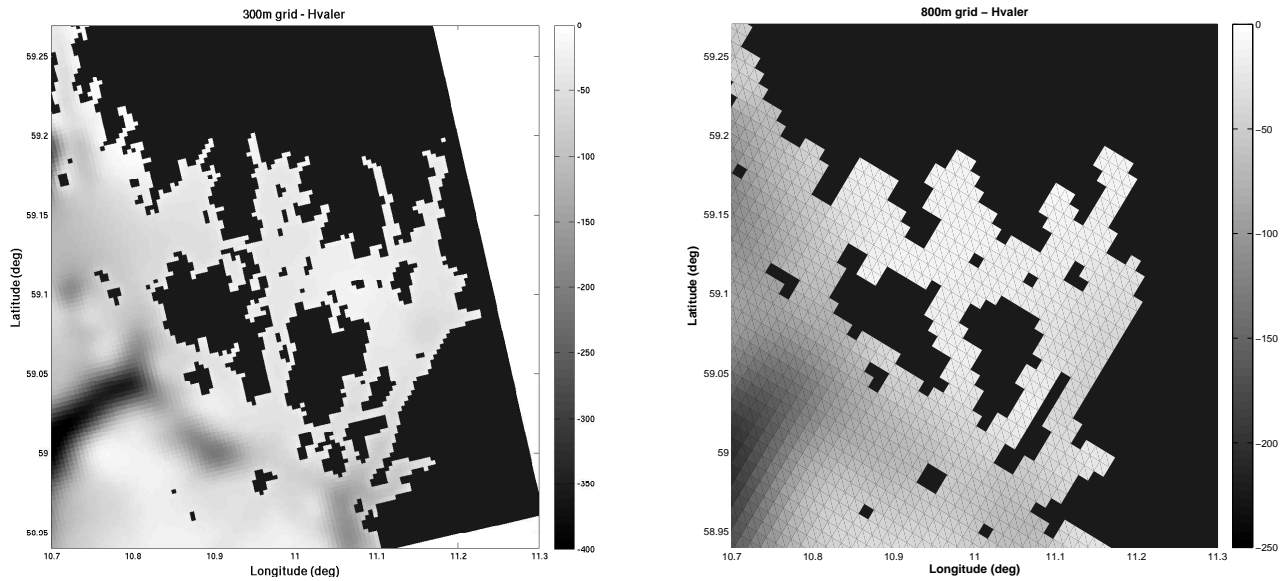


Figure 4.6: The two model grids in the area around the Hvaler archipelago.

4.3 Forcing; some minor differences

We mentioned in the start of this chapter that there are some small differences between the forcing used in our two model versions, and before looking at the results from the control run, we would like to elaborate some more on these.

- The model versions use the same atmospheric forcing, UM4km (Chap.3.2), but in the case of the 300m version the wind-vectors (u and v) had to be rotated. This was required since the grid used by the 300m version differs in its definition of the lateral directions, both with respect to UM4km and the grid used by NorKyst-800 (chap. 3.1). We also encountered problems with ROMS grabbing atmospheric values from the wrong positions in case of the 300m version, a problem probably connected with the difference in grid resolution between our two versions. This was solved via a direct interpolation of the atmospheric forcing over to the 300m mesh. These procedures could cause some differences between the versions, but they are presumed to be small.
- The creation of the river forcing file is closely linked with the model grid contained in the NorKyst-800 application. However, the 300m version is based on an entirely different grid, making the automated procedure in NorKyst-800 a non-viable option. We therefore had to create the river forcing via partly self-made code, which could cause the effects of rivers to vary between the versions.
The total volume fluxes of water released are the same in both of the versions, but the exact location of the river outlets will vary some since the outlet has to be specified in a single u or v grid-point (depending if the outlet has a north/south or east/west direction). Since the point source consists of a single grid cell, the currents associated with river fluxes will have a higher maximum value and be more confined in the 300m version.
- The position of Mosseelva differ between the grids. This is clearly depicted in Figure 4.7 showing the surface salinity for the different versions. In the 800m version the estuary is south of the city Moss, while it is situated to the north of the city, inside the bay called Mossesundet, in the 300m version. The latter placement is the correct one, but one could argue for the former as Moss is separated into two parts by a canal. This canal is only 30 meters wide, and thus too narrow to be resolved in any of our versions. The easy solution is to split the river flux associated with Mosseelva into two separate parts, but as this problem was noticed at a late stage in the study it was left unchanged.

4.4 Verification

To evaluate the performance of the two model versions, a control run was first performed. A one year test run spanning between 31.Okt 2010 - 30.Okt 2011 were carried out, and the results were then compared to the values from the Nonocur (Chap.3.2) simulation for the same time period. We see from Figures 4.7-4.9 that the two model versions do a reasonable job for the

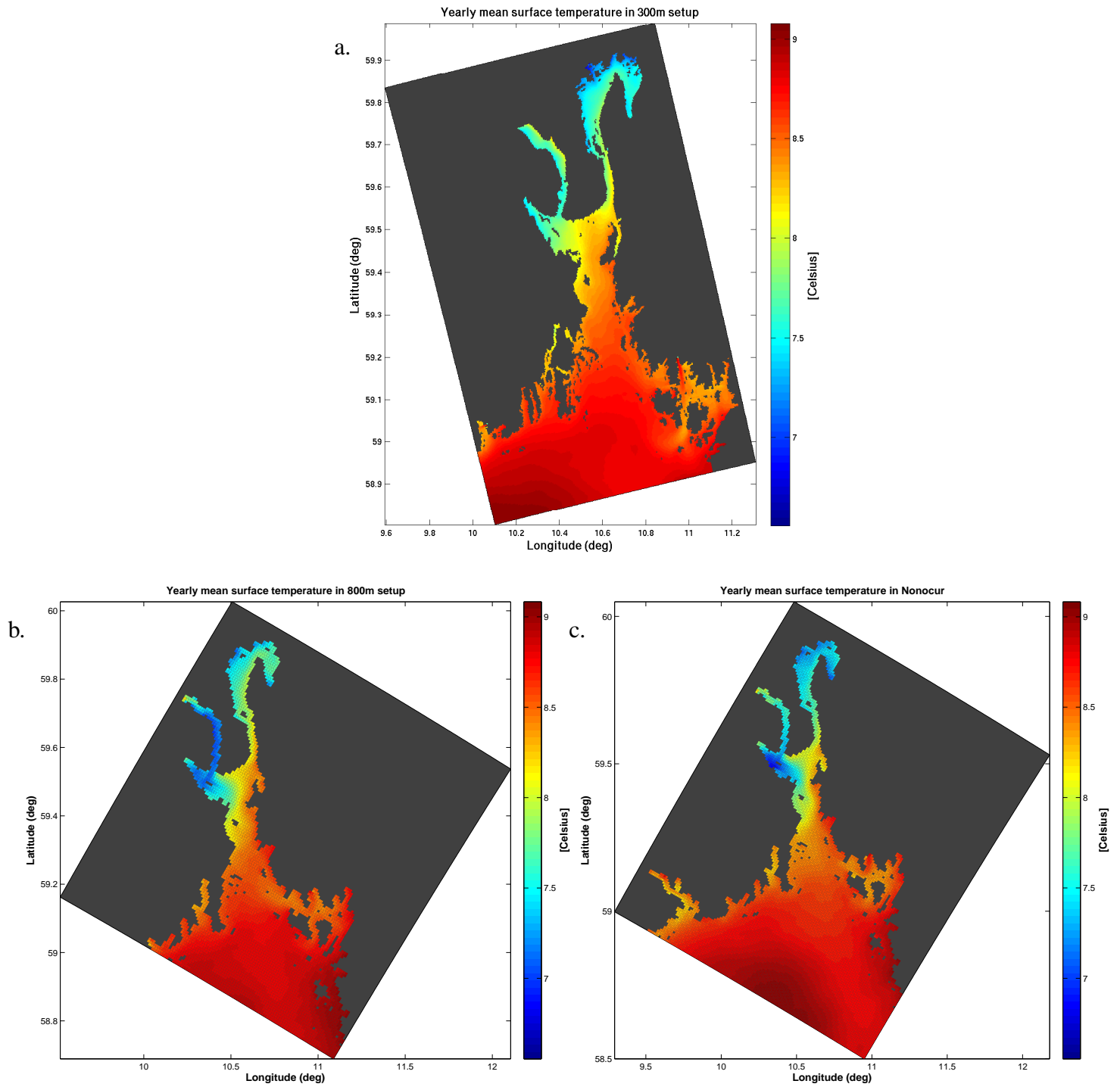


Figure 4.7: The yearly mean surface temperature for a) 300m version, b) 800m version and c) Nonocur. Covering the simulation period 31.Okt 2010 - 30.Sept 2011.

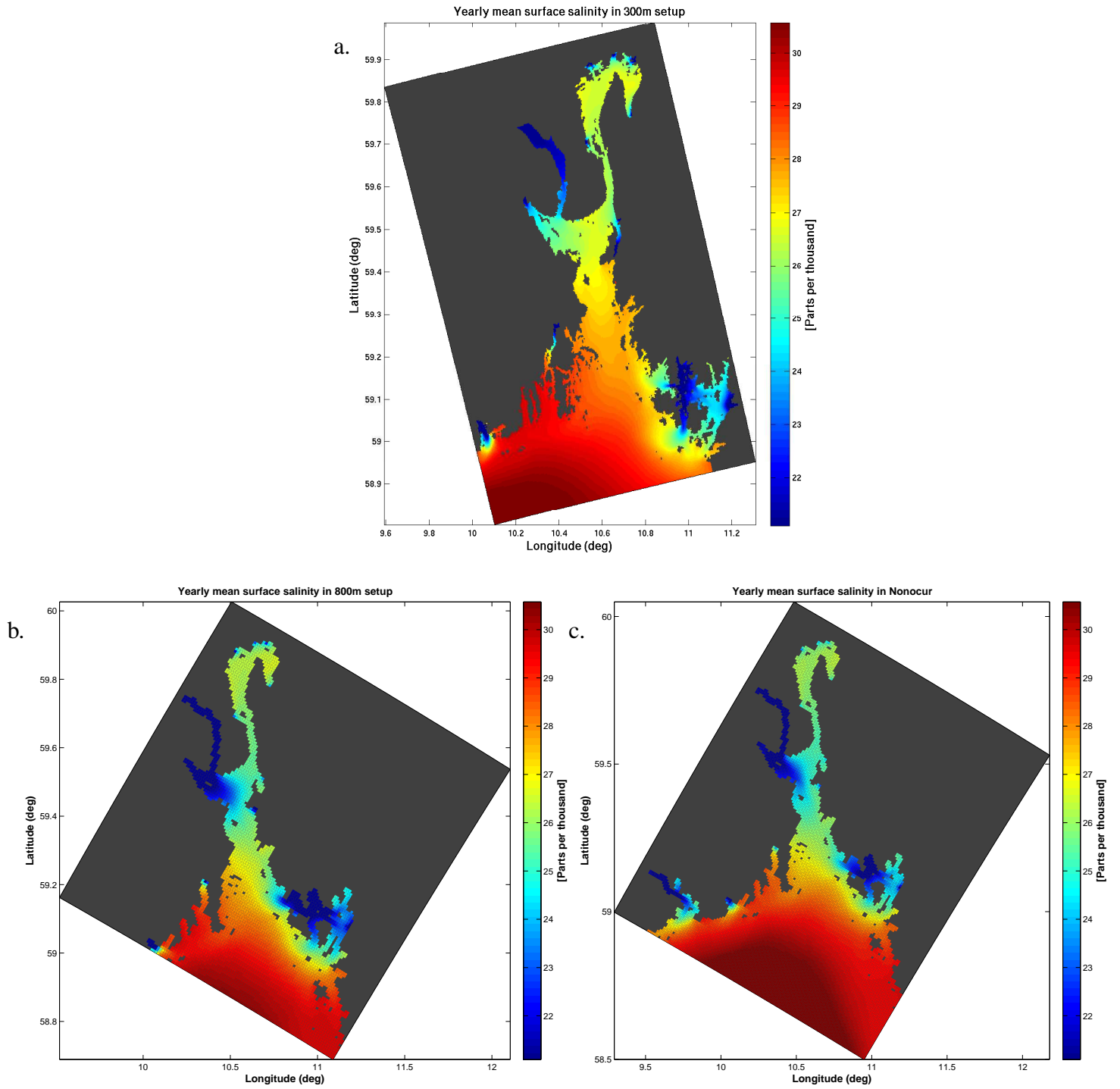


Figure 4.8: As Figure 4.7, but displaying the mean surface salinity.

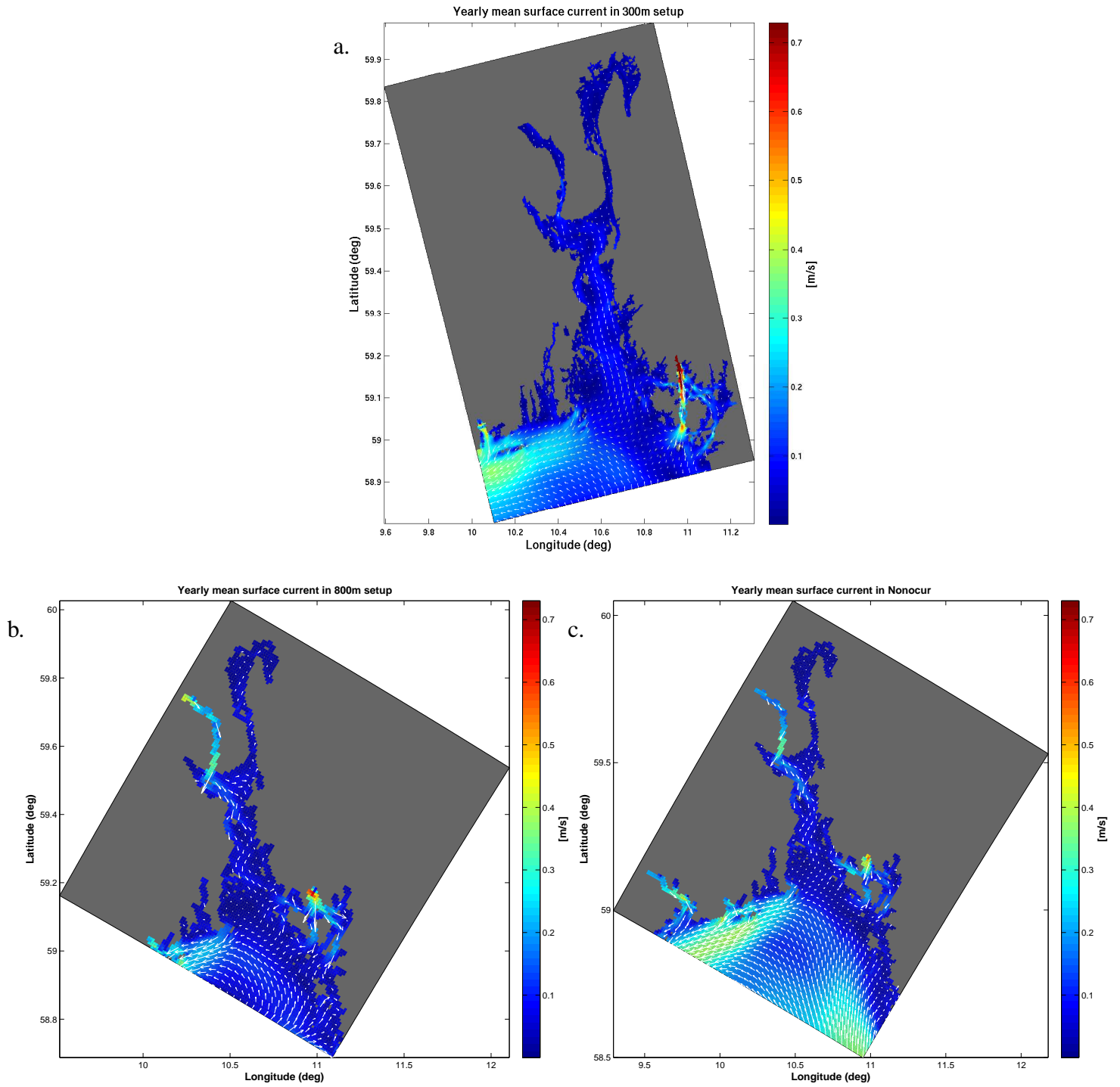


Figure 4.9: As Figure 4.7, but displaying the mean surface current.

large scale patterns in the domain, but there are some differences between our two versions and the Nonocur results. The 800m version does the best job emulating Nonocur, but as both these origin from the same grid this is no surprise. Both models separate slightly from the Nonocur results in the area approaching the southern boundary, an observation that can be explained via the nudging/nesting zone, which ROMS utilizes. The zone consists of the 15 grid-points near the boundary in question, and here the different scalars get “pushed” towards the values received via the lateral boundary condition, to avoid steep gradients. The boundary in Nonocur is placed way out in the Norwegian sea, and thus it is natural to experience some deviations between our model versions and Nonocur near the boundary.

Looking at the areas inside both the Drammensfjord and Drøbak, we have big disparities between the versions. That our 800m version also deviates from Nonocur to such extents is probably due to differences in the tidal forcing in the version. The interchange of the water in these inner parts are heavily tidal dependent, and as our two model versions use another tidal forcing file than Nonocur, this could cause some of the differences.

We note that the majority of the unsimilarities between Nonocur and our 300m version are found in the three locations of special interest, an observation that substantiate many of the assumptions made earlier. With enhanced resolution comes a more natural coastal geometry and bathymetry, which according to the figures, do affect the model dynamics. We should keep this in mind when embarking on the particle trajectories, as the difference in dynamics also should lead to differences in the trajectories.

Investigating the Hvaler archipelago we see that the assumptions from the previous section seems correct. The 300m version has dominating southern current, as this is the most accessible waterway out of the region. In 800m version the current has more of an even split, as the current induced by Glomma is weaker, and all three pathways out of the region is evenly accessible. In addition we also have some deviations between Nonocur and the 800m version in this area. It looks like the outflow from the river Glomma is modified, which in turn results in sending a larger portion of the river flux into the inner parts of the region. Modifications to the river module may have been done, providing us with this difference. The river Glomma is the longest river in Norway, and the water-flux associated with it is by far the largest in our river forcing data-set, hence even small changes involving this river could lead to differences locally.

For the area in and around Svelvik we see differences in in the salinity at the estuary of the fjord. This is probably due to the less saline water originating from rivers inside the Drammensfjord, being advected more effectively in the case of Nonocur and the 800m version (see Fig.4.9 and 4.8). The 800m grid used in these does not include the breakwater at Verket, which apparently allows for higher current velocities out of the fjord. Both the 800m version and Nonocur exhibit a strong surface current (larger than 0.2m/s), a property the 300m version is unable to provide. The lack of this dynamic in the 300m version points towards a slower interchange of water, and hence goes a long way in explaining the higher salinity concentration in the estuary of the fjord. For the waters around the Drøbak strait we actually see good resemblance in all 3 models. The somewhat higher saline concentration in the inner part of the fjord for the 300m version, might also here indicate a more effective interchange in Nonocur and the 800m version. A feasible assumption, since the grids allow for easier access to the inner parts of the fjord.

4.4.1 Tides

One of the biggest uncertainties for both model versions were connected to the tides and the versions ability to properly simulate these. The tidal forcing files created by NorKyst (Chap.3.1) utilized in early test runs, resulted in recorded tides way over measured levels. This was not caused by the quality of the input data, but the interpolation procedure used in the creation of the files. The NorKyst-800 modeling suite is intended for simulations of large domains, and these typically have their physical boundary placed far out in the open sea. By placing the boundaries to close to shore the interpolation procedure grabbed onto onshore values, resulting in a performance-wise poor end result. Harmonic analysis of early simulations done via `t_tide` application (Chap.3.2), showed a doubling of the tidal variations (primarily the M_2 constituent) at the measured station of Viker. To resolve this problem the two original forcing files were replaced with new files acquired from NIVA, in which a more suitable interpolation technique had been used. With this new forcing the tidal components reached more natural values, as both models went from grossly overestimating the tides, to place them-self in the vicinity of measured values. Looking at M_2 constituent for the station at Viker the 800m version has values around 3 cm under the measured levels, while the 300m version overestimate by roughly the same value. Taken into account all the different tidal constituents the 300m version yields the better results of the two, and both versions shows an increase in the prediction skill as the simulations moves forward in time. A more in-depth discussion of the tides in our model versions and results from harmonic tidal analysis, is found in Appendix B.

The purpose with this verification was to check that our model versions were able to produce credible results, and the fact that there were some differences between Nonocur and results obtained should not be to discouraging. The results obtained from both versions are all well within the realm of possibility, and the differences between the versions and Nonocur all fended for in a sufficient manner. This means that analyzing the output from the model versions is a task worth doing, and thus we move on and start our trajectory experiments.

Chapter 5

Results

5.1 Kinetic energy

A direct comparison of the kinetic energy (KE) in our two model version could be highly deceiving, as the model grids do not cover the same areas. To enable such a comparison we decided to overlook contributions in energy from areas not shared by the grids, and as a result the regions south of Hvaler and Vestfold are removed before calculations presented in the upcoming figures. The removal of the region south of Vestfold has an enjoyable side effect. This location mark the start of the Norwegian Coastal Current (NCC), a feature clearly seen in figure 4.9. With this big mesoscale feature removed, the remaining eddies inside the fjord will now contain a larger portion of the total energy. This will again result in a stronger signal, easing our job investigating these features.

Still, the difference in bathymetry and coastal geometry will cause the versions to differ in terms of volume (about 17%), in favor of the 300m version. The additional volume in the 300m grid consists mainly as a mix of deep ocean, smaller fjords and other rugged coastal features. These are regions typically associated with a small KE, and hence it seemed most fair to present the energy budgets for the whole domain (Fig.5.2-5.3) showing the total energy, and not energy per cubic meter.

The KE is calculated from daily u and v estimates, following the calculations presented in Chapter 2.3. The signal from the tides would pollute the calculated values. We mentioned the difference in tidal variations between the grids in Chapter 4.4, meaning that using unaveraged values also would skew the energy budgets in the 300m versions favor, as this overestimates the tides most. To perform the energy calculations with “detided*” values is therefore preferable, and the measure of doing a daily mean will filter out the majority of the tidal variation.

To quantify the model results we decompose the energy into a mean (MKE) and eddy (EKE) part, with values averaged over 21 days as outlined in Chapter 2.3. The act of choosing the actual time-span to average over is an art in itself, and there were some trial and error involved before ending up with the 21 day value. One could argue for a somewhat shorter averaging period, trying to maximize the differences between our two model versions. The 300m version

is believed to sustain more short lived sub-mesoscale eddies, and with a shorter averaging period these would yield a clear signal. In contrast, in the article *Røed and Fossum (2004)* the authors utilized an averaging period of 30 days for investigating Skagerrak and the North Sea with good results. The waters in Skagerrak and the North Sea display more long lived mesoscale eddies than the ones inside the Oslofjord, which are submesoscale eddies. Hence we ended up with the somewhat shorter averaging period (21 days).

In addition we picked out 4 specific locations (Location 1-4 Fig 5.1). Here we examined the surface values for TKE, MKE and EKE, and plotted these as a series in time.

5.2 Results in terms kinetic energy

The panel in figure 5.2 shows the inherent TKE in both model versions during the full simulation. Looking at the volume plot (b) we see that the 300m version contains roughly 17% more water, somewhat hampering the direct comparison in panel a. We see that the difference in TKE between the versions is small, with a slightly higher amount in the 300m version. However, there are exceptions to this. Looking at the TKE values around day 137 we see that the TKE inherent in the 800m version is notable higher than the one in the 300m version. Looking at Figure 5.3 we should note several things. First, both versions has a higher amount of inherent EKE than MKE. Second, the 300m version seems able to resolve more of the mean currents in the Oslofjord. Looking at day 137 we see that the excess amount of TKE consist mostly of EKE.

*An average over a lunar day (24 hours and 50 minutes) would have been more appropriate, but the temporal sampling rate of the results did not allow for this.

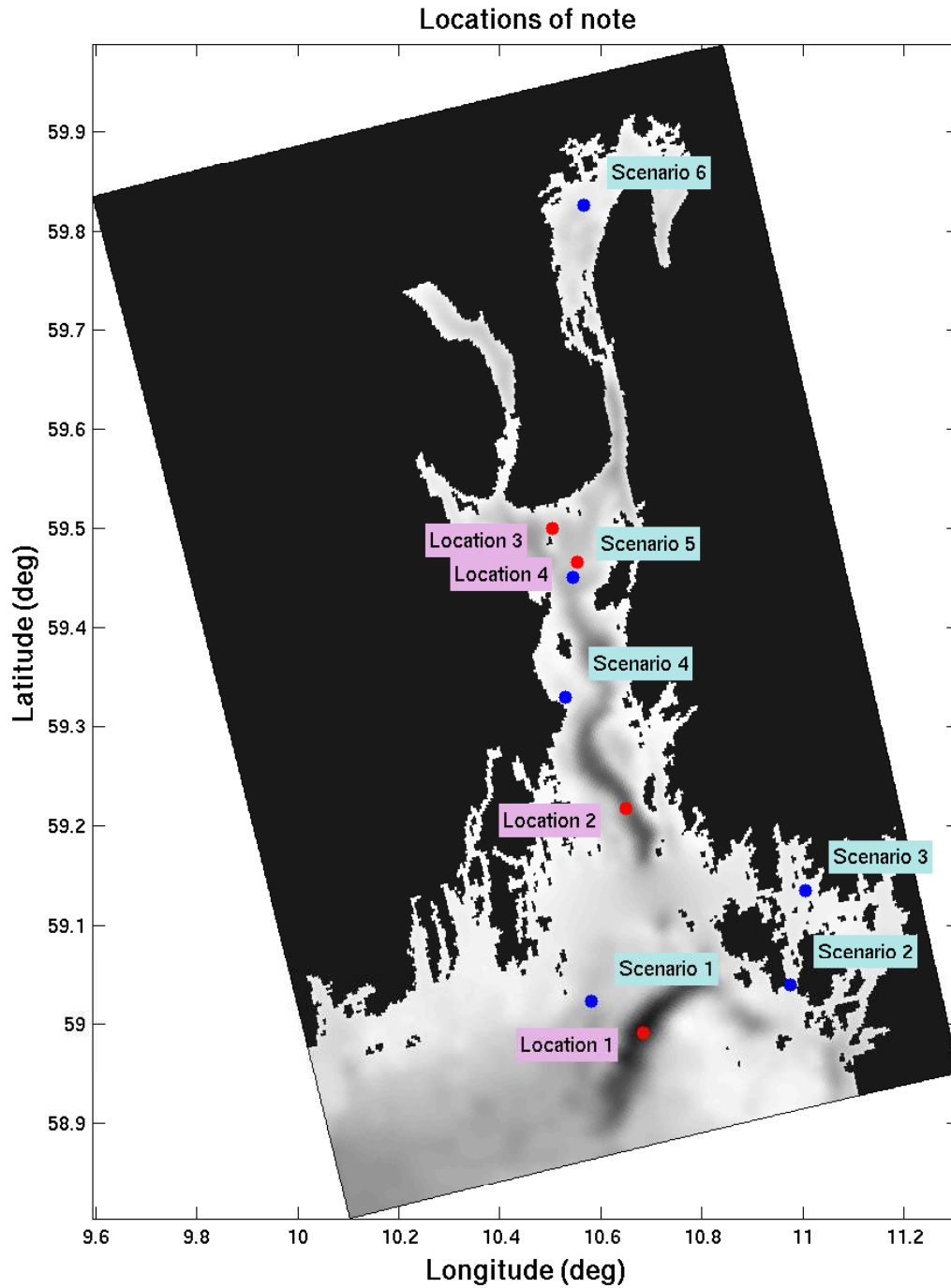


Figure 5.1: The location of the 6 different scenarios in which Lagrangian drifters are released, in addition to the placement of 4 chosen locations where we will take a closer look at the kinetic energy levels later on.

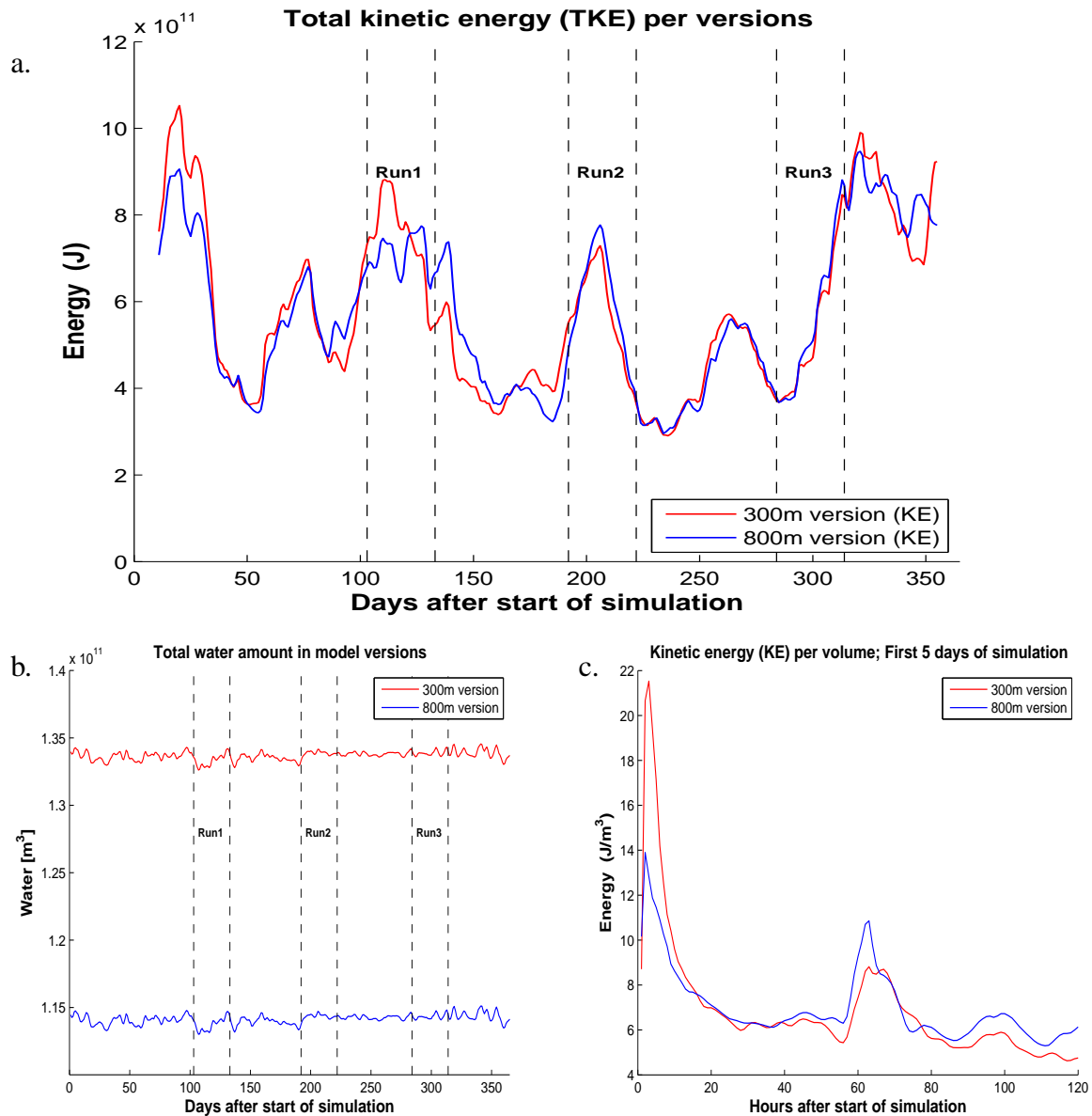


Figure 5.2: Panel a) shows the averaged TKE for both model versions as a function of time. Panel b) shows the amount of water contained in the simulations, helping us interpret the results for the volume averaged kinetic energy. Day 1 corresponds 31.oct.2010. We have used a 21 day average to calculate the values resulting in the missing values for the 10 first and last entries. Panel c) gives a more detailed view on the early development in the KE in the versions, giving insight into the length of the spin-up period. This plot is based on unaveraged model results with a 5 minute spacing, and hence also include tidal effects.

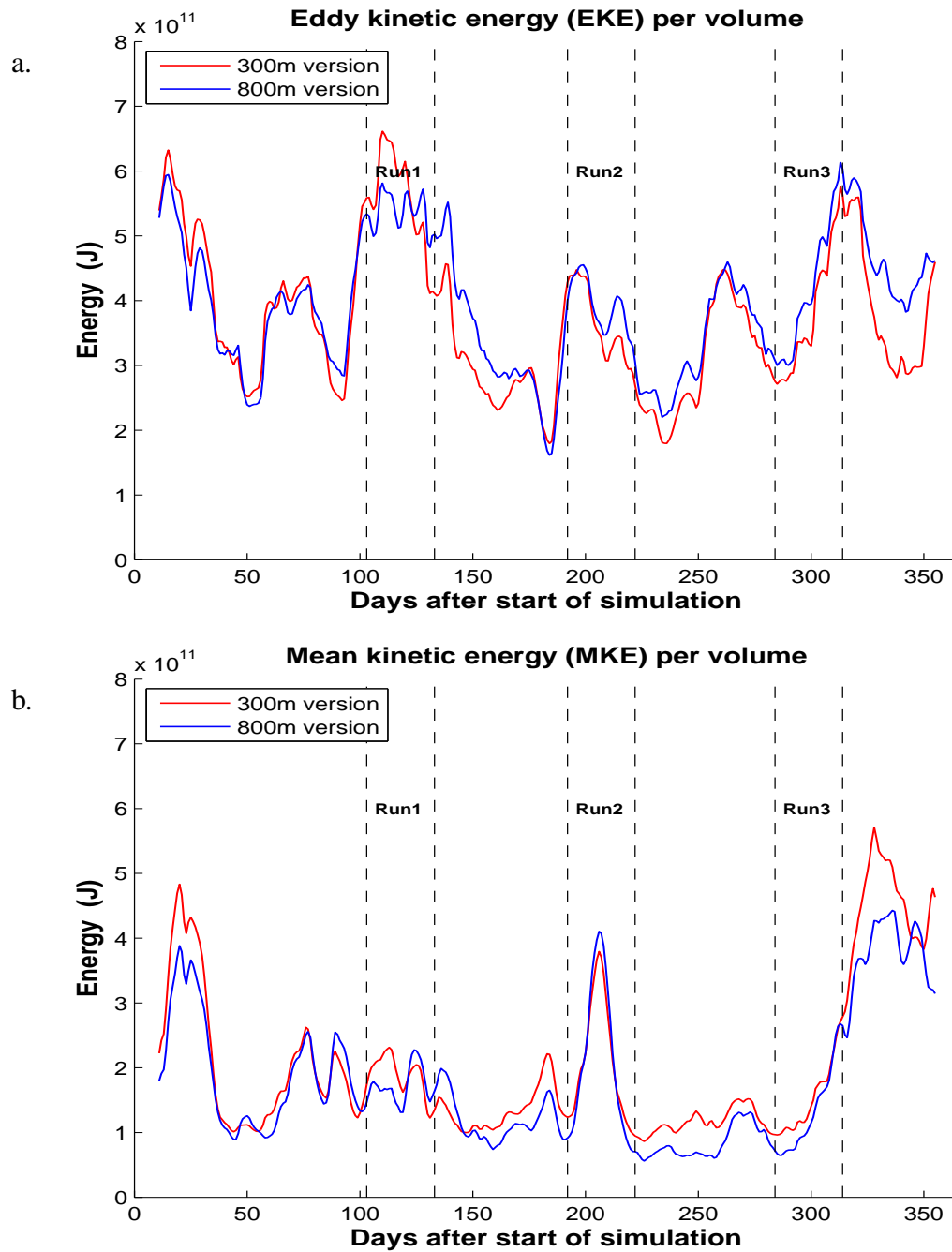


Figure 5.3: As Figure 5.2, but showing the eddy kinetic energy (a) and mean kinetic energy (b)

Figure 5.4 shows the spatial placement of the TKE eddies in both version domains. We see equal patterns between the two versions, but the 300m version has sharper and more confined eddies. The 300m version also has more eddy activity in the middle regions of the fjord, where it displays pockets of high TKE. We also have differences associated with Glomma and the Drøbak strait. Finally, we see that the sill just east of the deep ravine in the southern region of our domain yield large differences. This can be seen as a pocket of low TKE in the 300m version. The sill has been smoothed away from the 800m version (Chap.4.1), hence this version lack this low TKE pocket.

From Chapter 2.3 we know that combining Figures 5.5-5.6 will result in Figure 5.4, which look to be correct. For MKE both versions have the same patterns, but in case of the 300m version they are stronger. The 300m version displays a steady mean current just south of Hvaler and in the Drøbak strait.

The EKE shows many of the same patterns as the TKE, as we see small filaments of EKE spread around the central region of the fjord. We should also note the band of EKE to the north and west of the island Eldøya (Fig.1.2)

Figure 5.7 covers the period around day 137. We see increased eddy activity all over the model domains for both versions, particularly in the southern region. The mentioned sill seems to yield an even larger impact in this period. The 800m version is able to support strong eddies over a larger part of the southern domain, explaining why it is the most energetic for this period in time. In the 300m version we see very sharp and confined eddies, specially for the structures around Eldøya.

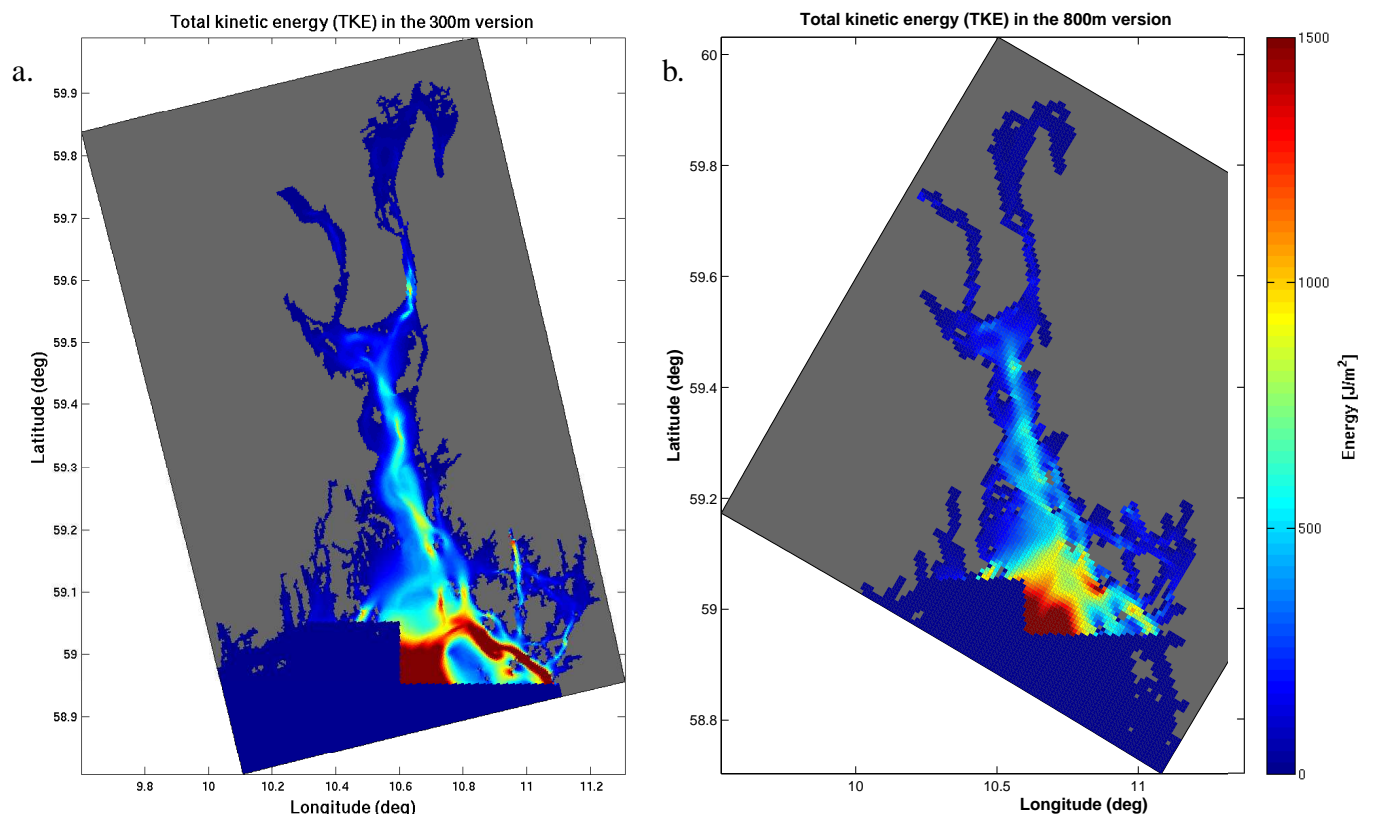


Figure 5.4: Yearly averaged TKE as defined in (2.7) and (2.10) for a) 300m- and b) 800m versions. Areas not common for both grids are removed to ease the comparison.

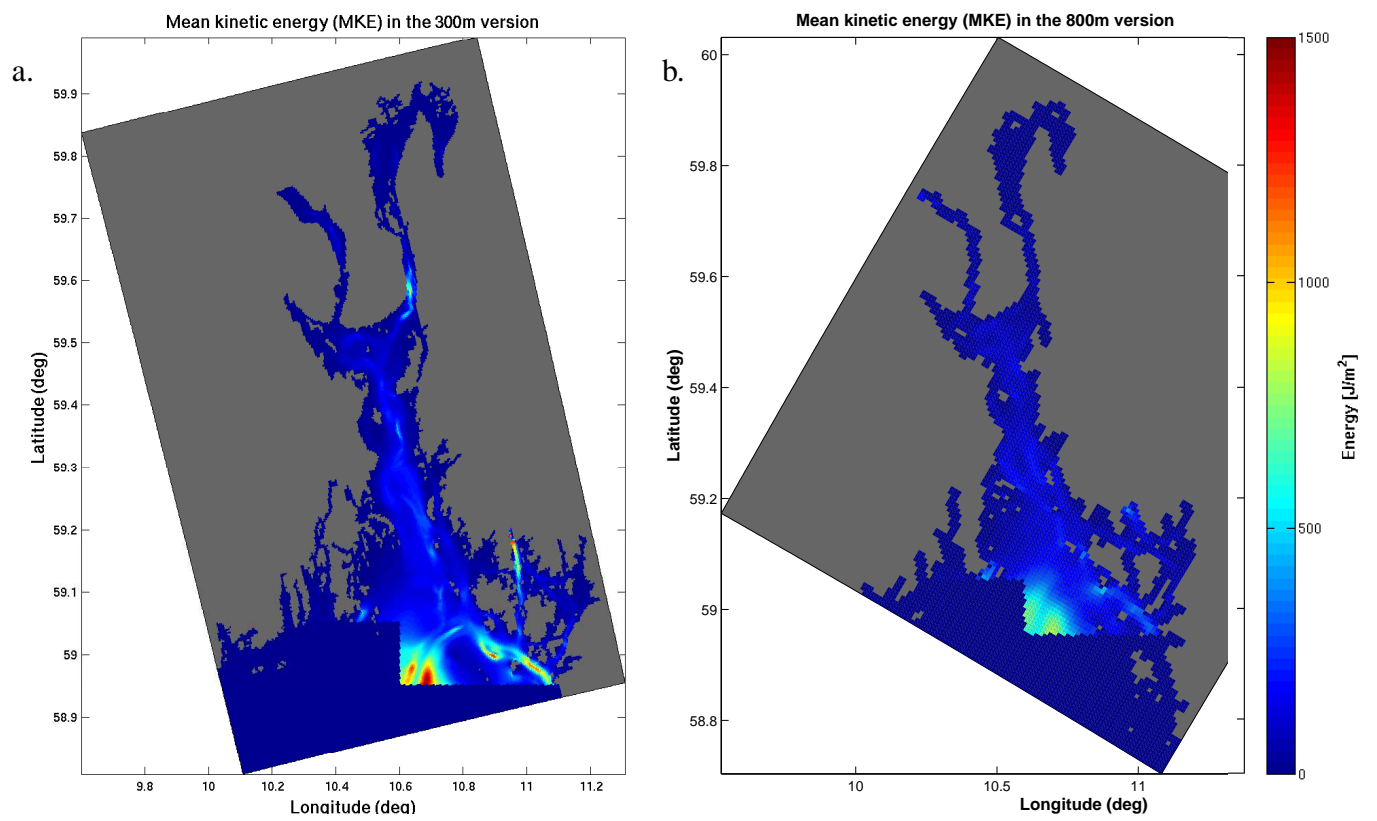


Figure 5.5: As Figure 5.4, but showing the EKE as defined in (2.9).

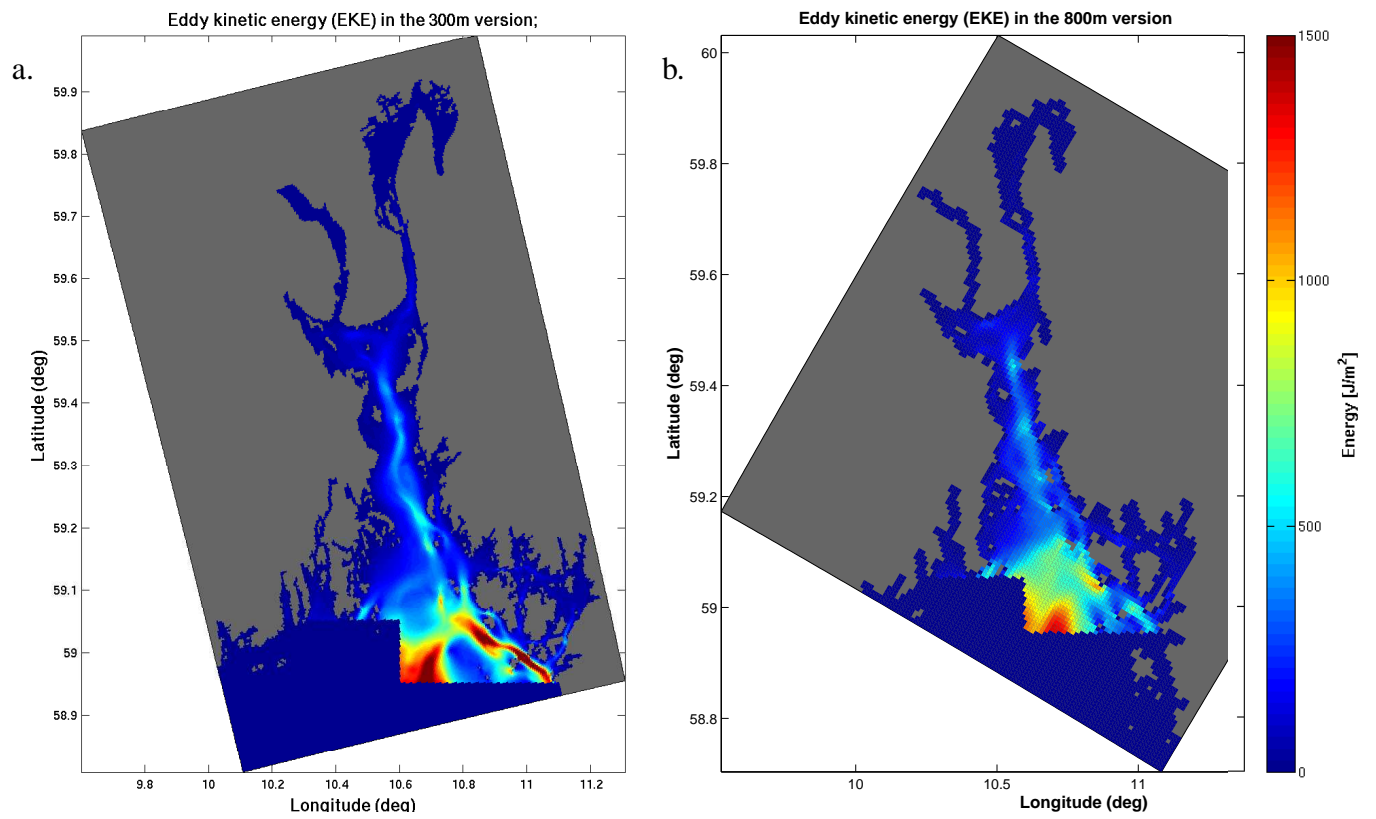


Figure 5.6: As Figure 5.4, but showing the MKE as defined in (2.8).

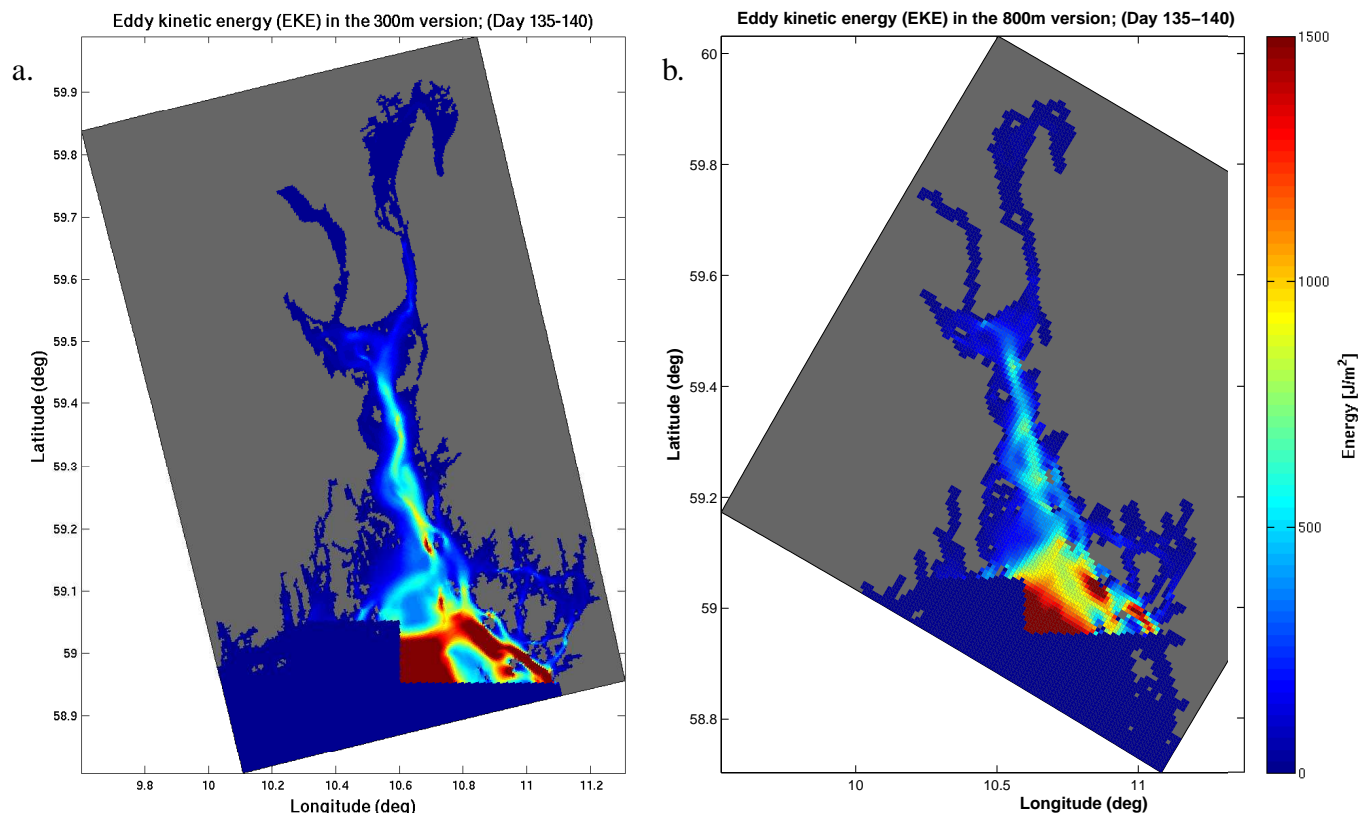


Figure 5.7: 5 day mean (Day 135-140 in simulation) averaged EKE as defined in (2.8) for a) 300m- and b) 800m versions. Areas not common for both grids are removed to ease the comparison.

In Figure 5.8 we see eddy activity in both versions, but the 300m version has the higher values. We also note the spike in EKE happening around run 1, fitting well with observations from Figure 5.7. We see some resemblance between the atmospheric winds and TKE, but not enough to claim a correlation. This especially during run 1. Where we have almost no winds, and high eddy activity in the area.

Figure 5.9 is placed to the north-west of Eldøya. The 800m version has problems resolving any mean currents in the region, while the 300m version is able to this at certain periods of time. Here we might be able to claim a correlation between the winds and TKE, but is still a very weak link. Again we note the period around run 1 where we have high energies and small winds.

Figure 5.10-5.11 should be considered in tandem as they serve a very specific purpose. The island of Mølen (Fig.1.2) is not resolved in the 800m version grid, and by investigating Figure 5.10-5.11 we can quantify the island effect on the local dynamics in the area. Close to the island (Fig.5.10), the 300m version has small values of TKE and no recognizable current patterns. In contrast, the 800m version is able to resolve much of the dynamics, as it displays relatively large values for both MKE and EKE. We also see that the wind is weaker in this region.

In location 4 the 300m version is able to resolve more of the dynamics, and both versions yield similar graphs for the area, with slighter higher values for the 800m version. Implying that in island in the 300m version grid could be obstructive for the generation of larger eddies.

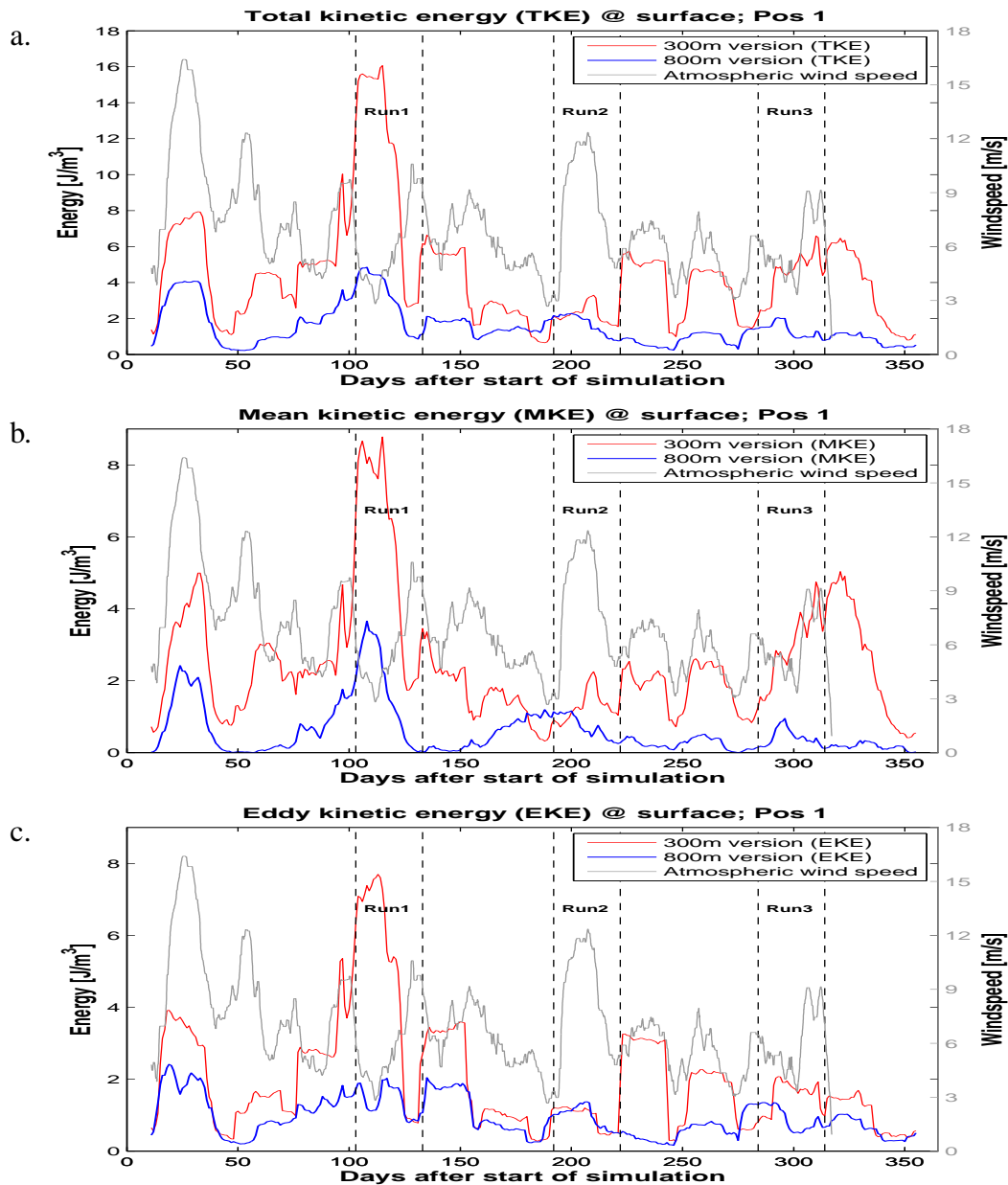


Figure 5.8: Surface kinetic energies for location 1 as a function of time for the whole simulation. Day 1 corresponds to 31.oct.2010. We have used a 21 day average to calculate the values, resulting in the missing values for the 10 first and last entries. The plot also includes the atmospheric wind speeds at the same position to check for possible correlations. The plots is showing the following: a) TKE, b) MKE and c) EKE.

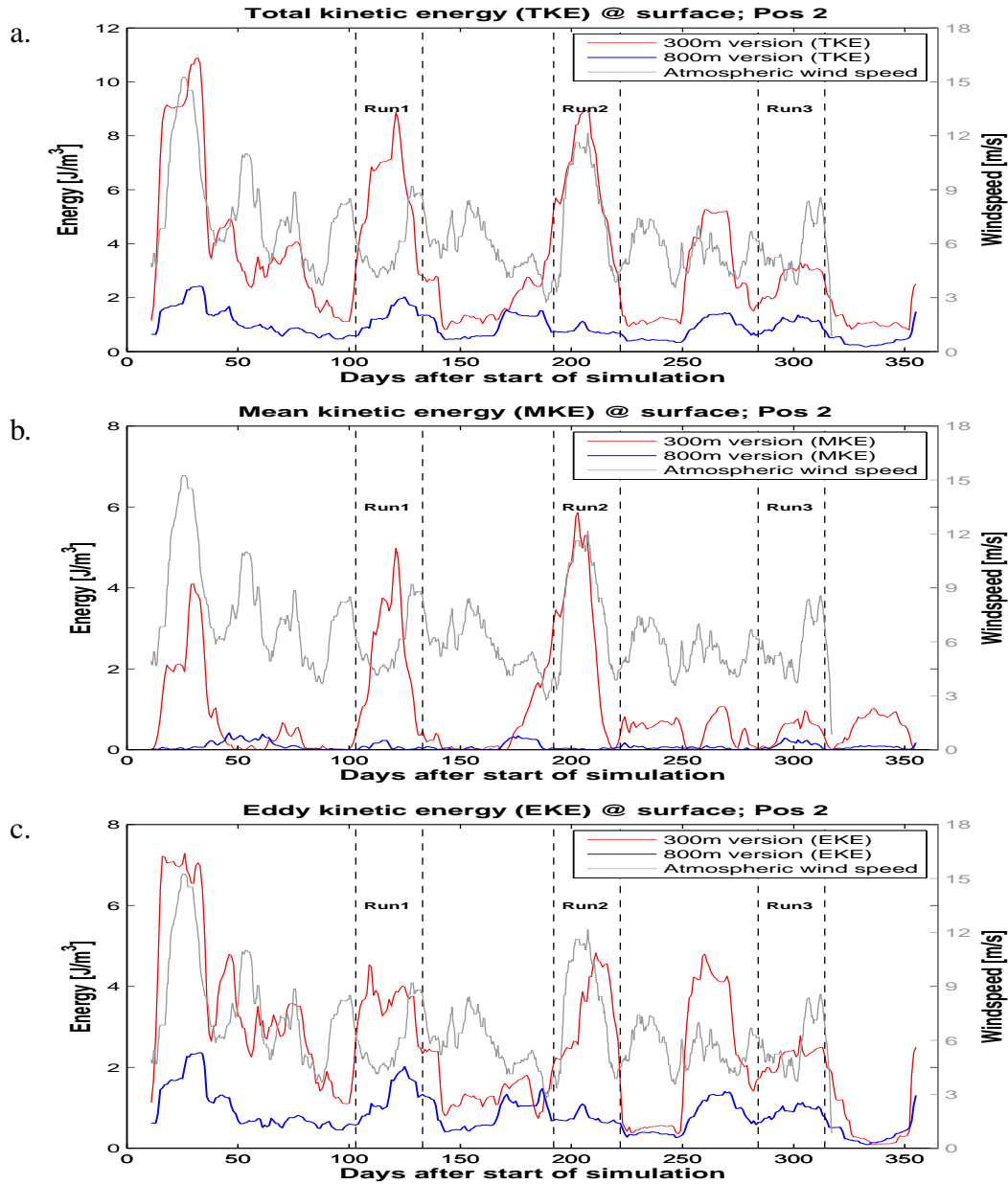


Figure 5.9: Surface kinetic energies for location 2 as a function of time for the whole simulation. Day 1 corresponds to 31.okt.2010. We have used a 21 day average to calculate the values, resulting in the missing values for the 10 first and last entries. The plot also includes the atmospheric wind speeds at the same position to check for possible correlations. The plots is showing the following: a) TKE, b) MKE and c) EKE.

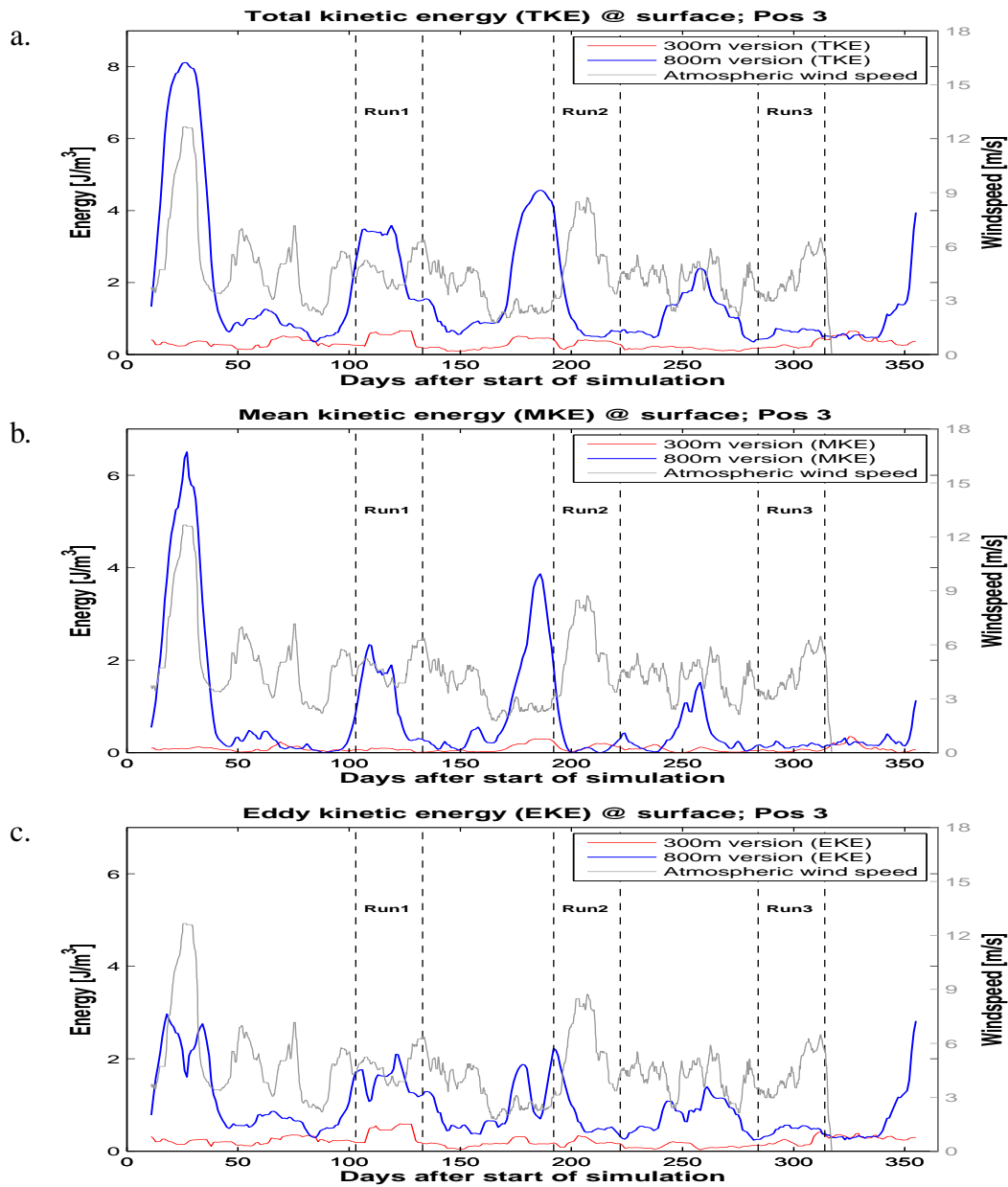


Figure 5.10: Surface kinetic energies for location 3 as a function of time for the whole simulation. Day 1 corresponds to 31.oct.2010. We have used a 21 day average to calculate the values, resulting in the missing values for the 10 first and last entries. The plot also includes the atmospheric wind speeds at the same position to check for possible correlations. The plots is showing the following: a) TKE, b) MKE and c) EKE.

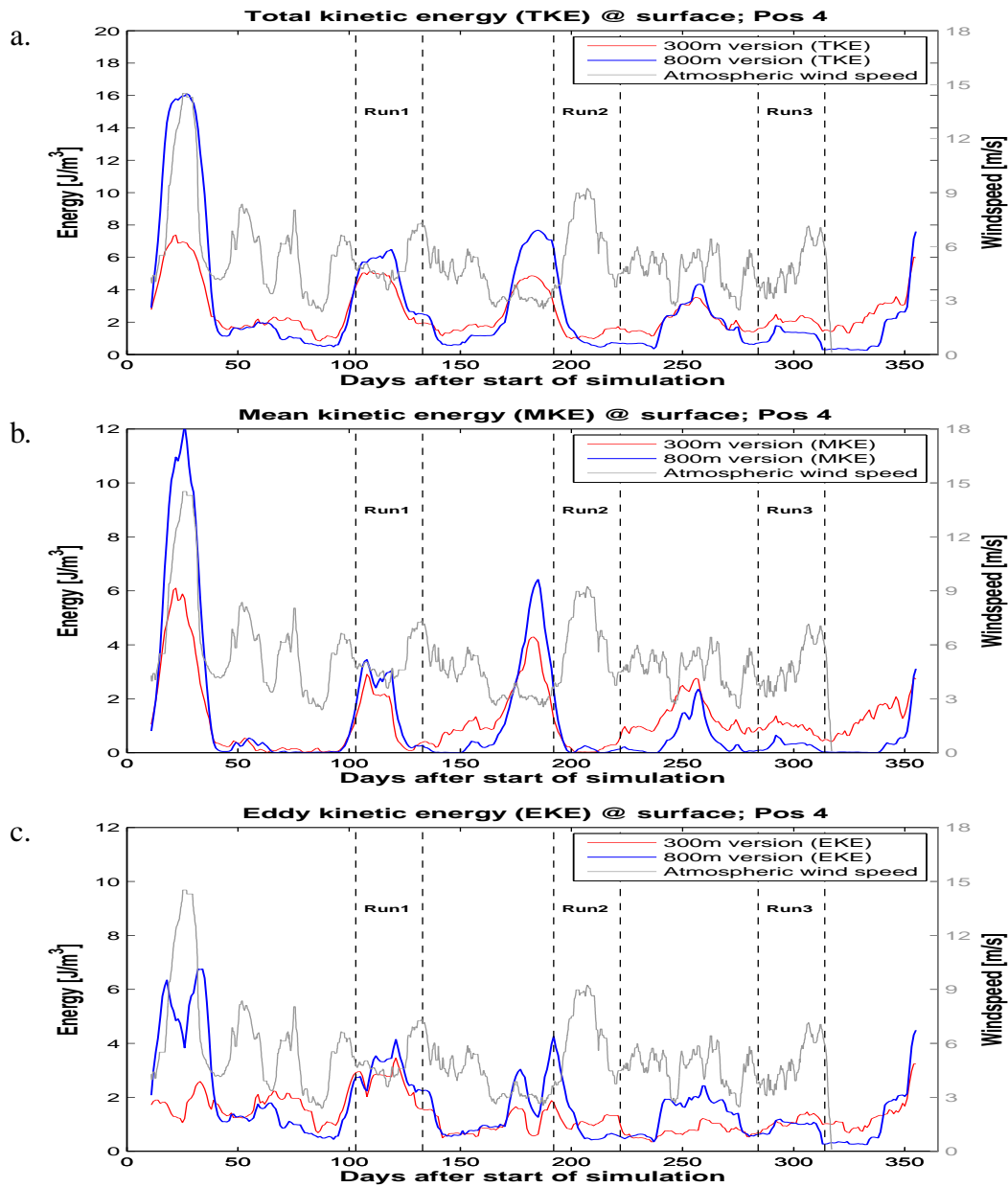


Figure 5.11: Surface kinetic energies for location 4 as a function of time for the whole simulation. Day 1 corresponds to 31.oct.2010. We have used a 21 day average to calculate the values, resulting in the missing values for the 10 first and last entries. The plot also includes the atmospheric wind speeds at the same position to check for possible correlations. The plots is showing the following: a) TKE, b) MKE and c) EKE.

5.3 Particle trajectories

To investigate the behavior of particle trajectories in our two different model versions, a simple experiment making use of Lagrangian drifters/floaters was performed. The drifters were released from stationary points into our two model versions, and their movement was then tracked to look for possible differences.

The experiment was conducted with the aid from a built-in module from the ROMS hierarchy named FLOATS. Here the user specifies where and when he/she want the floats to be released, via a text-file given to ROMS as input prior to the simulation, making it an online configuration. The module also offers several advanced options, as it supports both Lagrangian-, geopotential- ($z = const$) and isobaric ($p = g * (z + \zeta) = const$) drifters. For this experiment we elected to use the Lagrangian floaters. The floats do not interfere with model dynamics (i.e. act like passive tracers), meaning it will be advected only depending on the currents in the grid cell it is currently residing. The release position for the drifters was given as a set of latitude/longitude values, ensuring that the drifters would originate from the exact same location in both model versions. All drifters were released at the ocean surface ($\sigma = 0$ or $z = 0 + \zeta$). We selected 6 separate locations throughout our domain, all associated with a different scenario, which were to be used as points of origin for the drifters. The different scenario locations (numbered from 1-6) is displayed in Figure 5.1.

- Scenario 1** is situated near the Færder lighthouse, and was primarily selected because of its central location in the lower part of our domain. The verification run showed some differences between our model versions in the area, and the current patterns here is generally well known. The region also marks the start of the Norwegian Coastal Current (NCC), a strong and stable current that can be traced along whole the Norwegian coast.
- Scenario 2** is placed between the two islands of Asmaløy and Kirkeøy in the southern part of the Hvaler archipelago. The Icelandic freight ship Godafoss went ashore on a small islet at this location February 2011, causing a major oil spill. The drift pattern of the oil spill created by the incident is generally well known. As a result, the location was chosen out of curiosity, checking if the model versions could recreate a similar pattern.
- Scenario 3** is located well within the Hvaler national park, a region carefully reviewed in the previous chapter. The area showed large differences in both coastal geometry and bathymetry, causing deviating results in the verification run. Thus it is a prime location to illustrate the difference between our two model grids.
- Scenario 4** is located just outside the Esso's refinery at Slagentangen. This is a very busy port, with several ships docking on daily basis. As a result this location have a high potential for accidents, and was thus chosen.
- Scenario 5** is more of a thought experiment. The Bastøy ferry runs between the cities of Moss and Horten, and this scenario is based on the ferry encountering problems (i.e. capsizing,

*c

*This means that the trajectories is calculated at the same time as the other scalar fields.

| Run no. | Start date | End date |
|---------|------------|----------|
| 1 | 11.feb | 11.mar |
| 2 | 11.may | 9.jul |
| 3 | 11.aug | 9.sept |

Table 5.1: Overview of the time span covered by the different runs. All dates are in the year 2011.

engine problems, etc) midway in the crossing. The placement might seem somewhat near scenario 4 and hence redundant, but the location has proven to point out some interesting differences between the two model versions in our upcoming experiments.

Scenario 6 is placed in the inner parts of the Oslofjord, in the near vicinity of Oslo. This is the densest populated part of the fjord, and in addition we do not have any other scenarios nearby.

The floaters were released over the 3 separate periods in time, as we from now on will refer to as runs. An overview of these are presented in Table 5.3. At the start of each run, the model versions were programmed to release 24 drifters in all scenario locations. These were released with a 5 minute spacing, making the total release time 2 hours.

Run 1 was placed in time so it would contain the date for the Godafoss incident, and the other 2 runs were then set to take place 3 and 6 months after this. The exact dates of the latter two are arbitrary, but a big spread between the dates was preferred so the experiments would cover different seasons. The start date for the actual simulations, were in both model versions set to the same date used in the verification, 31.okt 2010. The typical current speeds and the size of our domain, would suggest that a spin-up time of about 3 days would be sufficient, and probably required for the 300m version only. The 800m version shares most of its traits with Nonocur, including the grid resolution, making a spin-up procedure needless here. However, the long period prior to the first floater release can also be argued for via another factor. In Chapter 4.4 we discussed the tides, and we mentioned that the model versions prediction skill with respect to these increased as we moved further out in the simulation. This could point towards using a relative long time period prior to the runs, ensuring the best possible model performance in both model versions during the experiments.

5.4 Results in terms of particle trajectories

We look at scenario 1 during the 2nd (Fig.5.12] and 3rd run (Fig.5.12). The trajectories taken in the 2nd run is almost equal between the versions. The particles stay in relative open waters, traveling southwards approaching Skagerrak, and exit the model domain in a matter of days.

For run 3 the versions yield more diverging results. Here the floats drift westward. When reaching the southern tip of Tjøme the floats in the 300m version are advected towards shore, entering the archipelago. In contrast, the drifters in the 800m version stay collected, exiting the domain after just over one day. An interesting thing to note here is how the trajectories in the 800m

version start to merge just prior to exiting the domain, indicating a dominant mean current in the area (NCC).

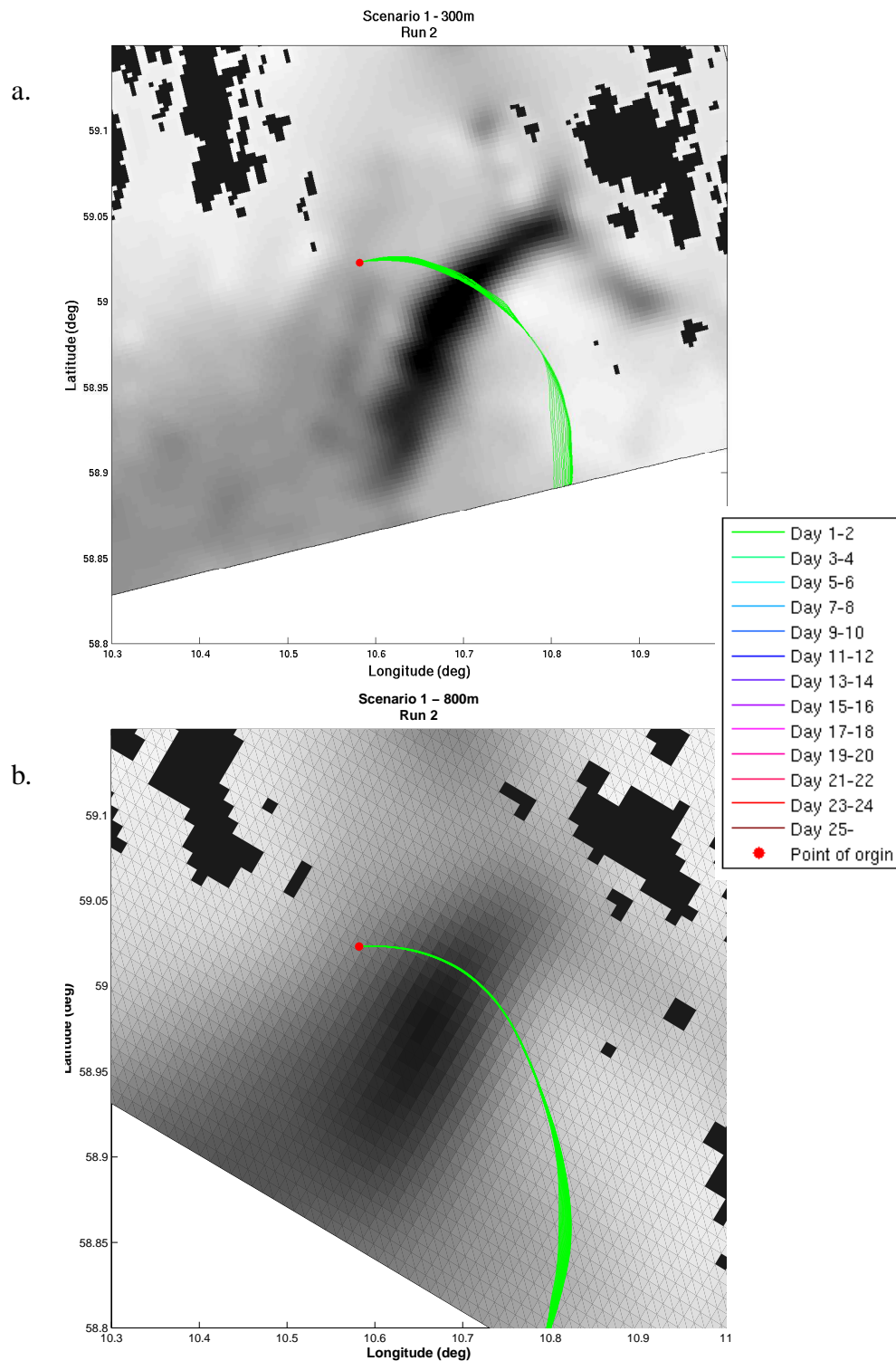


Figure 5.12: Lagrangian drifters trajectories for scenario 1 during the 2nd run for a.) 300m- and b.) 800m version. Each line represent the trajectory of a single Lagrangian drifter, and their color coding changes with respect to the number of days spent by the drifter in the domain relative to the release-time.

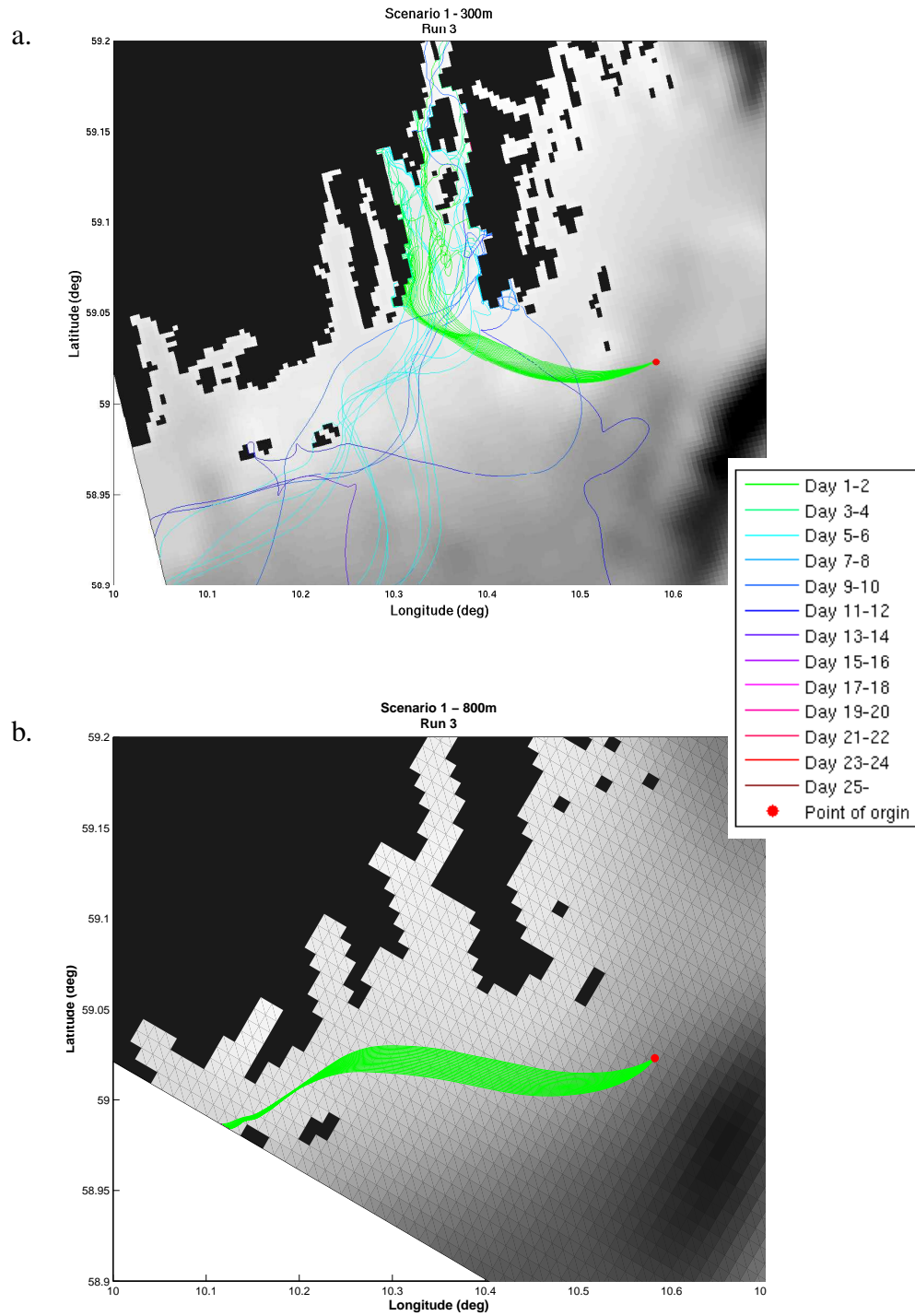


Figure 5.13: Lagrangian drifters trajectories for scenario 1 during the 3rd run for a.) 300m- and b.) 800m version. Each line represent the trajectory of a single Lagrangian drifter, and their color coding changes with respect to the number of days spent by the drifter in the domain relative to the release-time.

Moving on to scenario 2. For the 1st run (Fig.5.14) we again observe diverging trajectories between the model versions. In the 300m version the drifters are advected towards Skagerrak, as soon as they reach more open waters. In contrast, the 800m version displays movement straight over the fjord. Both the time and place for this figure coincides with the date of the Godafoss incident, and the 800m version is actually able to produce similar current patterns to those that was recorded during the accident.

For run 3 (Fig.5.15) we start with similar trajectories. However, when reaching the northwestern tip of Vesterøy the drifters in the 300m version start to spread out considerably. In the 800m version there is hardly no spread, as the vast majority of the drifters ends up going westwards.

Figure 5.16 can be somewhat deceiving as it can look like the all trajectories in the 300m version coincide with each other. This is not the case. The drifters end up going ashore on the eastern side of Vesterøy and the majority stay trapped there throughout the run. For the 800m version we see a more westward tendency. About half of the drifters goes ashore on Vesterøy and the other half exit the archipelago via the western channel.

For the 3rd run (Fig.5.17) the versions yield highly different results. Here the drifters in case of the 800m version, are all able to exit the archipelago via the southern channel. When reaching open ocean we note a large spread, indicating eddies in the area. However, in the 300m version all drifters are advected northwards, stranded east of Fredrikstad.

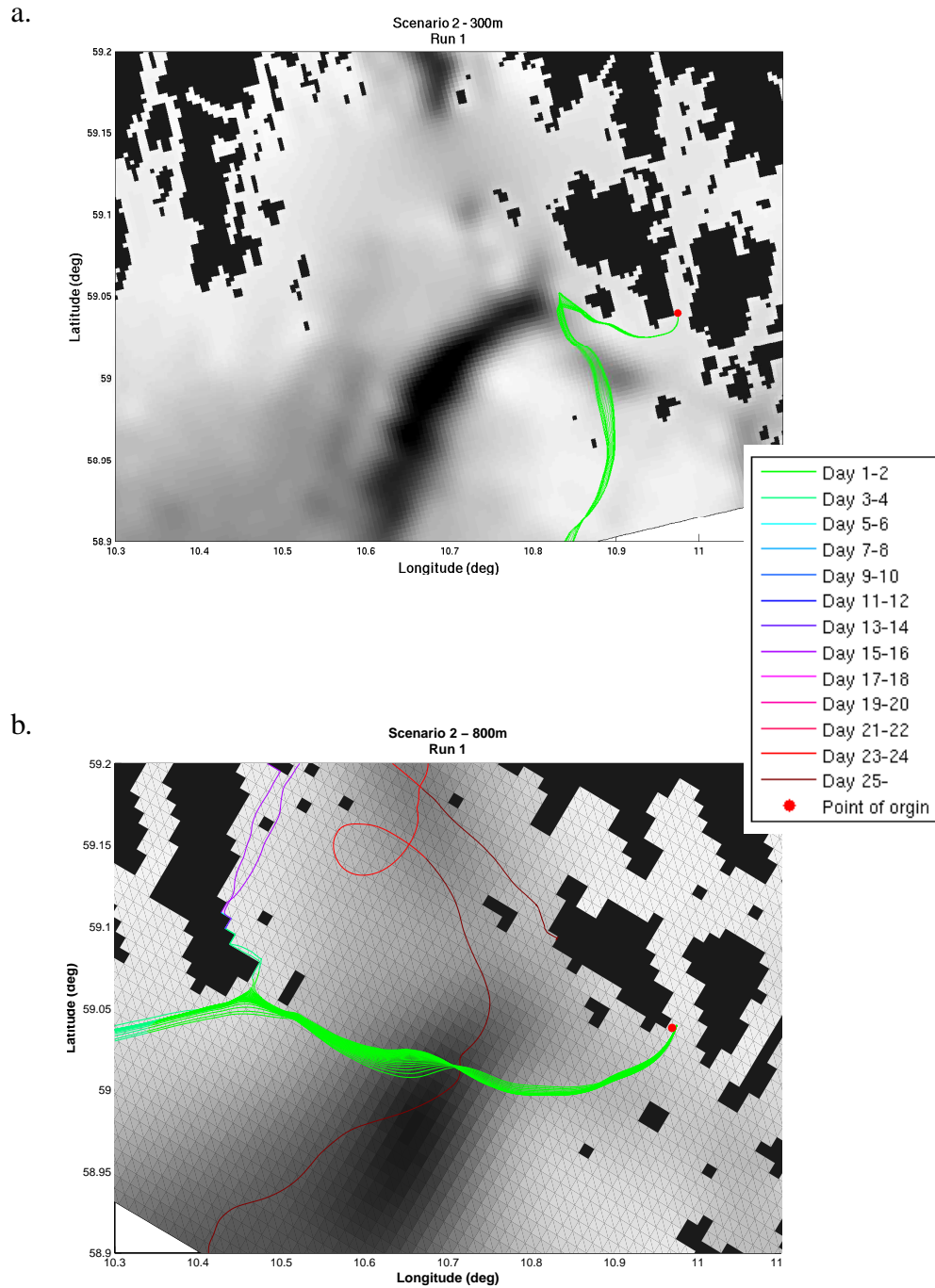


Figure 5.14: Lagrangian drifters trajectories for scenario 2 during the 1st run for a.) 300m- and b.) 800m version. Each line represent the trajectory of a single Lagrangian drifter, and their color coding changes with respect to the number of days spent by the drifter in the domain relative to the release-time.

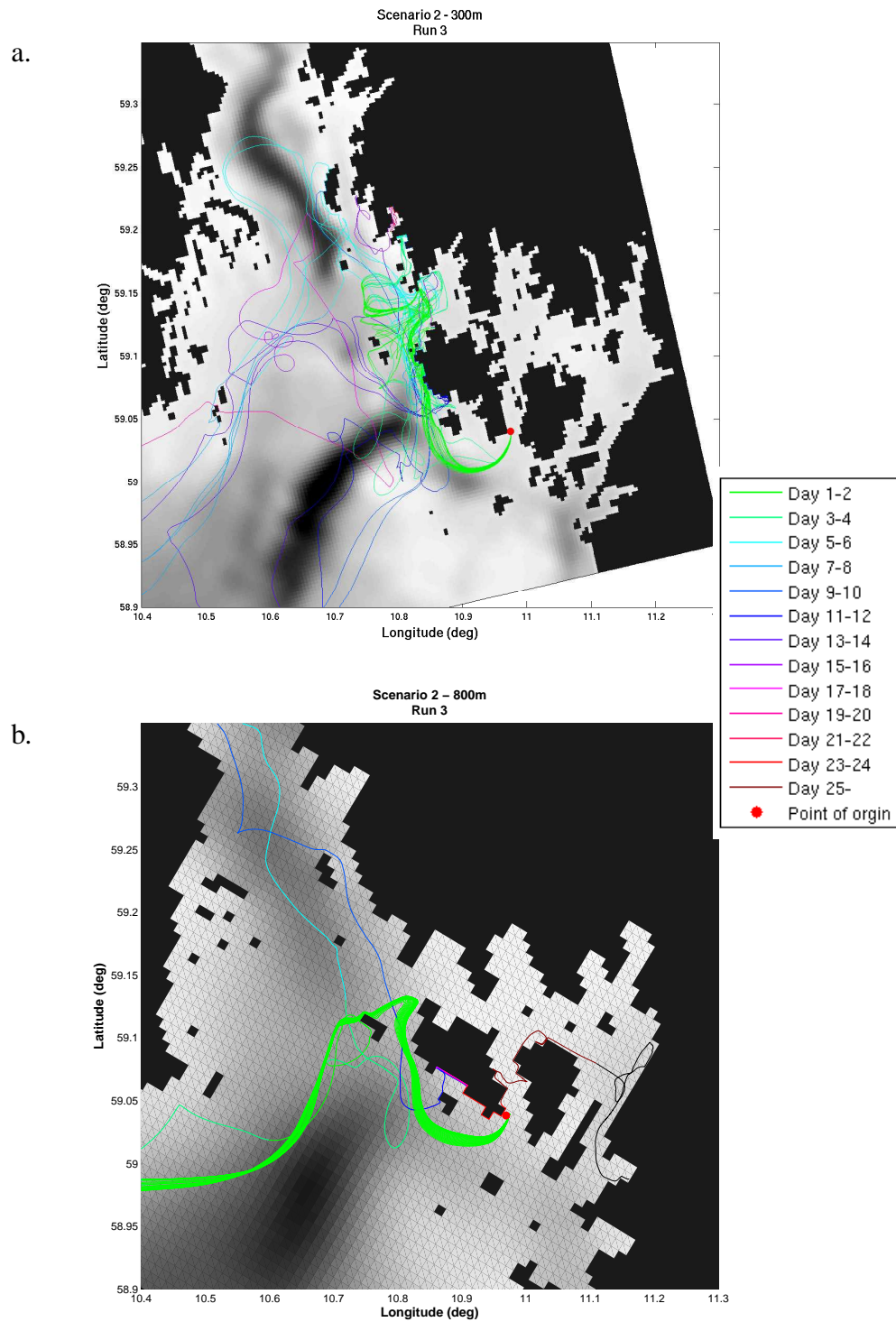


Figure 5.15: Lagrangian drifters trajectories for scenario 2 during the 3rd run for a.) 300m- and b.) 800m version. Each line represent the trajectory of a single Lagrangian drifter, and their color coding changes with respect to the number of days spent by the drifter in the domain relative to the release-time.

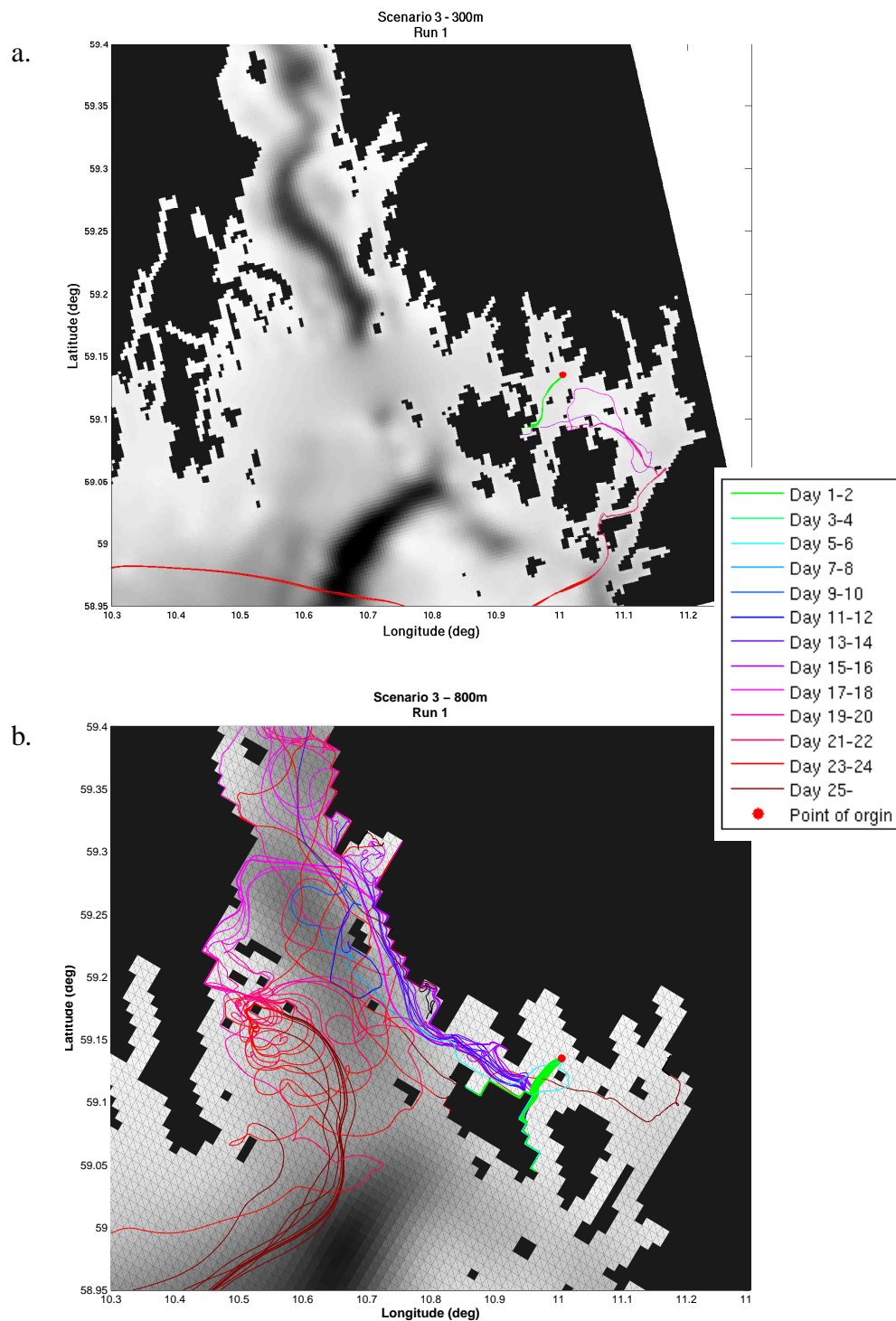


Figure 5.16: Lagrangian drifters trajectories for scenario 3 during the 1st run for a.) 300m- and b.) 800m version. Each line represent the trajectory of a single Lagrangian drifter, and their color coding changes with respect to the number of days spent by the drifter in the domain relative to the release-time.

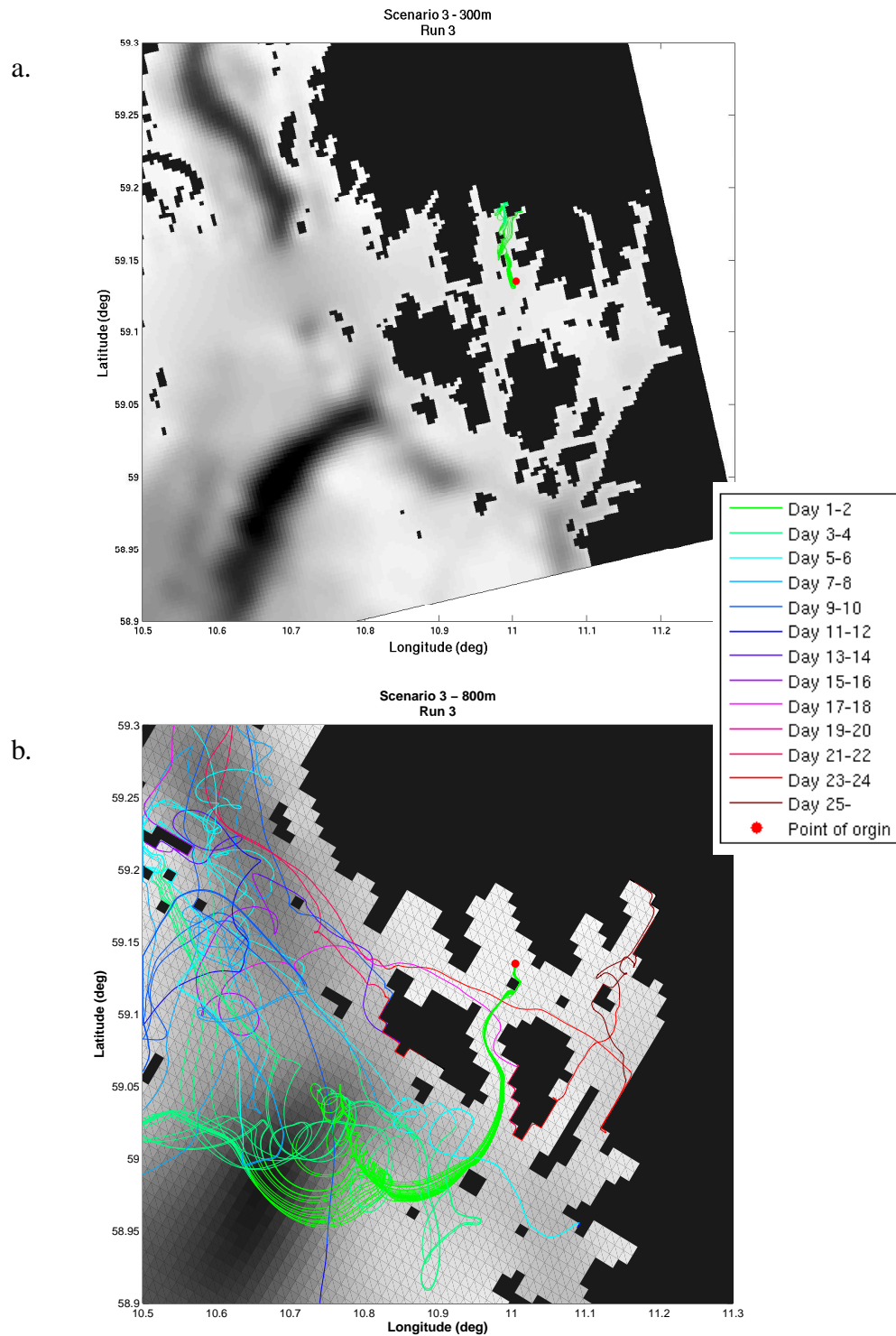


Figure 5.17: Lagrangian drifters trajectories for scenario 3 during the 3rd run for a.) 300m- and b.) 800m version. Each line represent the trajectory of a single Lagrangian drifter, and their color coding changes with respect to the number of days spent by the drifter in the domain relative to the release-time.

Looking at Figure 5.18 we see that the model versions yields trajectories in the opposite direction. In the 300m version the trajectories leads out of the fjord, towards Skagerrak. When reaching the more open ocean they seem to caught up in an eddy, doing a twirl before begin advected out of the domain. On the other hand the 800m version display northward moment, through the Drøbak and into the inner Oslofjord.

For the 1st run at scenario 5 (Fig.5.19) we see similarities in the taken trajectories. In case of the 300m version, the drifters follow the deeper part of the fjord northward towards the estuary of the Drammenfjord. As they approach the estuary they get advected to the south, passing around the western side of Langøya (Fig 1.2). While in the 800m version, the drifters approaches Langøya from the opposite direction. In both cases the drifters end up being advected ashore, and stay trapped there for the duration of the run.

Finally, we arrive at scenario 6. For the 3rd run, we see that both model versions seem to resolve a small eddy just south of the release location. All trajectories display circular motion, but in case of the 800m version we have a slightly larger spread.

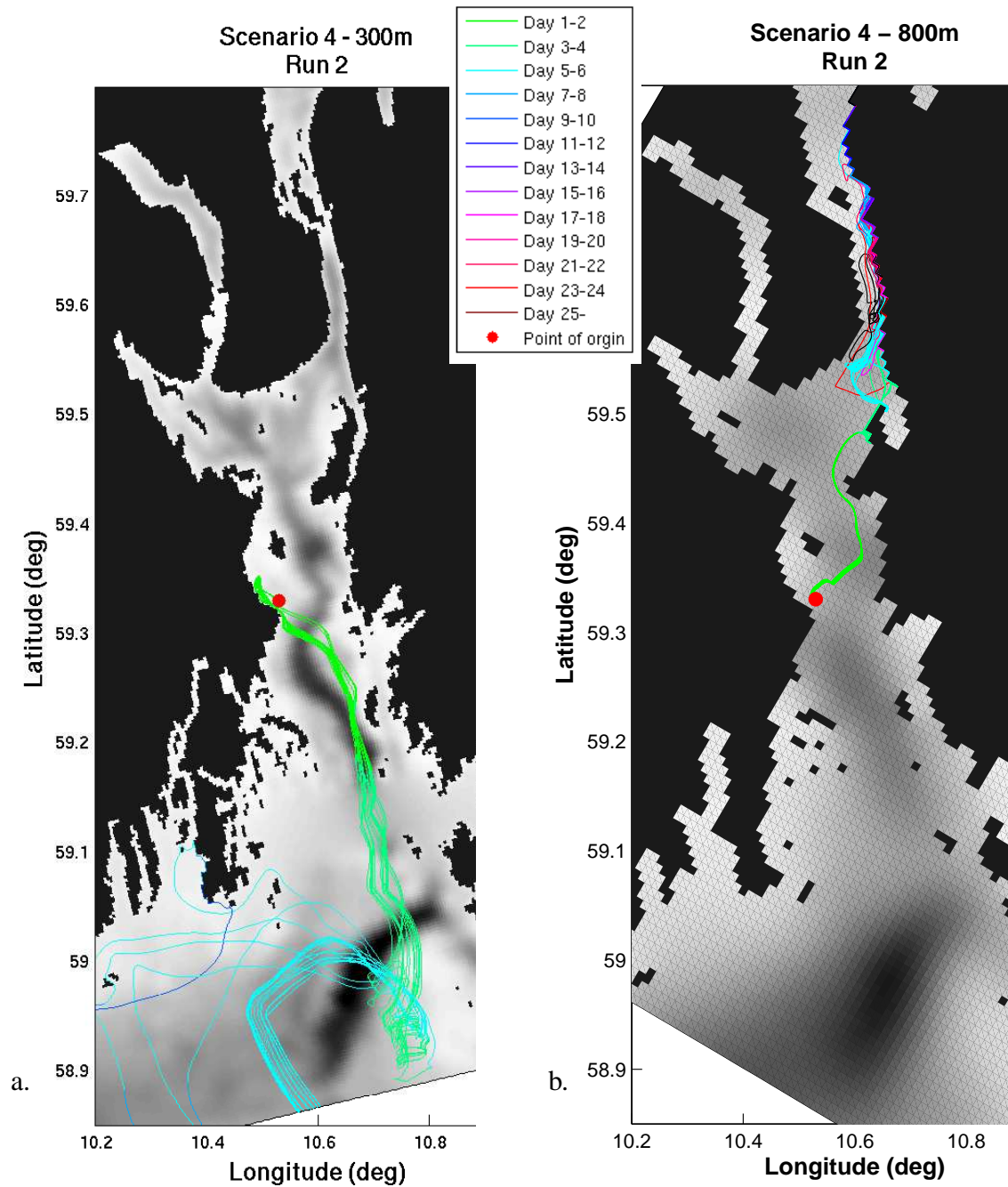


Figure 5.18: Lagrangian drifters trajectories for scenario 4 during the 2nd run for a.) 300m- and b.) 800m version. Each line represent the trajectory of a single Lagrangian drifter, and their color coding changes with respect to the number of days spent by the drifter in the domain relative to the release-time.

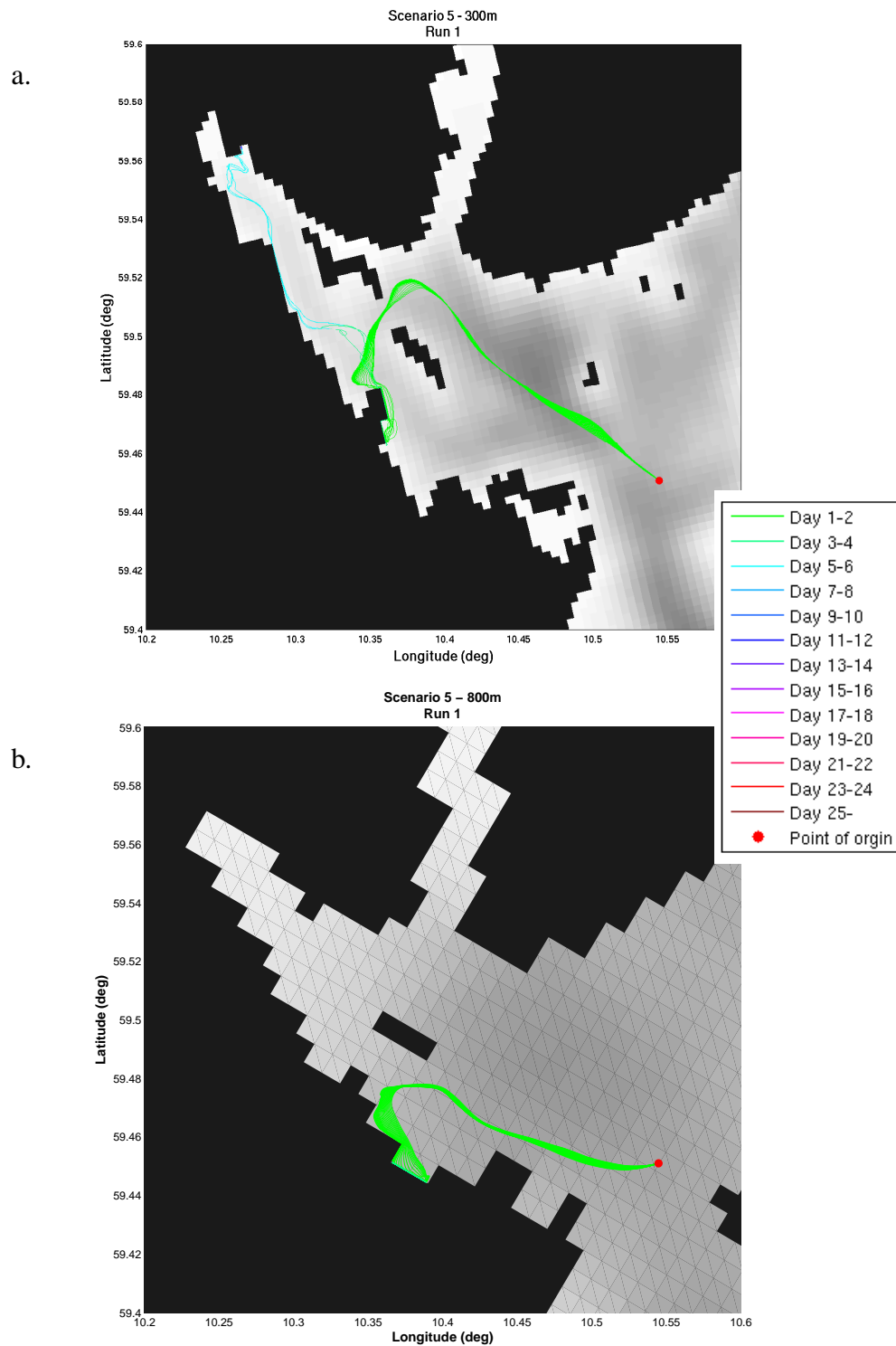


Figure 5.19: Lagrangian drifters trajectories for scenario 5 during the 1st run for a.) 300m- and b.) 800m version. Each line represent the trajectory of a single Lagrangian drifter, and their color coding changes with respect to the number of days spent by the drifter in the domain relative to the release-time.

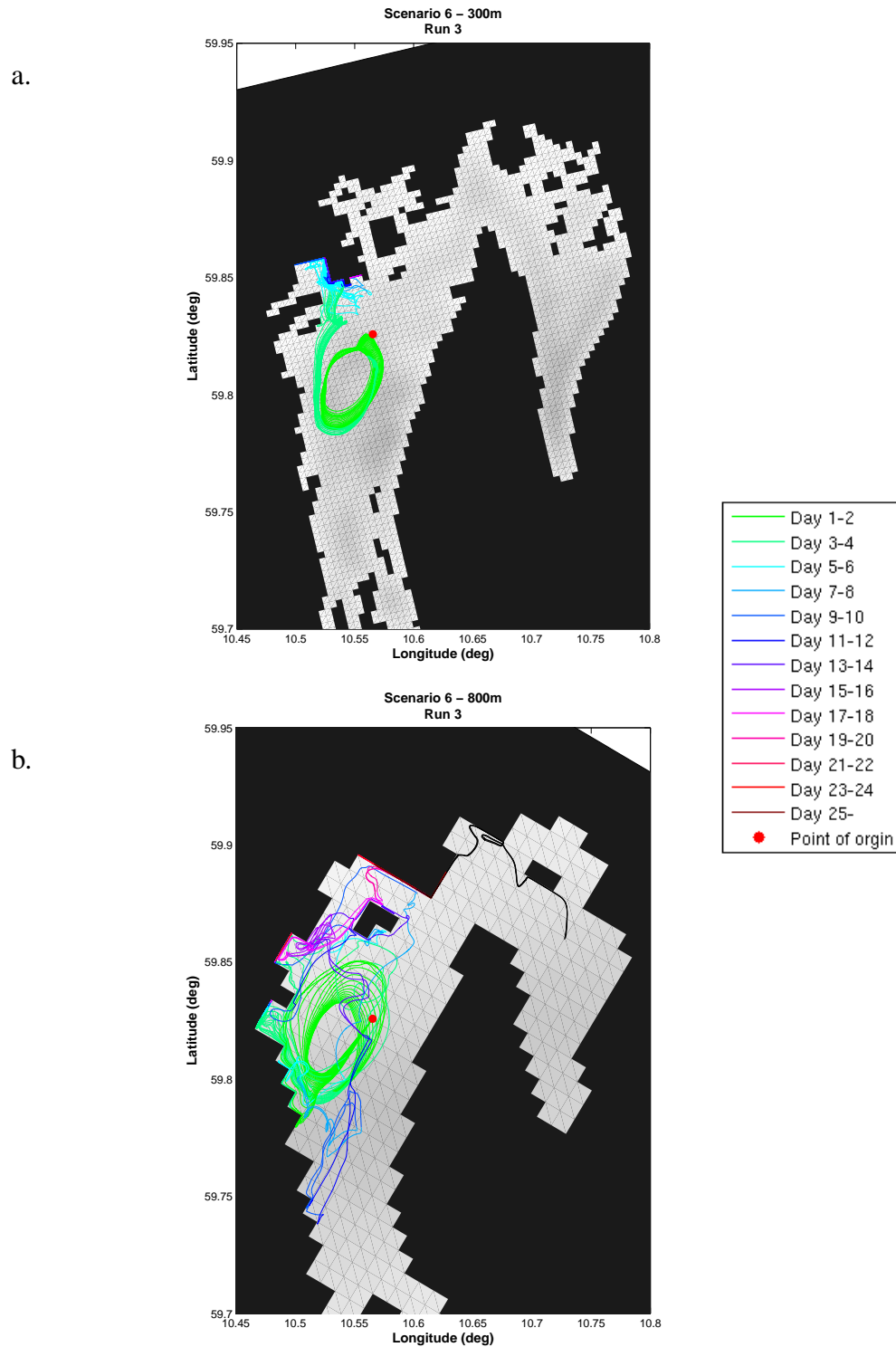


Figure 5.20: Lagrangian drifters trajectories for scenario 6 during the 3rd run for a.) 300m- and b.) 800m version. Each line represent the trajectory of a single Lagrangian drifter, and their color coding changes with respect to the number of days spent by the drifter in the domain relative to the release-time.

Chapter 6

Discussion

Based on the results in Chapter 5 we now ask;

1. How will the differences between the two grids affect the trajectories of particles, and
2. how will the difference in grid resolution be reflected in the energy distribution?

6.1 Preliminary discussion

There are many papers on the subject of grid resolution and its effect on the dynamics in ocean models. *Capet et al.* (2008a,b,c), *Böning and Budich* (1992) and *Røed and Albretsen* (2010) all discuss the topic. The latter is of special interest, since it involves simulations by several models in the oceans just south for our model domain (northern part of the North Sea and Skagerrak). In this paper the authors showed that a version of the ROMS model with 1.5km spatial resolution, was able to capture much of the mesoscale dynamics in the area.

The trend in these papers and similar ones are clear. With the transition from a coarse to a higher resolution model, comes a transfer in the energy distribution from potential- (PE) to kinetic energy (KE). *Gill et al.* (1974) showed that this was associated with an increase in amount of baroclinic instabilities in higher resolution model. The smaller eddies allowed for by higher resolution was found to enhance the energy transfer, by taking available PE from the mean flow and converting it to KE. These eddies tend to evolve in the outskirts of their bigger mesoscale brethren, and are typically smaller in both spatial and temporal scales. However, the conclusions from the above papers are all based on experiments made with coarser ocean models, in combination with a less complex coastal geometry, and hence treats mesoscale eddies rather than submesoscale eddies as studied here.

We know that the vast majority of the KE resides in the bigger scales (mesoscale and upwards). This implies that the increase in KE for two models of different resolution, is expected, but not to be of the dramatic due to the submesoscale nature of the eddies. This is again dependent on the inherent amount of sub- and mesoscale features associated with the model version in question. Our own verification run (Chap.4.4) showed signs of some mesoscale features in the southern

part of the basin, but outside these areas only exhibited a smallish mean current, indicating low KE these areas. This mean that the additional submesoscale eddies inherent in the 300m version contain a relatively larger portion of the KE, yielding this as the most energetic version. There is however an important point that complicates the investigation. The 800m grid is the “victim” of extensive smoothing (Chap.4.1), and that is in addition to its inability to resolve some smaller island in the middle of the fjord. As a result of this the 800m version might be able to yield submesoscale eddies over a larger portion of the fjord, which in some cases could lead to a more energetic 800m version.

The southern area of the basin is the deepest and most open area in our domain. We know from Chapter 2.2 that the Rossby radius of deformation is approximately the same for the entire fjord (5-10km), but restraints placed by topography and bathymetry inhibits the creation of mesoscale eddies inside the fjord. This can be seen clearly in Figures 5.4-5.6, where the regions inside the Oslofjord only display sub-mesoscale features.

Another perspective is the effects of islands in the model domain. *Dong and McWilliams* (2007) concluded that islands could induce so-called island wakes, induced by currents and/or winds. The design of these features would be heavily influenced by the geometry of the particular island in question, and hence the effect changing between domains. They also found wakes when experimenting with “sunken” island. Here the island in the domain was replaced by water, 50m deep. The wakes are associated with an increased vorticity/enstrophy, and hence also the EKE. The 300m version grid is riddled with both large and small islands, and hence has a high potential for islands wakes. The 800m version grid on the other hand is more scarcely populated with respect to islands, making for a notably lower potential. The higher resolution in the 300m version could also be an important factor here, as this will allow for the creation of smaller submesoscale eddies. Note that this effect could also be important around the sill just south-west of Hvaler in the 300m version grid.

6.2 Development in energy

6.2.1 Spin-up

Panel c. of Figure 5.2 shows the KE for the first 120 hours after start of simulation for both model versions. This could be a useful tool with respect to investigating whether a spin up period was required prior to the simulation for the 300m version. In addition to stem from a very similar model (Chap.3.2), the resolution of the 800m version equals that of the initial conditions. This means that it is unlikely that a spin-up period is required for this version. Still it is included in the figure for comparison.

The graph shows that a spin-up time spanning over 1 day is sufficient for both versions (Note that the horizontal axis is in hours), a shorter time-span than the 3 days initially assumed (Chap.5.1). Since the redistribution of momentum is done relative fast, this indicate that the differences in KE between the versions are more locally confined. An assumption that could be verified via the

similarities between the versions in Figures 5.4-5.6.

6.2.2 Discussion

We start by looking at the main KE energy budgets (Fig.5.2-5.3). In Chapter 5.2 we emphasized on the difference in TKE for the time period around day 137. Looking at figure 5.3, we see that the difference in TKE is mainly consisting of EKE. Indicating that a high amount of short lived eddies in the 800m version, is to blame for the differences. Thus, we compare the EKE of the two different versions via Figures 5.6 and 5.7. Figure 5.6 shows the yearly mean EKE, and Figure 5.7 just the period were we had the extraordinary EKE values (days 135-140). During this period, the 800m version shows a large increase in EKE, and the bulk of the increase is situated in the southern region. The smoothing procedure discussed in Chapter 4.1, has left the 800m grid with an almost flat ocean floor in the southern part of the basin. Enabling it to support relative large eddies over the whole southern region. However, this is not the case for the 300m grid, were we find a sill just to the east of the deeper part of the channel (Fig.4.1 and Chap.5.2). Approaching the sill the depth decreases rapidly, going from over 300- to approximately 35 meters over the horizontal span of a few kilometers. The 800m grid cannot support such steep gradient due to the r -value (Chap. 2.1 and 4.1) of the grid getting to large, and hence ends up being 3 times deeper(!) in this region. The final result can be seen as the enclave of low EKE in the southern part of the basin for the 300m version (Fig.5.6). A result going a long way in explaining the relative small differences between the TKE in the two versions, while also highlighting the importance of bathymetry.

But why does this phenomena occur?

Figure 5.8 show the wind speed at Ferder 1.2, and we see that the winds recorded around day 137 are small. However, this is not necessary the case for the winds in the North Sea and Skagerrak. Strong southerlies in the North Sea/Skagerrak region possibly induce boundary currents increasing the current speed around Ferder (Fig.1.2). This could be the cause of the high TKE levels, despite of the low local winds. Another possible explanation could be strong currents originating from the Baltic Sea.

In Figure 5.7 the 300m version shows pockets of confined EKE following the deep channel in the middle of the fjord. These pockets could actually be island wakes, induced by nearby islands or coast formations. The effect is most pronounced in the 300m version, which is natural as this version have the higher resolution and employ the more complex grid. The best example can be seen in Figure 5.7, west of the island Missingen (Fig.1.2). Investigating Figure 5.9 looking at the surface energies at the location just north of Missingen, we see high EKE values at the surface on several occasions. However, we see no sign of a transfer from EKE to MKE associated, with an island wake. Meanwhile, it is possible that the transition occurs further to the south, as the mean currents are stronger there (Fig.5.5). Looking at the currents arriving via the southeastern boundary (Fig.5.5-5.6), in combination with the rugged coastal features around Hvaler. It seems likely that such wakes could be formed. In addition do the region hold several rivers. The fluxes

associated with these could increase the stratification, resulting in more local baroclinic instabilities.

The mentioned concept of “sunken islands” *Dong and McWilliams (2007)*, could also apply to the sill present in the 300m version grid. Looking at EKE in the areas surrounding the sill (Fig.5.6), it seems like nearby eddies are strengthened by the sills presence in the 300m grid. This may be caused by the velocity shear induced by the sills bathymetry. The shear will increase the vorticity in the region, causing a local transition from MKE to EKE. A theory that fits well with observations made in Figure 5.5-5.6.

Our conclusion from this discussion, will be that an increase of the grid resolution is found to have three main effects on the KE in an ocean model.

- Increase in skill in the representation of bathymetry and coastal irregularities. The removal of the sill west of Hvaler from the 800m grid, was found to yield big impacts on the energy budgets. In addition, the more pronounced deep channel running along the middle of the fjord in the 300m grid, was also found to impact the size and location of the eddies. In addition, we found traces of island wakes, especially in the 300m version.
- Increase in the models ability to resolve smaller scale eddies, so called submesoscale eddies. We expected an notable increase in KE associated with the transition between the 800m and 300m model versions. However, the observed increase was small, due the eddies being submesoscale. This effect is still important, but probably more significant when doing simulations in more open ocean areas, where the additional eddies are mesoscale eddies. From *Gill et al. (1974)* we know that such eddies are a very important source of EKE.
- Sharper more confined eddy structures. A natural result of the increased resolution. The enhanced resolution enables sharper representation of different scalar features, as the model now has more spatial grid cells.

6.3 Particle trajectories

From the observation made in 5.4 we split the fjord into two separate regimes;

- Regime 1: Is related to open ocean areas. The predicted trajectories from both model versions showed many similarities in the these regions of the fjord. This was found to be caused by the relative small differences between the model grids regarding bathymetry and coastal geometry associated with these regions. The lack of coastal features, ensured that both models were able to resolve the governing dynamics, leading to trajectories resembling each other.

- Regime 2: Is related to in fjord areas. Here the drifter motion is highly influenced by the irregular coastal geometry. The 300m grid is associated with a high amount of “rugged” coastal features, and it is expected that these will make a substantial impact on the particle trajectories in these areas. The 800m grid is more scarcely populated with these features, and this will cause differences between the two model versions. The 300m version also has a higher potential for development and supporting submesoscale eddies as we approach the more shallow coastal waters.

This distinction can explain much of the particle movement we seen in the trajectory plots (Fig.5.12-5.20).

We start with Figures 5.12-5.13. In 5.12 we are in a regime 1 situation. Here the drifters stay in the deep waters, feeling little effect of the coast. The drifters stay collected in both scenarios, and show similarities in the trajectories taken.

Figure 5.13 is different. The drifters start in regime 1 waters, but as they approach Tjøme (Fig.1.2) the trajectories start diverging. Indicating the importance of the enhanced coastal geometry, with respect to local currents.

Moving to scenario 2 (Fig.5.14). The figure is covering dates just prior to the extraordinary high EKE values. Looking at the taken trajectories we can clearly see traces of the eddy patterns seen in Figure 5.7, as the drifters in case of the 300m version are advected around the sill. The 800m grid contain no such feature, and hence the drifters move right over the fjord. We also note that the trajectories is only showing a small spread, especially when in the more open areas.

Figure 5.15 is showing another interesting property. The trajectories start out equal, but we soon note movement indicating small scales eddies in the 300m version. This could be the product of island wakes produced as the currents are forced between Vesterøy and the small island to the west of Hvaler. We mentioned in the energy discussion (Chap.6.2) how the partial confinement of an ocean current could create a shear, leading to baroclinic instabilities. Leading to an increase in EKE in the expense of MKE.

The Figures regarding scenario 3 both underline the importance of more realistic coastal geometry. For run 1 (Fig.5.16) we see that the assumptions regarding variations in the dynamics of the region is correct (Chap.4.2 and 4.3). In both versions the trajectories go ashore at the island of Asmaløy (Fig.1.2), but after this the versions yields diverging patterns. In the 300m version the floats drift eastward, exiting the archipelago by the southeastern route. In contrast, the drifters in the 800m version exit via the “opened” western channel (Chap.4.2). This shows how a seemingly non-viable trajectory route can get relevant as we reduce the coastal geometry in the model grid.

For run 3 (Fig.5.17) we again notice differences in the trajectories taken by our drifters. The point source of the river flux is a single grid-cell, causing the flux in the 800m version to be wider and weaker than the one in the 300m version. The estuary of the river Glomma (Chap.4.3) is placed just north from the release point. The difference in resolution and facing of the river outflow, is a likely reason for why the drifters is advected away in the 800m version, while being seemingly unaffected in the 300 meter version. In addition, the 300 meter grid has three small

islands between the estuary and the release-point. These islands could act as a natural barrier, preventing the river induced current to reach the drifters, again understating the effect of coastal geometry.

For Figure 5.18 we note that the two versions show complete opposite current patterns. From Figures 5.8-5.11 we see that the Oslofjord is very low in energy at this time. As a result the 800m version is unable to resolve any mean current, possibly explaining the different direction of the trajectories. The relative high EKE and MKE around Moss (Fig.1.2) for the 300m version (Fig.5.9), is also displayed by the drifters. In the form of a slight trajectory spread (EKE) and a mean southward motion (MKE).

For Figure 5.19 the trajectories start out even in both versions, but as the drifters approach the coastal waters they start diverging. In both cases the drifters move west towards Langøya (Fig.1.2). The 300m version yield trajectories to the north and around the island, while the drifters in the 800m version passes to the south. After passing the island the particles drift ashore, but the amount of time spent here is vastly different between the versions. Some of the particles in the 300m version break lose and move north towards Svelvik (Chap.4.2) after a few days, while the drifters in the 800m version is stranded for the full duration of the run. That the drifters diverge in the area around Langøya is interesting. In Chapter 4.2 we examined the area around Svelvik, where we have big differences between the model grids. The the 800m version produced a southern mean surface current the area, and this could result in the floats being advected further south in this version.

For scenario 6 (Fig.5.20), we see resemblance between the trajectories produced by the two versions in the area. Both model versions are able to resolve a small sub-mesoscale eddy near the release point. The higher resolution enables the 300m version to capture more of a mean current in the area. Since models grid is quite similar in this region, the 300m versions has the least spread in the trajectories.

We draw the following conclusion:

- It is not the effect of grid resolution itself that is of most importance for simulations the fjord, but rather the implications it brings in the form of enhanced bathymetry and coastal geometry.
- With increasing complexity of the coastline, follows a larger spread in the particle trajectories. This is of course also dependent on the size of the currents in the region.
- The more defined eddy patters in the 300m version (Fig.5.6) will cause the trajectories to be more sensitive towards perturbations.

Chapter 7

Summary and final remarks

We examine the effect of grid resolution in a fjord, with an emphasis on current patterns, particle trajectories, and developments in kinetic energy (KE).

An increase in grid resolution is found to have two main effects.

- Increased skill in representing bathymetry and coastal geometry including islands
- Increased ability to resolve smaller scale eddies, particular submesoscale eddies resulting in a sharper and more confined representation.

For simulations in coastal regions the first effect is presumed to be largest, an assumption that agrees well with our findings. We found that the bathymetry inherent in the 300m grid, has a somewhat obstructing effect on eddy generation. Thus the net increase in KE associated with the transition to higher resolution version to be small (Fig.5.2). A smoothing procedure performed on the 800m grid prior to the simulation, removed many of the bathymetric features from the model grid. This includes the sill just west of Hvaler, and the deep channel running along the center of the fjord (Fig.4.2-4.1). As a result, the 800m version was able to support substantial eddies over a larger portion of the fjord, explaining the small differences in KE. The inclusion of additional islands in open sea areas was found to be obstructive for mesoscale eddy generation, adding further to the unexpectedly small increase in KE affiliated with the amplified resolution. However, features like island or rugged coastlines were also suspected to cause island wakes. This was seen as an increase in eddy activity in the central areas of the fjord, which took the form as small pockets of high EKE (Fig.5.4-5.6). Particularly the 300m version displayed these features, because of the higher grid resolution and more complex coastal geometry representation.

We find a correlation between the atmospheric winds and the amount of KE in the inner part of the fjord in both versions, agreeing with the consensus (Chap.1) regarding the currents in the Oslofjord.

Our results show a correlation in the behavior of particle trajectories with respect to the location in the model grid, and based on this we defined two separate regimes, for short just called regime 1 and 2.

- Regime 1: Is related to open ocean areas; the predicted trajectories from both model versions showed many similarities in these regions of the fjord. This was found to be caused by the relative small differences between the model grids regarding bathymetry and coastal geometry associated with these regions. The lack of coastal features, ensured that both models were able to resolve the governing dynamics, leading to the resembling trajectories (Fig.5.12).
- Regime 2: Is related to fjord areas. Here we find a large spread of the particle trajectories. Here the difference between the grids regarding bathymetry and coastal geometry, resulted in a more arbitrary trajectory behavior. This, combined with the 300m version's enhanced ability in supporting submesoscale eddies, was found to be the cause of the diverging trajectories (Fig.5.15).

Both the 300m- and the 800m version exhibit the largest deviations in the particle trajectories in the Hvaler region. This was found to be caused by the pronounced local differences in the bathymetry and coastal geometry, combined with the strong outflow from the river Glomma (Fig.5.16-5.17). The “opening” of the western channel in the 800m grid (chap.4.2) is also a key factor in creating the local differences, thus stressing the importance of the coastal geometry. The trajectories in the 300m version were also found to be more susceptible to perturbations. This is a natural result by the latter of the listed effects, as this model version exhibits more confined eddies than the 800m version (Fig.5.4).

So what have we learned? We already knew that performing model simulations in coastal regions places strict requirements on the models. In the introduction (Chap.1) we mentioned the two key factors in (ocean) weather forecasting; the initial conditions, and model skill. We have seen how an increase in the horizontal grid resolution of an ocean model will allow for a more realistic bathymetry and coastal geometry, while also reducing the r -value (chap.2.1)(smoothing factor). All this can be deemed as an increase in the model skill, resulting in a statistically improved forecast.

Note that we have no data enabling us to validate the performance of our two model versions, but based on the theorems of Bjerknes, we assume that the results from the 300m version are closest to the real values.

The implications, though generally well known, from this study are many. A natural continuation of this work should consist of:

- Quantifying the actual increase in forecast skill with respect to grid resolution. For trajectories this could be done via the use of drifting buoys, fitted with a GPS transmitter. The real trajectories received from this could then be used to validate model results for the same time period.

- Examine vorticity/enstrophy for the region. Following in the tracks of *Dong and McWilliams* (2007). This could be used to investigate the effect of island wakes in the fjord.
- Testing for sensitivity with respect to perturbation. This could be done via reproducing this experiment, but use Lagrangian drifters perturbed in space.
- Use of ensemble simulations. These are growing in popularity and are getting more common, especially in weather forecasting. Having an ensemble of coarse models like our 800m version will probably have little value, but experiments with an ensemble of models ranging around our 300m version compared against an even higher resolution model might be interesting.
- A more dynamic model grid. Our 800m version presumably performed satisfactory in the open areas in the fjord, implying that such resolution might be sufficient here. Same skill simulation in complex region like Hvaler, would probably require a resolution in the range of 75 meters. This points toward a more dynamic model grid as an optimal choice for simulations in the Oslofjord. Example of such could be curvilinear- or triangular grids. An interesting prospect would be a regional curvilinear model, with nested smaller local triangular models for complex areas like Hvaler. This would ensure a model with near ideal coastal geometry combined with an efficient use of computer power.

Appendix A

Appendix I

A.1 ROMS parameters

Table A.1 shows ROMS parameters with a short explanation. The two theta terms is used to tweak the vertical distribution of the σ -layers for optimal performance, depending on what phenomena one want to investigate. For further documentation the reader is referred to the ROMS community home page (<http://www.myroms.org>).

| Name | Value | Info |
|-------------|-------|--|
| Vtransform | 2 | Transformation equation used |
| Vstretching | 1 | Stretching function used |
| Nvert | 35 | No. of vertical levels |
| theta_s | 6.0 | S-coordinate surface control parameter ($0 < \text{theta}_s < 20$) |
| theta_b | 0.1 | S-coordinate bottom control parameter ($0 < \text{theta}_b < 1$) |
| Tcline | 30.0 | Width (m) of surface or bottom boundary layer |

Table A.1: ROMS spesific parameters.

A.2 ROMS module list

Following is a list of modules used in both model setups.

| | |
|------------------|--|
| ADD_FSOBC | Adding tidal elevation to processed OBC data |
| ADD_M2OBC | Adding tidal currents to processed OBC data |
| ALBEDO | Shortwave radiation from albedo equation |
| ATM_PRESS | Impose atmospheric pressure onto sea surface |
| ANA_BSFLUX | Analytical kinematic bottom salinity flux |
| ANA_BTFLUX | Analytical kinematic bottom temperature flux |
| ANA_SRFLUX | Analytical kinematic shortwave radiation flux |
| ASSUMED_SHAPE | Using assumed-shape arrays |
| AVERAGES | Writing out time-averaged nonlinear model fields |
| BULK_FLUXES | Surface bulk fluxes parameterization |
| COOL_SKIN | Surface cool skin correction |
| CURVGRID | Orthogonal curvilinear grid |
| DJ_GRADPS | Parabolic Splines density Jacobian (Shchepetkin, 2002) |
| DOUBLE_PRECISION | Double precision arithmetic |
| EAST_FSCHAPMAN | Eastern edge, free-surface, Chapman condition |
| EAST_M2FLATHER | Eastern edge, 2D momentum, Flather condition |
| EAST_M3NUDGING | Eastern edge, 3D momentum, passive/active outflow/inflow |
| EAST_M3RADIATION | Eastern edge, 3D momentum, radiation condition |
| EAST_TNUDGING | Eastern edge, tracers, passive/active outflow/inflow |
| EAST_TRADIATION | Eastern edge, tracers, radiation condition |
| EMINUSP | Compute Salt Flux using E-P |
| FLOATS | Simulated Lagrangian drifters |
| GLS_MIXING | Generic Length-Scale turbulence closure |
| ICE_ADVECT | Advection of ice tracers |
| ICE_BULK_FLUXES | Ice bulk fluxes from the atmosphere |
| ICE_EVP | Elastic-viscous-plastic ice rheology |
| ICE_MK | Mellor-Kantha ice thermodynamics |
| ICE_MODEL | Include sea ice model |
| ICE_MOMENTUM | Compute ice momentum equations |
| ICE_SMOLAR | Advect ice tracers with MPDATA scheme |
| ICE_THERMO | Include ice thermodynamics |
| LONGWAVE | Compute net longwave radiation internally |
| M3CLIMATOLOGY | Processing 3D momentum climatology data |
| MASKING | Land/Sea masking |
| MIX_S_TS | Mixing of tracers along constant S-surfaces |
| MIX_S_UV | Mixing of momentum along constant S-surfaces |
| MPI | MPI distributed-memory configuration |
| NONLINEAR | Nonlinear Model |
| NONLIN_EOS | Nonlinear Equation of State for seawater |
| NORTH_FSCHAPMAN | Northern edge, free-surface, Chapman condition |

| | |
|-------------------|---|
| NORTH_M2FLATHER | Northern edge, 2D momentum, Flather condition |
| NORTH_M3NUDGING | Northern edge, 3D momentum, passive/active outflow/inflow |
| NORTH_M3RADIATION | Northern edge, 3D momentum, radiation condition |
| NORTH_TNUDGING | Northern edge, tracers, passive/active outflow/inflow |
| NORTH_TRADIATION | Northern edge, tracers, radiation condition |
| N2S2_HORAVG | Horizontal smoothing of buoyancy and shear |
| POWER_LAW | Power-law shape time-averaging barotropic filter |
| PROFILE | Time profiling activated |
| K_GSCHEME | Third-order upstream advection of TKE fields |
| RAMP_TIDES | Ramping tidal forcing for one day |
| RST_SINGLE | Single precision fields in restart NetCDF file |
| SALINITY | Using salinity |
| SOLAR_SOURCE | Solar Radiation Source Term |
| SOLVE3D | Solving 3D Primitive Equations |
| SOUTH_FSCHAPMAN | Southern edge, free-surface, Chapman condition |
| SOUTH_M2FLATHER | Southern edge, 2D momentum, Flather condition |
| SOUTH_M3NUDGING | Southern edge, 3D momentum, passive/active outflow/inflow |
| SOUTH_M3RADIATION | Southern edge, 3D momentum, radiation condition |
| SOUTH_TNUDGING | Southern edge, tracers, passive/active outflow/inflow |
| SOUTH_TRADIATION | Southern edge, tracers, radiation condition |
| SSH_TIDES | Add tidal elevation to SSH climatology |
| STATIONS | Writing out station data |
| STATIONS_CGRID | Extracting station data at native C-grid locations |
| TCLIMATOLOGY | Processing tracer climatology data |
| TCLM_NUDGING | Nudging toward tracer climatology |
| TS_U3HADVECTION | Third-order upstream horizontal advection of tracers |
| TS_C4VADVECTION | Fourth-order centered vertical advection of tracers |
| TS_DIF2 | Harmonic mixing of tracers |
| TS_PSOURCE | Tracers point sources and sinks |
| UV_ADV | Advection of momentum |
| UV_COR | Coriolis term |
| UV_U3HADVECTION | Third-order upstream horizontal advection of 3D momentum |
| UV_C4VADVECTION | Fourth-order centered vertical advection of momentum |
| UV_QDRAG | Quadratic bottom stress |
| UV_PSOURCE | Mass point sources and sinks |
| UV_TIDES | Add tidal currents to 2D momentum climatologies |
| UV_VIS2 | Harmonic mixing of momentum |
| VAR_RHO_2D | Variable density barotropic mode |
| WEST_FSCHAPMAN | Western edge, free-surface, Chapman condition |
| WEST_M2FLATHER | Western edge, 2D momentum, Flather condition |
| WEST_M3NUDGING | Western edge, 3D momentum, passive/active outflow/inflow |
| WEST_M3RADIATION | Western edge, 3D momentum, radiation condition |
| WEST_TNUDGING | Western edge, tracers, passive/active outflow/inflow |
| WEST_TRADIATION | Western edge, tracers, radiation condition |

Appendix B

Appendix II

B.1 Harmonic analysis

Here follows the harmonic analysis of the tides for periods covering run 1 and 3 (Tab.5.3). The analysis is done at the location in our grids which coincides with Viker measuring station, placed outside Hvaler. Looking at the plots, the reader should note that in run 1 the tidal constituent M_{sf} is on the same scale as the M_2 component. This factor should be small compared to the bigger contributors in the tidal budget, but this is not the case here. Why?

Let us start with elaborating around the M_{sf} component. The Moon takes 27 days and 7 hours to complete one orbit around the Earth. Since the Earth moves around the Sun, it takes somewhat longer time for the Moon to make one orbit around the Earth relative to the Sun. The time for the Moon to fulfill one such cycle is 29 days and 12 hours, and it is from this feature the M_{sf} component stems.

The key thing to notice here is the period of the M_{sf} component, which is half of the mentioned cycle (14 days and 18 hours). Looking at the plot for ocean height, and then especially for figures (B.1-B.2) where the M_{sf} is largest, we can see variations with a period of around 14 days. This is most probably just the variations in the ocean weather, that just happens to change over the same period as the M_{sf} . The harmonic analysis recognizes the fluctuations as the M_{sf} because of the similarities in the period, and hence we end up with this peculiar result. If we compare figure B.5 to the fluctuations in sea levels during the different runs, we can see clear correlations. If the sea level pressure were to increase as in the beginning of run 1, the ocean naturally responds with a lower sea height and vice versa. Of course this correlation comes as no surprise, but it is always good to see that the model respond in a physical credible way to changes in the forcing. The tidal variations at Viker measuring station should be around 12cm.

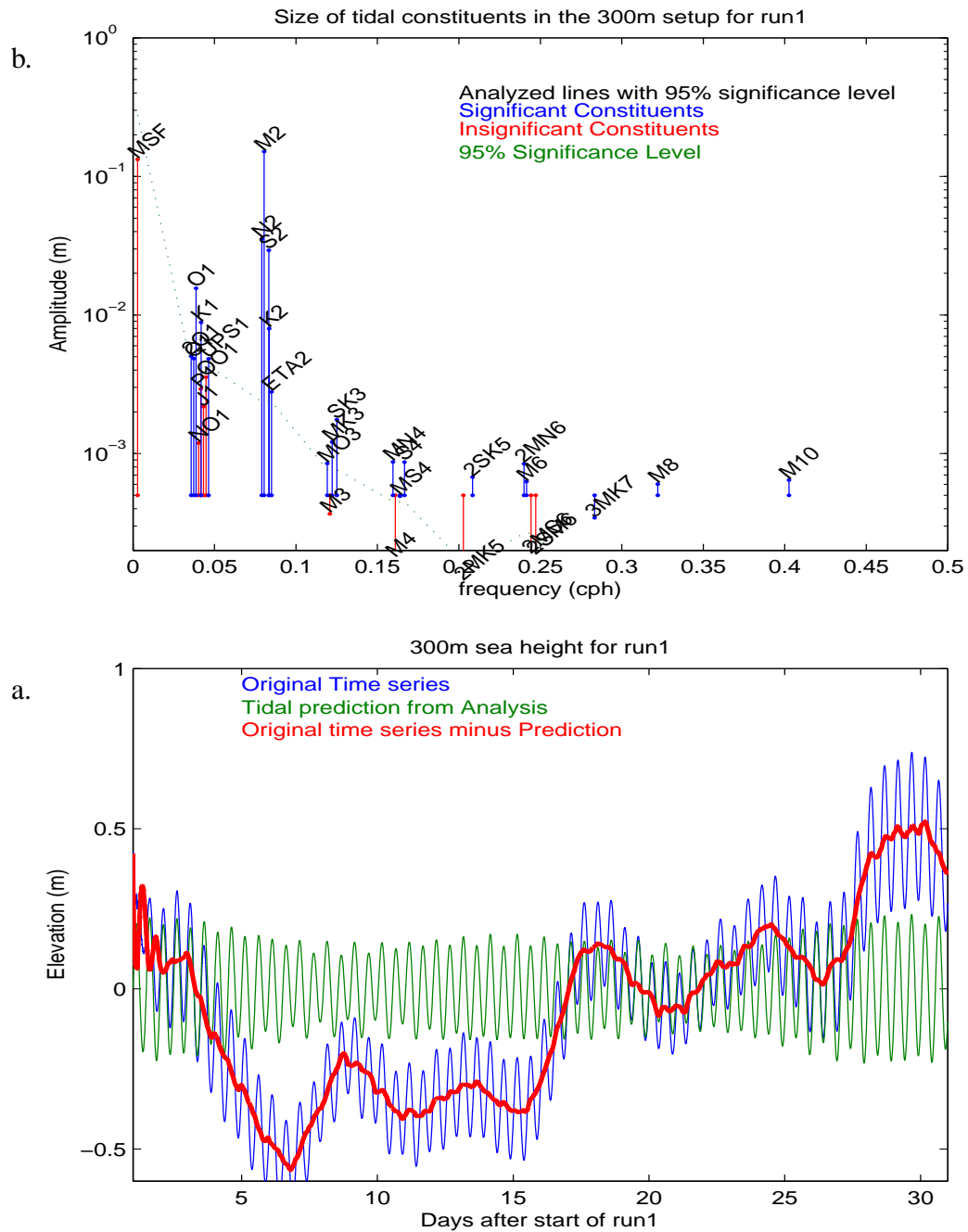


Figure B.1: Harmonic analysis at Viker for the 300 meter setup during the time span covering run 1 (11.Feb - 11.Mar 2011). Plot a) shows the sea elevation, and plot b) shows the size of the different tidal constituents.

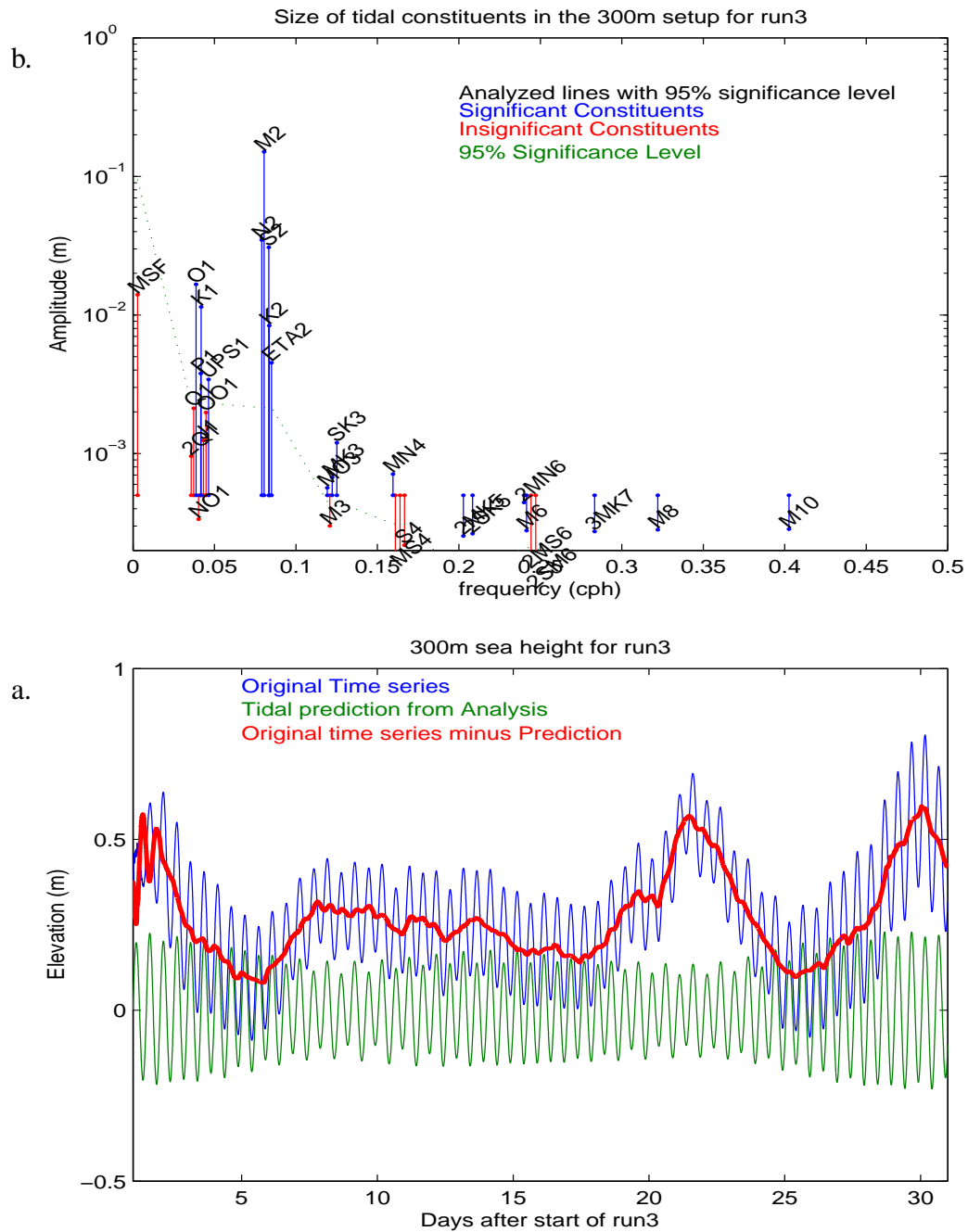


Figure B.3: Harmonic analysis at Viker for the 800 meter setup during the time span covering run 3 (11.Aug - 9.Sept 2011). Plot a) shows the sea elevation, and plot b) shows the size of the different tidal constituents.

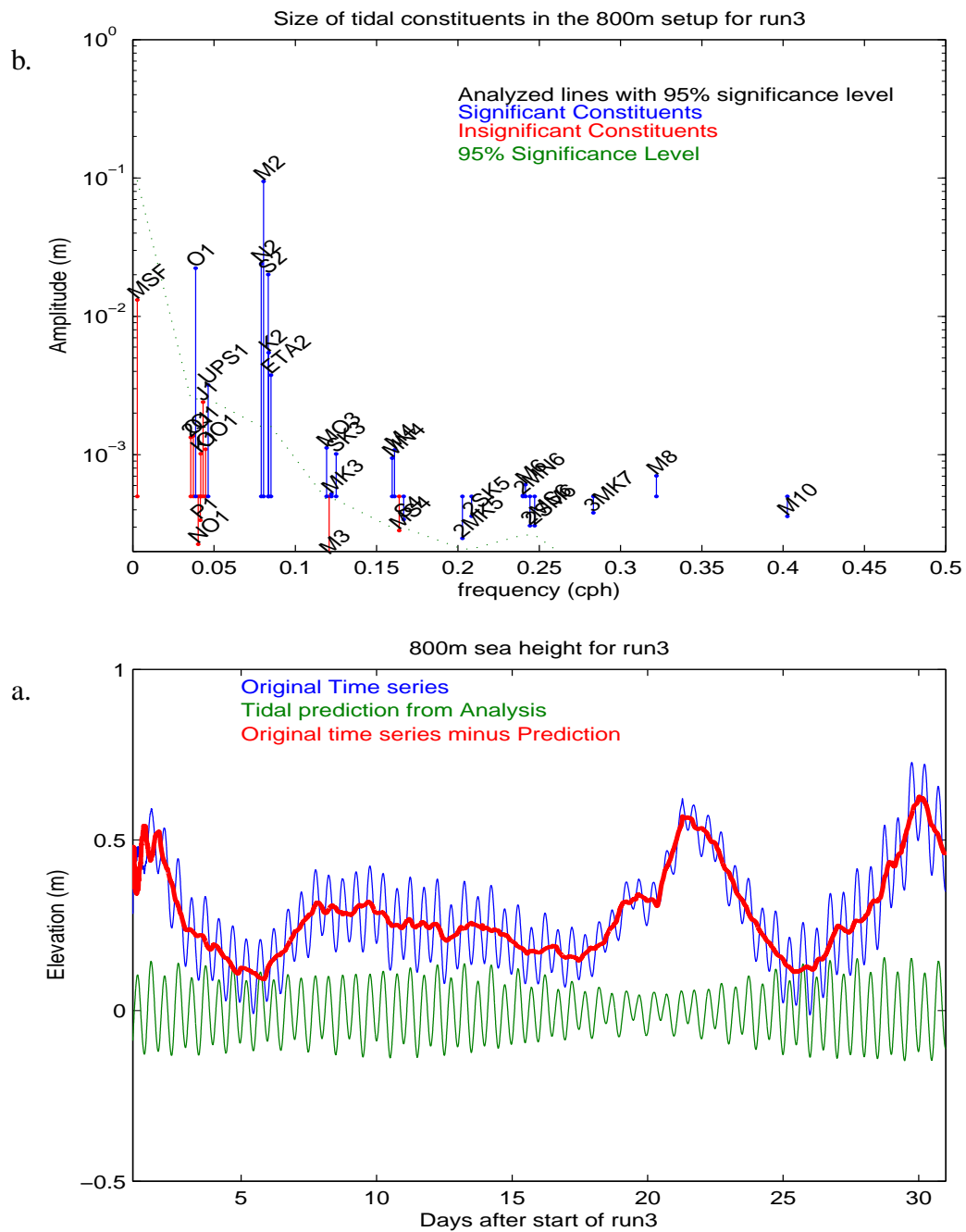


Figure B.4: Harmonic analysis at Viker for the 800 meter setup during the time span covering run 3 (11.Aug - 9.Sept 2011). Plot a) shows the sea elevation, and plot b) shows the size of the different tidal constituents.

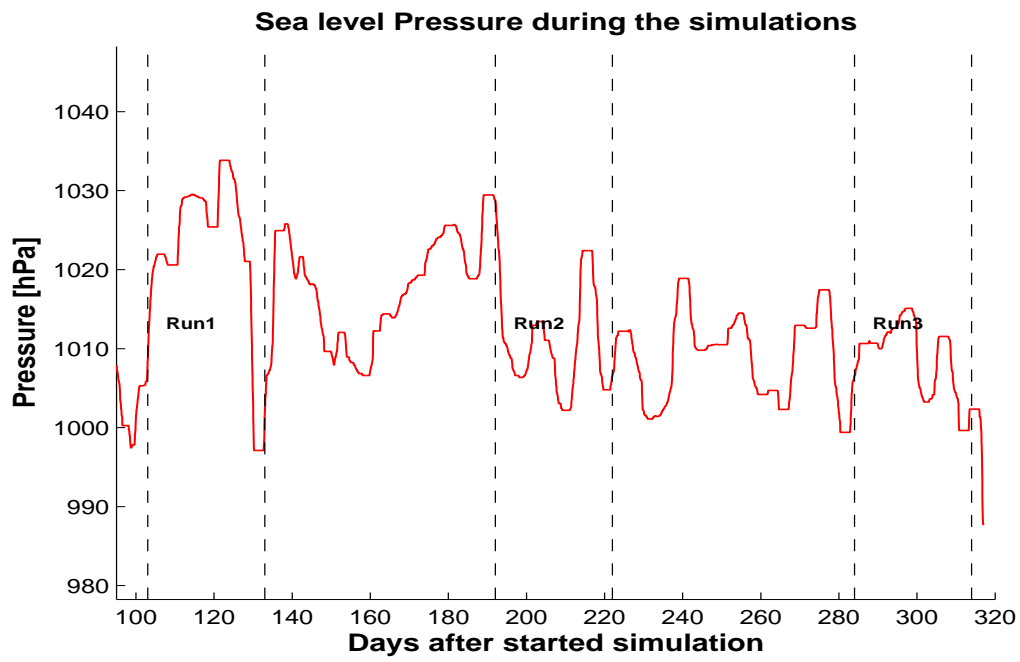


Figure B.5: The sea level pressure at Viker during all 3 runs.

Bibliography

(2014), Roms community webpage, <http://www.myroms.org>.

Albretsen, J., A. K. Sperrevik, A. Staalstrøm, A. D. Sandvik, F. Vikebø, and L. C. Asplin (2011), Norkyst-800 Report No. 1: User manual and technical descriptions, *Tech. Rep. Fisken og Havet 2/2011*, Institute of Marine Research, Pb. 1870 Nordnes, N-5817 Bergen, Norway.

Arakawa, A. (1966), Computational design for long-term numerical integration of the equations of fluid motion: Two-dimensional incompressible flow. part 1, *Journal of computational physics*, 1, 119–143.

Arakawa, A., and V. R. Lamb (1977), Computational design of the basic dynamical process of the ucla general circulation model, *Methods in Computational Physics*, 17, 173–265.

Beckmann, A., and D. B. Haidvogel (1993), Numerical simulation of flow around a tall isolated seamount. part i: Problem formulation and model accuracy, *Journal of Physical Oceanography*, 23, 1736–1753.

Beldring, S., K. Engeland, L. A. Roald, N. R. Sælthun, and A. Voksø(2003), Estimation of parameters in a distributed precipitation-runoff model for norway, *Hydrology and earth System Sciences*, 7, 304–316.

Bjerknes, V. (1904), Das problem der wettervorhersage, betrachtet vom standpunkte der mechanik und der physik, *Meteorologische Zeitschrift*, 21, 1–7.

Böning, C. W., and R. G. Budich (1992), Eddy dynamics in a primitive equation model: Sensitivity to horizontal resolution and friction, *Journal of Physical Oceanography*, 22, 361–381.

Capet, X., J. C. McWilliams, M. J. Molemaker, and A. F. Shchepetkin (2008a), Mesoscale to submesoscale transition in the california current system. part i: Flow structure, eddy flux, and observational tests, *Journal of Physical Oceanography*, 38, 29–43.

Capet, X., J. C. McWilliams, M. J. Molemaker, and A. F. Shchepetkin (2008b), Mesoscale to submesoscale transition in the california current system. part ii: Frontal processes, *Journal of Physical Oceanography*, 38, 44–64.

- Capet, X., J. C. McWilliams, M. J. Molemaker, and A. F. Shchepetkin (2008c), Mesoscale to submesoscale transition in the california current system. part iii: Energy balance and flux, *Journal of Physical Oceanography*, 38, 2256–2269.
- Chelton, D. B., R. A. DeSzoeke, M. G. Schlax, K. Naggar, and N. Siwerts (1997), Geographical variability of the first baroclinic rossby radius of deformation, *Journal of Physical Oceanography*, 8, 433–460.
- Cullen, M. J. P., and T. Davies (1991), A conservative split-explicit integration scheme with fourth-order horizontal advection, *Quarterly Journal of the Royal Meteorological Society*, 117, 993–1002.
- Dong, C., and J. C. McWilliams (2007), A numerical study of island wakes in the southern california bight, *Continental Shelf Research*, 27, 1233–1248.
- Egbert, G. D., and S. Y. Erofeeva (2002), Efficient inverse modeling of barotropic ocean tides, *Journal of Atmospheric and Oceanic technology*, 19, 183–204.
- Egbert, G. D., A. F. Bennet, and M. G. G. Foreman (1994), Topex/poseidon tides estimated using a global inverse model, *Journal of Geophysical Research*, 99, 24,821–24,852.
- Gill, A. E., J. S. A. Green, and A. J. Simmons (1974), Energy partition in the large-scale ocean circulation and the production of mid-ocean eddies, *Deep Sea Research*, 21, 509–528.
- Griffies, S. M. (2004), *Fundamentals of ocean climate models*, Princeton University Press, ISBN 0-691-11892-2.
- Haidvogel, D. B., and A. Beckmann (1999), *Numerical ocean circulation modeling*, vol. 2, 137 pp., Imperial college press, Covent garden, London, ENG.
- Haidvogel, D. B., H. Arango, P. W. Budgell, B. D. Cornuelle, E. Curchitser, E. D. Lorenzo, K. Fennel, W. R. Geyer, A. J. Hermann, L. Lanerolle, J. Levin, J. C. McWilliams, A. J. Miller, A. M. Moore, T. M. Powell, A. F. Shchepetkin, C. R. Sherwood, R. P. Signell, J. C. Warner, and J. Wilkin (2008), Ocean forecasting in terrain-following coordinates: Formulation and skill assessment of the regional ocean modeling system, *J. Comput. Phys.*, 227(7), 3595–3624, doi:<http://dx.doi.org/10.1016/j.jcp.2007.06.016>.
- Orlanski, I. (1976), A simple boundary condition for unbounded hyperbolic flows, *Journal of Computational Physics*, 21, 251–269.
- Pawlowicz, R., B. Beardsley, and S. Lentz (2002), Classical tidal harmonic analysis including error estimates in matlab using t tide, *Computers and Geosciences*, 28, 929–937.
- Phillips, N. A. (1957), A coordinate system having some special advantages for numerical forecasting, *Journal of Meteorology*, 14, 184–185.

- Røed, L. P., and J. Albrechtsen (2010), Decadal long simulations of mesoscale structures in the northern sea/skagerrak using two ocean models, *Ocean Dynamics*, 60, 933–955, dOI: 10.1007/s10236-010-0296-0.
- Røed, L. P., and I. Fossum (2004), Mean and eddy motion in the Skagerrak/northern North Sea: insight from a numerical model, *Ocean Dynamics*, 54, 197–220.
- Røed, L. P., and N. M. Kristensen (2012), Final report: Nonocur. contract no. 4502326827, *Research Report 7/2012*, Norwegian Meteorological Institute, Box 43 Blindern, N-0313 Oslo, Norway.
- Shannon, C. E. (1949), Communication in presence of noise, *Proceedings to the institute of radio engineers*, 37, 10–21.
- Shchepetkin, A. F., and J. C. McWilliams (2005), The regional oceanic modeling system (roms): a split-explicit, free-surface, topography-following-coordinate oceanic model, *Ocean Modelling*, 9, 347–404.
- Warner, J. C., C. R. Sherwood, H. G. Arango, and R. P. Signell (2005), Performance of four turbulence closure models implemented using a generic length scale method, *Ocean Modelling*, 8, 81–113.